CASL-U-2013-0324-000-b

Power uprates
and plant life extension

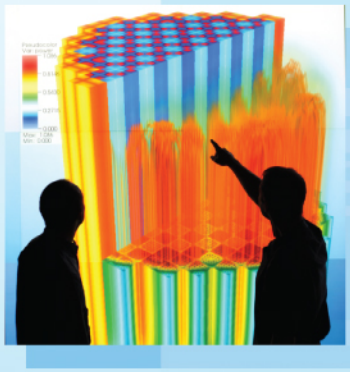

Engineering design
and analysis

Science-enabling
high performance
computing

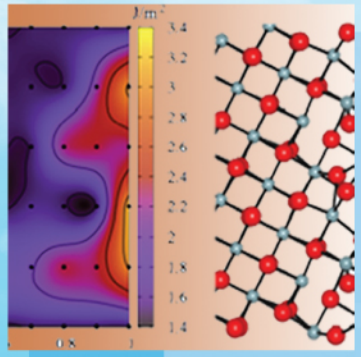

Fundamental science

Plant operational data

Consortium for Advanced Simulation of LWRs

L3:THM.CFD.P6.02

Hydra-TH Verification, Validation and Thermal-Hydraulics Benchmark Problems

Yidong Xia and Hong Luo
North Carolina State University

U.S. DEPARTMENT OF ENERGY | Nuclear Energy

CASL-U-2013-0324-000-b

Hydra-TH
Verification, Validation and Thermal-Hydraulics Benchmark Problems

LA-UR-13-22017

Jozsef Bakosi, Mark A. Christon, and Lori Pritchett-Sheats
Computational Physics and Methods, CCS-2
Los Alamos National Laboratory
Box 1663, MS D413
Los Alamos, NM 87545

Hong Luo, and Tim Xia
Mechanical and Aerospace Engineering Department
North Carolina State University
Raleigh, NC 27695

Robert Nourgaliev
Nuclear Science & Technology
Idaho National Laboratory
P.O. Box 1625
Idaho Falls, ID 83415

March 20, 2013

CASL-U-2013-0324-000-b

Abstract

This document presents a suite of verification, validation and thermal-hydraulics benchmark problems for Hydra-TH. The intent for this suite of problems is to provide baseline comparison data that demonstrates the performance of the Hydra-TH solution methods on problems that vary in complexity from laminar to turbulent flows. Where possible, some form of solution verification has been attempted to identify sensitivities in the solution methods, and suggest best practices when using Hydra-TH.

Contents

1 Introduction **1**

2 Incompressible Navier-Stokes 2D Test Problems **3**

2.1 Poiseuille Flow . . . 3
2.1.1 Problem Description . . . 3
2.1.2 Problem Setup . . . 3
2.1.3 Control File . . . 4
2.1.4 Mesh Files . . . 4
2.2 Lid-Driven Skew Cavities . . . 10
2.2.1 Problem Description . . . 10
2.2.2 Problem Setup . . . 10
2.2.3 Results . . . 11
2.2.4 Control Files . . . 11
2.2.5 Mesh Files . . . 14
2.3 Natural Convection in a Square Cavity . . . 16
2.3.1 Problem Description . . . 16
2.3.2 Problem Setup . . . 16
2.3.3 Results . . . 17
2.3.4 Control Files . . . 19
2.3.5 Mesh Files . . . 19
2.4 Flow Past A Flat Plate . . . 22
2.4.1 Problem Description . . . 22
2.4.2 Problem Setup . . . 22
2.4.3 Computational Results . . . 22
2.4.4 Control File . . . 23
2.4.5 Mesh Files . . . 24
2.5 Turbulent Channel Flow . . . 36
2.5.1 Problem Description . . . 36
2.5.2 Problem Setup . . . 36
2.5.3 Results . . . 37
2.5.4 Control Files . . . 38
2.5.5 Mesh Files . . . 38

3 Incompressible Navier-Stokes 3D Test Problems **45**
3.1 Large-Eddy Simulation of a Lid-Driven Cavity Flow . . . 45
3.1.1 Problem Description . . . 45
3.1.2 Problem Setup . . . 45
3.1.3 Results . . . 45
3.1.4 Control Files . . . 46
3.1.5 Mesh Files . . . 46

4 Thermal-Hydraulic Benchmark Problems **59**
4.1 3×3 Grid-to-Rod Fretting Rod Bundle . . . 59
4.1.1 Problem Description . . . 59
4.1.2 Problem Setup . . . 60
4.1.3 Results . . . 60
4.1.4 Control Files . . . 62
4.1.5 Mesh Files . . . 62
4.2 5×5 Rod Bundle . . . 68
4.2.1 Problem Description . . . 68
4.2.2 Problem Setup . . . 69
4.2.3 Results . . . 69
4.2.4 Control Files . . . 73
4.2.5 Mesh Files . . . 73
References . . . 80

List of Figures

2.1 Control file for laminar flow past a flat plate 5
2.2 Plots of the four successively refined grids for steady Poiseuille flow in a channel: (a) $100 \times 5 \times 1$, (b) $200 \times 10 \times 1$, (c) $400 \times 20 \times 1$ and (d) $800 \times 40 \times 1$ 6
2.3 Plots of x-velocity contours of steady Poiseuille flow in a channel for four successively refined grids: (a) $100 \times 5 \times 1$, (b) $200 \times 10 \times 1$, (c) $400 \times 20 \times 1$ and (d) $800 \times 40 \times 1$ 7
2.4 Plots of pressure contours of steady Poiseuille flow in a channel for four successively refined grids: (a) $100 \times 5 \times 1$, (b) $200 \times 10 \times 1$, (c) $400 \times 20 \times 1$ and (d) $800 \times 40 \times 1$ 8
2.5 Plots of x-velocity profiles at outflow boundary cells of steady Poiseuille flow in a channel for four successively refined grids: (a) $100 \times 5 \times 1$, (b) $200 \times 10 \times 1$, (c) $400 \times 20 \times 1$ and (d) $800 \times 40 \times 1$ 9
2.6 Skewed lid driven cavity geometry (reproduced from Erturk and Dursun[10] without permission). 10
2.7 Kinetic energy vs. time for the 128×128 grids for $\alpha = 15, 30, 45, 60, 90^o$. 11
2.8 15° lid-driven cavity: (a) x-velocity, (b) y-velocity. 12
2.9 30° lid-driven cavity: (a) x-velocity, (b) y-velocity. 12
2.10 45° lid-driven cavity: (a) x-velocity, (b) y-velocity. 13
2.11 60° lid-driven cavity: (a) x-velocity, (b) y-velocity. 13
2.12 90° lid-driven cavity: (a) x-velocity, (b) y-velocity. 14
2.13 A representative control file for the lid-driven cavity problem. 15
2.14 20 x 20 thermal cavity mesh. 16
2.15 Control file for the $Ra = 10^3$ differentially heated cavity. 18
2.16 (a) Nusselt number profile along vertical heated wall, (b) global kinetic energy time history, (c) x velocity along vertical centerline, and (d) z-velocity along the horizontal centerline for $Ra = 10^3, 10^4, 10^5, 10^6$. 20
2.17 Temperature distribution at $t = 2$ time units for (a) $Ra = 10^3$ using mesh B, (b) $Ra = 10^4$ using mesh C, (c) $Ra = 10^5$ using mesh D, and (d) $Ra = 10^6$ using mesh E. 21
2.18 Control file for laminar flow past a flat plate 25
2.19 Plot of the $(25 + 50) \times 30 \times 1$ hexahedral grids for steady flow past a flat plate at $Re = 100,000$: (a) $SR = 1.15$ in y-direction; (b) $SR = 1.20$ in y-direction; (c) $SR = 1.30$ in y-direction 26
2.20 Time history plots for kinetic energy obtained on the $(25 + 50) \times 30 \times 1$ hexahedral grids 27
2.21 Logarithmic plot of the computed skin friction coefficient distribution obtained on the $(25 + 50) \times 30 \times 1$ hexahedral grids compared with the analytical solution along the flat plate $x = [0, 1]$ 27

2.22 Plot of the (a) v_x and (b) v_y profiles obtained on the $(25+50)\times 30\times 1$ hexahedral grids compared with the analytical solutions along the cells cut through by plane of $x = 0.10$ in the boundary layer region . . . 28
2.23 Plot of the (a) v_x and (b) v_y profiles obtained on the $(25+50)\times 30\times 1$ hexahedral grids compared with the analytical solutions along the cells cut through by plane of $x = 0.50$ in the boundary layer region . . . 29
2.24 Plot of the (a) v_x and (b) v_y profiles obtained on the $(25+50)\times 30\times 1$ hexahedral grids compared with the analytical solutions along the cells cut through by plane of $x = 0.99$ in the boundary layer region . . . 30
2.25 Plot of the $(25+50+4)\times 30\times 1$ hexahedral grids for steady flow past a flat plate at $Re = 100,000$: (a) $SR = 1.15$ in y-direction; (b) $SR = 1.20$ in y-direction; (c) $SR = 1.30$ in y-direction . . . 31
2.26 Time history plots for kinetic energy obtained on the $(25+50+4)\times 30\times 1$ hexahedral grids . . . 32
2.27 Logarithmic plot of the computed skin friction coefficient distribution obtained on the $(25+50+4)\times 30\times 1$ hexahedral grids compared with the analytical solution along the flat plate $x = [0, 1.5]$ . . . 32
2.28 Plot of the (a) v_x and (b) v_y profiles obtained on the $(25+50+4)\times 30\times 1$ hexahedral grids compared with the analytical solutions along the cells cut through by plane of $x = 0.10$ in the boundary layer region . . . 33
2.29 Plot of the (a) v_x and (b) v_y profiles obtained on the $(25+50+4)\times 30\times 1$ hexahedral grids compared with the analytical solutions along the cells cut through by plane of $x = 0.50$ in the boundary layer region . . . 34
2.30 Plot of the (a) v_x and (b) v_y profiles obtained on the $(25+50+4)\times 30\times 1$ hexahedral grids compared with the analytical solutions along the cells cut through by plane of $x = 0.99$ in the boundary layer region . . . 35
2.31 The bounded domain for simulation of a turbulent channel flow. . . . 37
2.32 Control file for turbulent channel flow using the Spalart-Allmaras model. . . . 39
2.33 Time history of global kinetic energy for simulation of a turbulent channel flow, $Re_\tau = 590$, Spalart-Allmaras model. . . . 40
2.34 Time history of global kinetic energy for simulation of a turbulent channel flow, $Re_\tau = 590$, RNG k-ε model. . . . 40
2.35 v_x versus normal distance from bottom wall for simulation of a turbulent channel flow, $Re_\tau = 590$, Spalart-Allmaras model. . . . 41
2.36 v_x versus normal distance from bottom wall for simulation of a turbulent channel flow, $Re_\tau = 590$, RNG k-ε model. . . . 41
2.37 v_x^+ versus y^+ from bottom wall for simulation of a turbulent channel flow, $Re_\tau = 590$, Spalart-Allmaras model. . . . 42
2.38 v_x^+ versus y^+ from bottom wall for simulation of a turbulent channel flow, $Re_\tau = 590$, RNG k-ε model. . . . 42
2.39 Turbulent eddy viscosity versus normal distance from bottom wall for simulation of a turbulent channel flow, $Re_\tau = 590$, Spalart-Allmaras model. . . . 43
2.40 Turbulent eddy viscosity versus normal distance from bottom wall for simulation of a turbulent channel flow, $Re_\tau = 590$, RNG k-ε model. . . . 43

2.41 Turbulent kinetic energy versus normal distance from bottom wall for simulation of a turbulent channel flow, $Re_\tau = 590$, RNG k-ε model. 44
2.42 Turbulent kinetic energy dissipation rate versus normal distance from bottom wall for simulation of a turbulent channel flow, $Re_\tau = 590$, RNG k-ε model. 44

3.1 Control file for the lid driven cavity problem with the ILES turbulence model. . . . 47
3.2 A series of refined grids, $32 \times 32 \times 16$, $64 \times 64 \times 32$, and $128 \times 128 \times 64$, for large-eddy simulation of a flow in lid-driven cavity at $Re = 10,000$, $x - y$ plane. 48
3.3 A series of refined grids, $32 \times 32 \times 16$, $64 \times 64 \times 32$, and $128 \times 128 \times 64$, for large-eddy simulation of a flow in lid-driven cavity at $Re = 10,000$, $z - y$ plane. 48
3.4 Time history of global kinetic energy for large-eddy simulation of a flow in lid-driven cavity at $Re = 10,000$, obtained on a series of refined grids, $32 \times 32 \times 16$, $64 \times 64 \times 32$, and $128 \times 128 \times 64$, using ILES model. 48
3.5 Time history of global kinetic energy for large-eddy simulation of a flow in lid-driven cavity at $Re = 10,000$, obtained on a series of refined grids, $32 \times 32 \times 16$, $64 \times 64 \times 32$, and $128 \times 128 \times 64$, using WALE model. 49
3.6 Time history of global kinetic energy for large-eddy simulation of a flow in lid-driven cavity at $Re = 10,000$, obtained on a series of refined grids, $32 \times 32 \times 16$, $64 \times 64 \times 32$, and $128 \times 128 \times 64$, using Smagorinsky model. 49
3.7 Comparisons of mean velocity components $\langle u \rangle / u_b$ and $\langle v \rangle / u_b$ in the spanwise mid-plane with experimental data for large-eddy simulation of a flow in lid-driven cavity at $Re = 10,000$, obtained on a series of refined grids, $32 \times 32 \times 16$, $64 \times 64 \times 32$, and $128 \times 128 \times 64$, using ILES model. 50
3.8 Comparisons of scaled RMS velocity components $10\sqrt{\langle u'u' \rangle}/u_b$ and $10\sqrt{\langle v'v' \rangle}/u_b$ in the spanwise mid-plane with experimental data for large-eddy simulation of a flow in lid-driven cavity at $Re = 10,000$, obtained on a series of refined grids, $32 \times 32 \times 16$, $64 \times 64 \times 32$, and $128 \times 128 \times 64$, using ILES model. 51
3.9 Comparisons of scaled Reynolds stress tensor components $500\langle u'v' \rangle / u_b^2$ in the spanwise mid-plane with experimental data for large-eddy simulation of a flow in lid-driven cavity at $Re = 10,000$, obtained on a series of refined grids, $32 \times 32 \times 16$, $64 \times 64 \times 32$, and $128 \times 128 \times 64$, using ILES model. 52
3.10 Comparisons of mean velocity components $\langle u \rangle / u_b$ and $\langle v \rangle / u_b$ in the spanwise mid-plane with experimental data for large-eddy simulation of a flow in lid-driven cavity at $Re = 10,000$, obtained on a series of refined grids, $32 \times 32 \times 16$, $64 \times 64 \times 32$, and $128 \times 128 \times 64$, using WALE model. 53
3.11 Comparisons of scaled RMS velocity components $10\sqrt{\langle u'u' \rangle}/u_b$ and $10\sqrt{\langle v'v' \rangle}/u_b$ in the spanwise mid-plane with experimental data for large-eddy simulation of a flow in lid-driven cavity at $Re = 10,000$, obtained on a series of refined grids, $32 \times 32 \times 16$, $64 \times 64 \times 32$, and $128 \times 128 \times 64$, using WALE model. 54
3.12 Comparisons of scaled Reynolds stress tensor components $500\langle u'v' \rangle / u_b^2$ in the spanwise mid-plane with experimental data for large-eddy simulation of a flow in lid-driven cavity at $Re = 10,000$, obtained on a series of refined grids, $32 \times 32 \times 16$, $64 \times 64 \times 32$, and $128 \times 128 \times 64$, using WALE model. 55

3.13 Comparisons of mean velocity components $\langle u \rangle / u_b$ and $\langle v \rangle / u_b$ in the spanwise mid-plane with experimental data for large-eddy simulation of a flow in lid-driven cavity at $Re = 10,000$, obtained on a series of refined grids, $32 \times 32 \times 16$, $64 \times 64 \times 32$, and $128 \times 128 \times 64$, using Smagorinsky model. 56
3.14 Comparisons of scaled RMS velocity components $10\sqrt{\langle u'u' \rangle}/u_b$ and $10\sqrt{\langle v'v' \rangle}/u_b$ in the spanwise mid-plane with experimental data for large-eddy simulation of a flow in lid-driven cavity at $Re = 10,000$, obtained on a series of refined grids, $32 \times 32 \times 16$, $64 \times 64 \times 32$, and $128 \times 128 \times 64$, using Smagorinsky model. 57
3.15 Comparisons of scaled Reynolds stress tensor components $500\langle u'v' \rangle / u_b^2$ in the spanwise mid-plane with experimental data for large-eddy simulation of a flow in lid-driven cavity at $Re = 10,000$, obtained on a series of refined grids, $32 \times 32 \times 16$, $64 \times 64 \times 32$, and $128 \times 128 \times 64$, using Smagorinsky model. 58

4.1 Boundary conditions on rod and spacer surfaces, and subchannel boundaries. 60
4.2 Surface meshes for the (a) 7M and (b) 47M grids for the V5H GTRF 3×3 rod bundle. 63
4.3 Instantaneous snapshots of helicity $(\mathbf{v} \cdot \omega)$ isosurfaces for the 2M and 47M Spider meshes. 64
4.4 Instantaneous (a) and mean (b) pressure line plots for different meshes. 64
4.5 (a) RMS pressure integrated over the full length of the central rod for three different meshes, (b) RMS total force on the central rod integrated in 1-inch segments downstream of the mixing vanes. The Star-CCM+ results are from the LES calculations in [9]. 65
4.6 Second moments of the fluctuating velocity field for three different meshes: (a) turbulent kinetic energy along the rod for three different meshes, (b) Reynolds stress along the rod for the 14M mesh. 65
4.7 Total, pressure, and shear force time histories on the central rod and spacer for the 7M Spider mesh: (a) Total force on the central rod, (b) Total force on the spacer, (c) Pressure force on the central rod, (d) Pressure force on the spacer, (e) Shear force on the central rod, and (f) Shear force on the spacer. 66
4.8 Representative control file for 3×3 GTRF LES calculations. 67
4.9 Flow domain for the 5×5 rod bundle showing the rods, the inlet/outlet planes, the support, and the spacer grid. 68
4.10 Domain-average kinetic energy, $\int \rho \mathbf{v} \cdot \mathbf{v}/2 \mathrm{d}\Omega$, vs. time for the 14M 5×5 rod bundle. 69
4.11 Snapshots of the instantaneous helicity field for the (a) 14M and (b) 96M element meshes. 70
4.12 Locations relative to the "weld nugget" used for extracting data along planes 5, 6 and 7. (Reproduced from [18]) without permission.) 71
4.13 Mean axial and lateral velocity profiles at positions A, C, D, E, G and H for the 14M mesh. 72
4.14 Mean axial and lateral velocity profiles at positions A, C, D, E, G and H for the 96M mesh. 74
4.15 Experimental and computed axial (y-direction) time-averaged velocities on plane 5. Velocity magnitude has been scaled relative to the 2.48 m/s inlet velocity. 75
4.16 Experimental and computed axial (y-direction) time-averaged velocities on plane 7. Velocity magnitude has been scaled relative to the 2.48 m/s inlet velocity. 76

4.17 Control file for 5×5 rod-bundle LES calculations. 77

List of Tables

2.1 Convergence rate analysis for Poiseuille flow in a channel for four successively refined grids: $100 \times 5 \times 1$, $200 \times 10 \times 1$, $400 \times 20 \times 1$, and $800 \times 40 \times 1$ 4
2.2 Side set Id's used for the lid-driven skew cavities. 10
2.3 Convergence behavior of the global kinetic energy vs. h for the lid-driven skewed cavities. 14
2.4 Meshes used for the De Vahl Davis benchmark problem 16
2.5 Maximal velocities, mean and maximal Nusselt numbers compared with the extrapolated benchmark results obtained by De Vahl Davis [7]. 19
2.6 Boundary layer thickness of the mesh for steady flow past a flat plate at $Re = 100,000$ 23
2.7 Grids used for simulation of a turbulent channel flow, $Re_\tau = 590$, Spalart-Allmaras model. 36
2.8 Grids used for simulation of a turbulent channel flow, $Re_\tau = 590$, RNG k-ε model. . 36

4.1 Sample points A – H used to extract line-data for comparison with experimental data. 70

Chapter 1

Introduction

Verification testing is part of our software quality control process and ensures that Hydra-TH is solving problems of interest to the Consortium for Advanced Simulation of Lightwater reactors (CASL) program while meeting the necessary design requirements. It is one component of a larger testing infrastructure. This document identifies verification, validation and thermal hydraulics problems of interest to CASL, and summarizes the Hydra-TH solutions to these problems. We anticipate that this document, like the code, will change over time.

This document will have a wide audience of readers from the CASL program and is designed to be a concise report of both test setup and results. Contributors are encouraged to provide additional problems when appropriate, and include references to more in-depth discussions when needed.

The tests are organized by methods and physics to enable a quick survey of code capabilities. Each test has a section in this document with subsections describing why the test is included (§Problem Description), the setup of the test (§Problem Setup), either the control file used to run the test or an example of a control file if more than one was used (§Control File(s)), and pointers to the Exodus-II mesh files used for computation (§Mesh Files). Details regarding keyword input, prescription of boundary conditions, material models, initial conditions, time integrators, etc., may be found in the Hydra-TH User's Manual [2]. All the files required to reproduce the test results are located in the Hydra-TH repository under the `test/verification/FVM/CCIncNavierStokes` directory.

Chapter 2

Incompressible Navier-Stokes 2D Test Problems

2.1 Poiseuille Flow

2.1.1 Problem Description

The objective of this problem is to verify that Hydra-TH can achieve an optimal convergence rate for incompressible laminar flows. The test problem chosen in this case is the steady Poiseuille flow, which represents an exact solution to the full system of two-dimensional incompressible Navier-Stokes equations for a laminar flow in a channel. The velocity distribution at any given streamwise locations is a parabolic profile given by

$$v_{exact} = 12\mu - \frac{dP}{dx}(H - y) \tag{2.1}$$

where $1/\mu = Re$, and H is the height of the channel.

2.1.2 Problem Setup

In this problem, the Reynolds number based on the height of the channel is 100, the pressure gradient based on the length of the channel $dP/dx = -0.12$, and the height of the channel is $H = 1$. The computational domain is bounded from 0 to 20 in x-direction, from 0 to 1 in y-direction, and from 0 to 1 in z-direction. A series of four successively refined hexahedral meshes, consisting of $100 \times 5 \times 1$, $200 \times 10 \times 1$, $400 \times 20 \times 1$, and $800 \times 40 \times 1$ elements, and shown in Figures 2.2(a) through 2.2(d), are used to conduct the convergence study. Readers are suggested to refer to §5.1 of the Hydra-TH User's Manual [2] for more details of the setup. All contour and line plots are based on the cell-centered solution variables. The x-direction velocity and pressure contours for the four successively refined meshes are shown in Figures 2.3(a) through 2.3(d), and 2.4(a) through 2.4(d), respectively. The computed x-velocity distributions on the four successively refined meshes are compared with the exact solution at outflow boundary cells, as shown in Figures 2.5(a) through 2.5(d).

The order of accuracy provided by Hydra-TH can be assessed by computing the slope of the logarithmic L^2 norm of the error function in terms of the logarithmic cell size, where the L^2 error

can be computed as

$$\| v_x - v_{exact} \|_2 = \sqrt{\sum_{i=1}^{ncell} \int_\Omega (v_x - v_{exact})^2 \, d\Omega} = \sqrt{\sum_{i=1}^{ncell} (v_x - v_{exact})^2 \Omega_i} \tag{2.2}$$

where n_{cell} is the total cell number of the mesh and Ω_i is the volume of each cell. Then, the piecewise order or the slope can be computed using two meshes of characteristic cell size h and $h/2$ as follows

$$slope = \frac{\log_{10} errl2_{\frac{h}{2}} - \log_{10} errl2_h}{\log_{10} \frac{h}{2} - \log_{10} h} \tag{2.3}$$

Table 2.1: Convergence rate analysis for Poiseuille flow in a channel for four successively refined grids: $100 \times 5 \times 1$, $200 \times 10 \times 1$, $400 \times 20 \times 1$, and $800 \times 40 \times 1$

Cell Size	$\log_{10}(L^2 - error)$	Order
0.200	-0.58886	—
0.100	-1.23673	2.15218
0.050	-1.81820	1.93159
0.025	-2.41830	1.99350

Table 2.1 shows that the errors and the convergence rate the Hydra-TH results, indicating that Hydra-TH is able to achieve the designed second-order spatial accuracy for solving incompressible Navier-Stokes equations.

2.1.3 Control File

The control file is Poiseuille.cntl, is shown in Figure 2.1.4, and may be found in `2D/poiseuille` test directory.

2.1.4 Mesh Files

The mesh files for the grids used in this study are Poiseuille1.exo, Poiseuille2.exo, Poiseuille3.exo, and Poiseuille4.exo, and may be found in the `2D/poiseuille` directory.

```
title
Re = 100 laminar Poiseuille flow

cc_navierstokes

  nsteps   1000
  deltat   0.001
  term     150.0

  time_integration
    type    fixed_cfl
    CFLinit 1.0
    CFLmax  10.0
    dtmax   0.5
    dtscale 1.025
    thetaa  1.0
    thetak  1.0
    thetaf  1.0
  end

  # Output options
  pltype exodusii
  filetype serial
  plti   50
  ttyi   10

  # Material model definition
  material
    id  1
    rho 1.0
    mu  1.0e-2
  end

  materialset
    id 10
    material 1
    block 1
  end

  plotvar
    elem vel
    elem pressure
    elem volume
    elem density
    elem procid
    elem div
    elem enstrophy
    node vel
    node pressure
  end
```

```
  # Simple IC's
  initial
    velx 0.0
    vely 0.0
    velz 0.0
  end

  # Fixed pressure
  pressure
    sideset 1 -1 2.4
    sideset 2 -1 0.0
  end

  # Velocity BC's
  velocity
   # Inlet
   vely sideset 1 -1 0.0
   velz sideset 1 -1 0.0
   # Top
   velx sideset 3 -1 0.0
   vely sideset 3 -1 0.0
   velz sideset 3 -1 0.0
   # Bottom
   velx sideset 4 -1 0.0
   vely sideset 4 -1 0.0
   velz sideset 4 -1 0.0
   # Back & Front - symmetry in z
   velz sideset 5 -1 0.0
  end

  ppesolver
    type  AMG
    itmax 250
    itchk 1
    coarse_size 100
    diagnostics off
    convergence off
    eps 1.0e-8
  end

  momentumsolver
    type  ILUFGMRES
    itmax 50
    itchk 2
    restart 20
    diagnostics off
    convergence off
    eps   1.0e-8
  end

end

exit
```

Figure 2.1: Control file for laminar flow past a flat plate

CASL-U-2013-0324-000-b

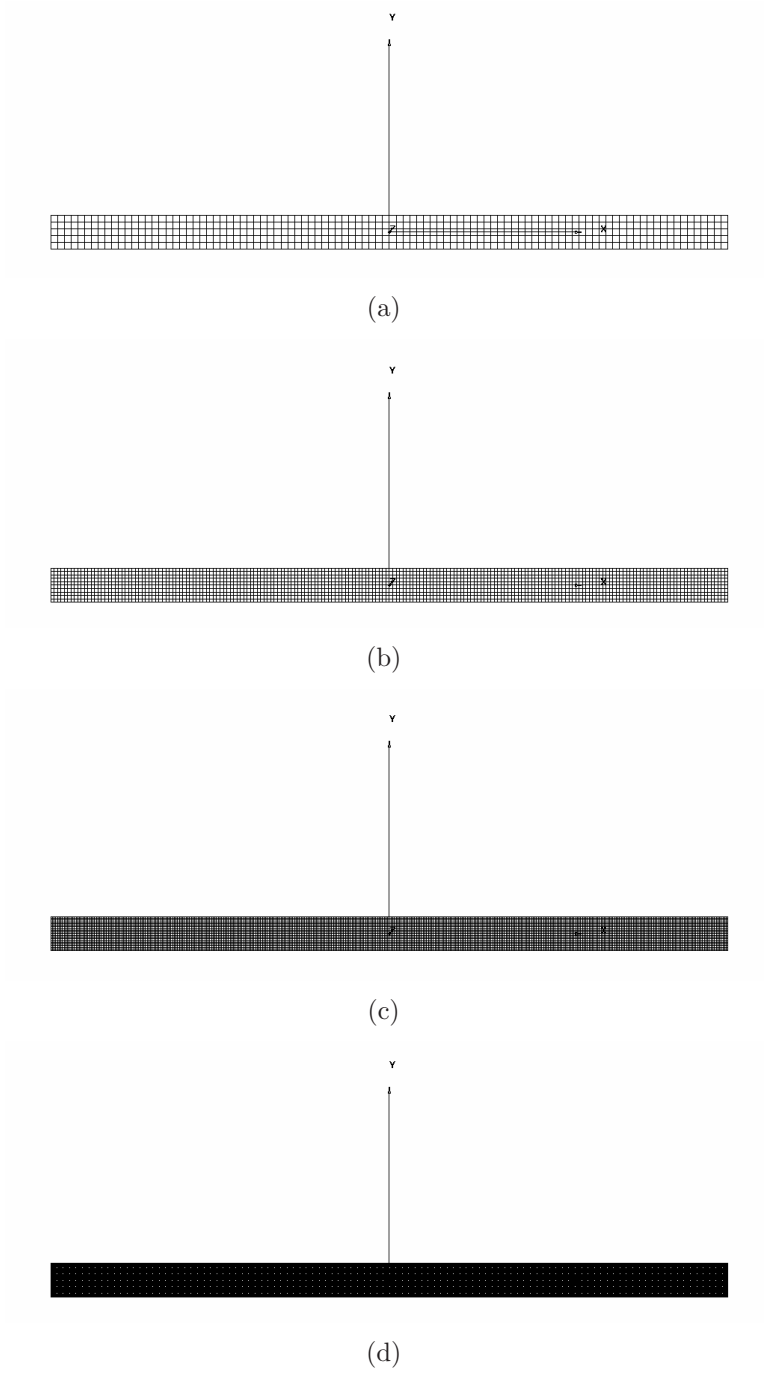

Figure 2.2: Plots of the four successively refined grids for steady Poiseuille flow in a channel: (a) $100 \times 5 \times 1$, (b) $200 \times 10 \times 1$, (c) $400 \times 20 \times 1$ and (d) $800 \times 40 \times 1$

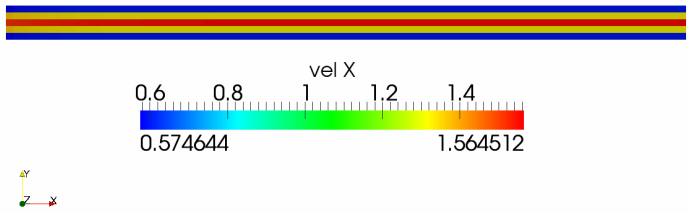

(a)

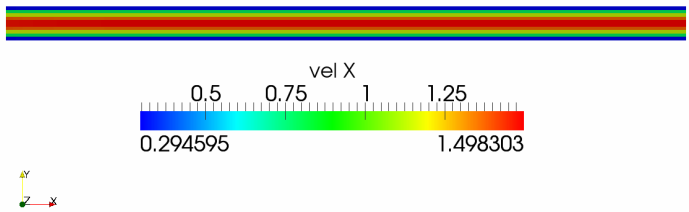

(b)

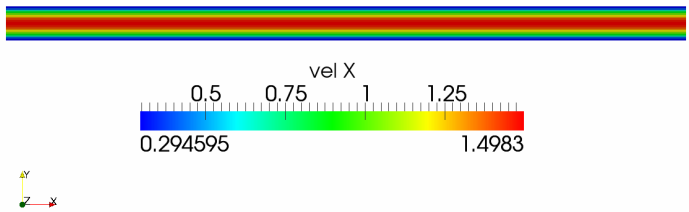

(c)

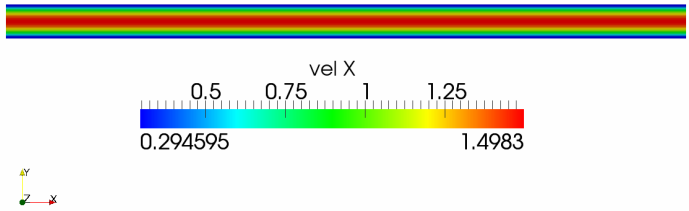

(d)

Figure 2.3: Plots of x-velocity contours of steady Poiseuille flow in a channel for four successively refined grids: (a) $100 \times 5 \times 1$, (b) $200 \times 10 \times 1$, (c) $400 \times 20 \times 1$ and (d) $800 \times 40 \times 1$

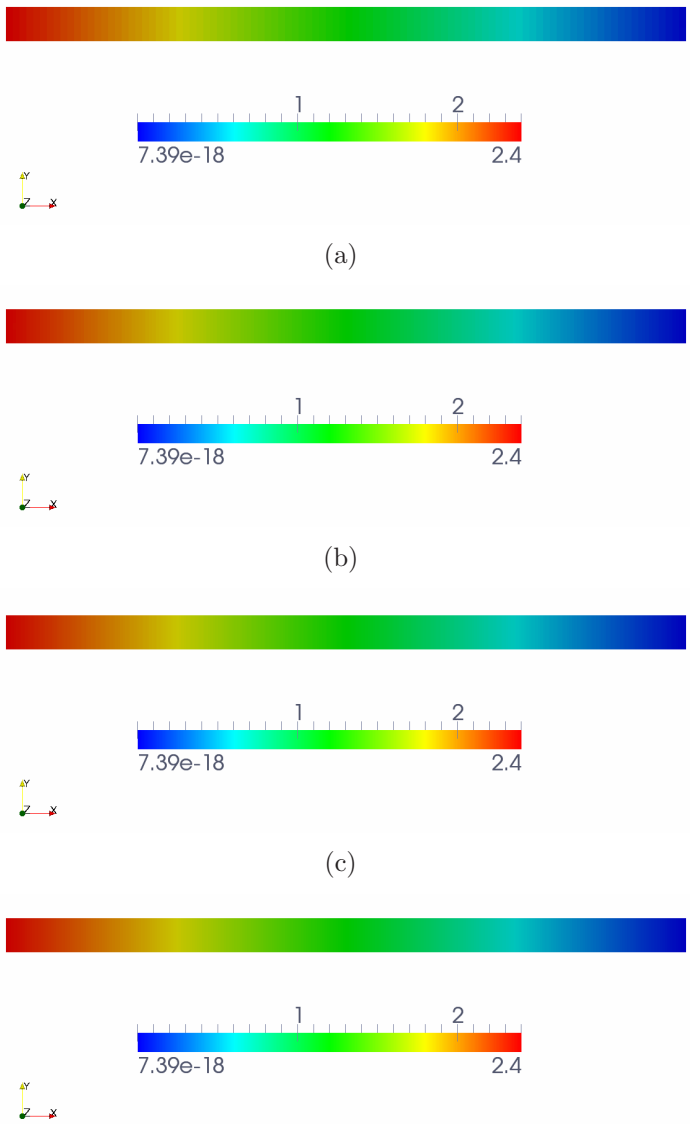

Figure 2.4: Plots of pressure contours of steady Poiseuille flow in a channel for four successively refined grids: (a) $100 \times 5 \times 1$, (b) $200 \times 10 \times 1$, (c) $400 \times 20 \times 1$ and (d) $800 \times 40 \times 1$

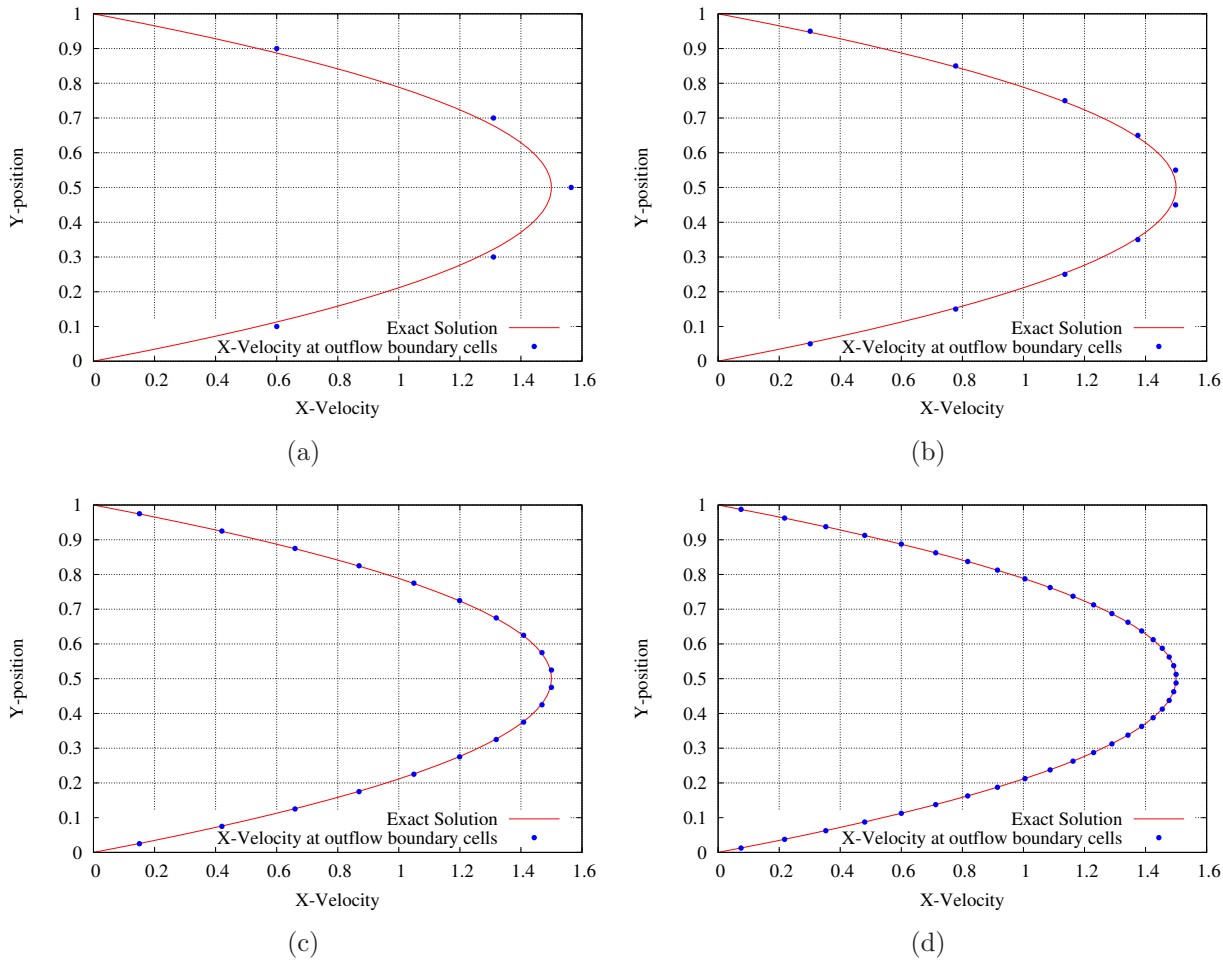

Figure 2.5: Plots of x-velocity profiles at outflow boundary cells of steady Poiseuille flow in a channel for four successively refined grids: (a) $100 \times 5 \times 1$, (b) $200 \times 10 \times 1$, (c) $400 \times 20 \times 1$ and (d) $800 \times 40 \times 1$

2.2 Lid-Driven Skew Cavities

2.2.1 Problem Description

This problem consists of a suite of five lid driven skewed cavity problems based on the work by Erturk and Dursun [10]. Note that the results by Ghia, et al. [11] are also available for the specific 90° lid driven cavity, but a direct comparison with this data is not included here.

2.2.2 Problem Setup

The geometrical configuration for the lid driven cavity is shown generically in Figure 2.6 with α defining the skew angle. On the bottom and side walls, no-slip/no-penetration boundary conditions were prescribed. Along the top "lid", a no-penetration boundary condition along with a unit lid velocity are prescribed. A single nodal pressure was set in the bottom right-hand corner to define the hydrostatic pressure level.

The verification suite consists of five skewed cavities with $\alpha = 15, 30, 45, 60, 90^o$. Each skewed cavity uses three grids with 32×32, 128×128 and 256×256 elements. In order to simplify the prescription of boundary conditions, all of the meshes used a consistent sideset numbering relative to Figure 2.6 as shown in Table 2.2.

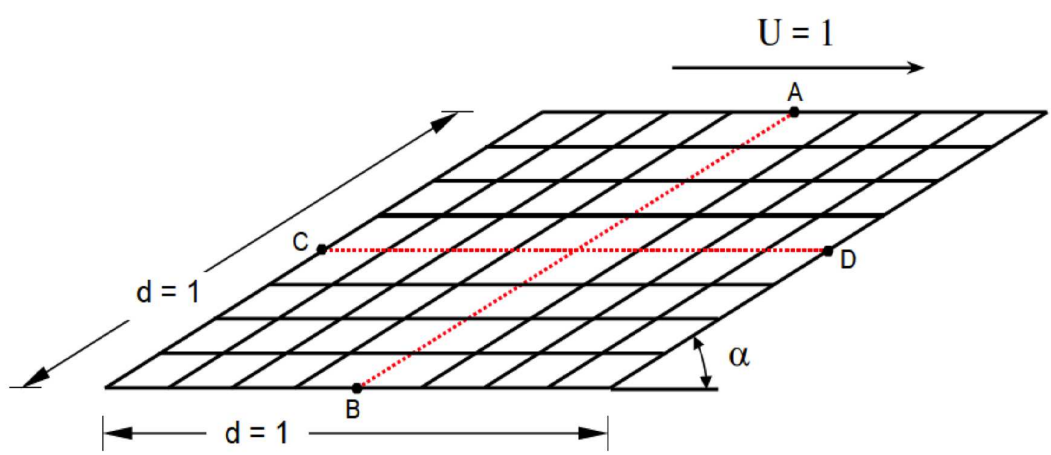

Figure 2.6: Skewed lid driven cavity geometry (reproduced from Erturk and Dursun[10] without permission).

Cavity Side	Side Set Id
Top (A)	4
Bottom (B)	5
Left (C)	1
Right (D)	2
Front/Back	3

Table 2.2: Side set Id's used for the lid-driven skew cavities.

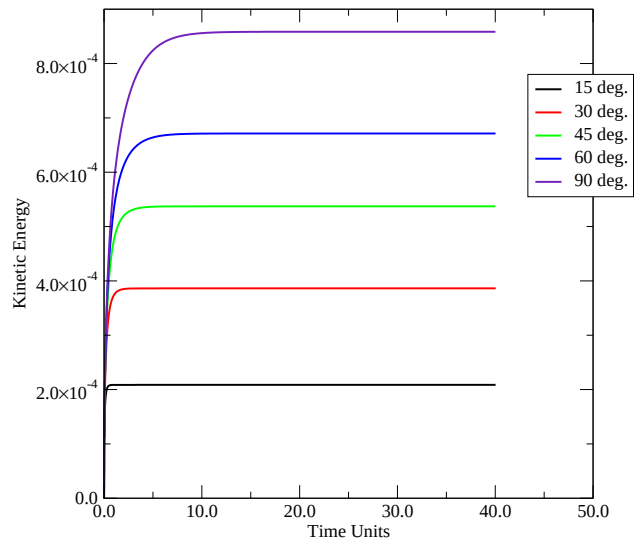

Figure 2.7: Kinetic energy vs. time for the 128×128 grids for $\alpha = 15, 30, 45, 60, 90^o$.

2.2.3 Results

For all computations, $CFL_{max} = 10$ and backward-Euler time integration is used since the goal is a steady-state solution. Time history plots of the global kinetic energy indicate that a steady-state solution is reached by ≈ 10 time units. Note that the diffusional time-scale varies with each skew angle with slightly larger time-scales required for the larger skew angles. All problems for the verification suite are run for 40 time units. The kinetic energy vs. time plots for the 128×128 grids are shown in Figure 2.7. Velocity data is extracted along the red center lines shown in Figure 2.6 for direct comparison with the reference data provided by Erturk and Dursun. The x-velocity profile is plotted against the vertical centerline, and the y-velocity profile is plotted against the horizontal centerline as shown in Figures 2.8 – 2.12.

All of the lid driven cavity problems achieve a steady-state (as verified by the global kinetic energy and velocity time-histories), and this provides a convenient way to assess the convergence behavior as the mesh is refined. All of the cavity meshes used uniform meshing, albeit with severely skewed elements for the 15° cavity. Table 2.3 shows the asymptotic behavior of the kinetic energy as a function of the x-mesh size (h) which indicates $O(h^2)$ convergence in all velocity components for all of the skew angles.

2.2.4 Control Files

An example control, ldc_Re100.cntl, is shown in Figure 2.13. All of the control files may be found in the `2D/lid_driven_cavity` directory.

CASL-U-2013-0324-000-b

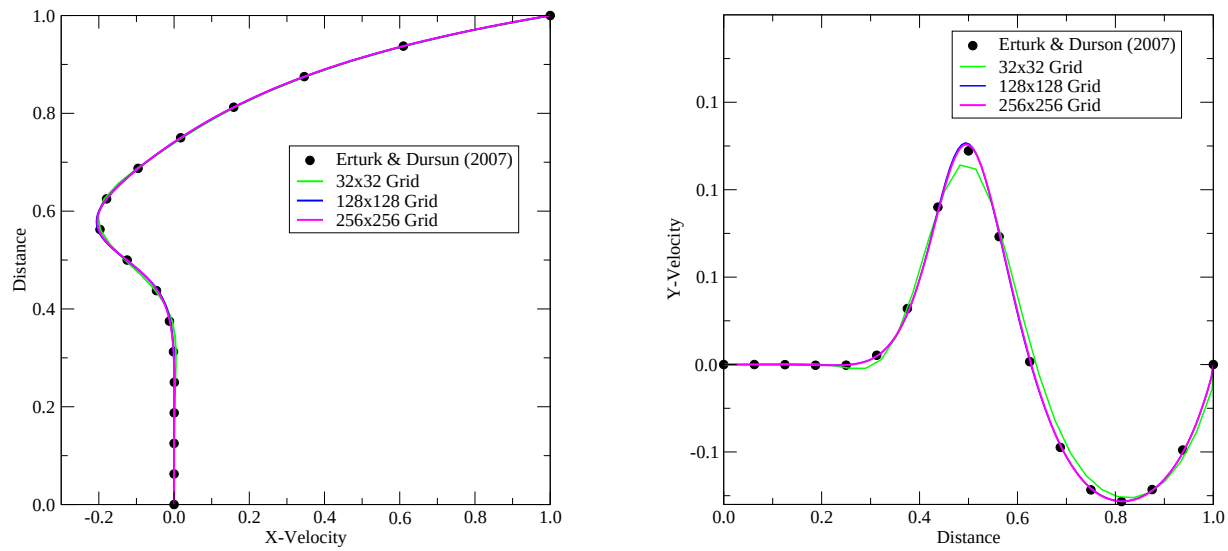

(a) (b)

Figure 2.8: 15° lid-driven cavity: (a) x-velocity, (b) y-velocity.

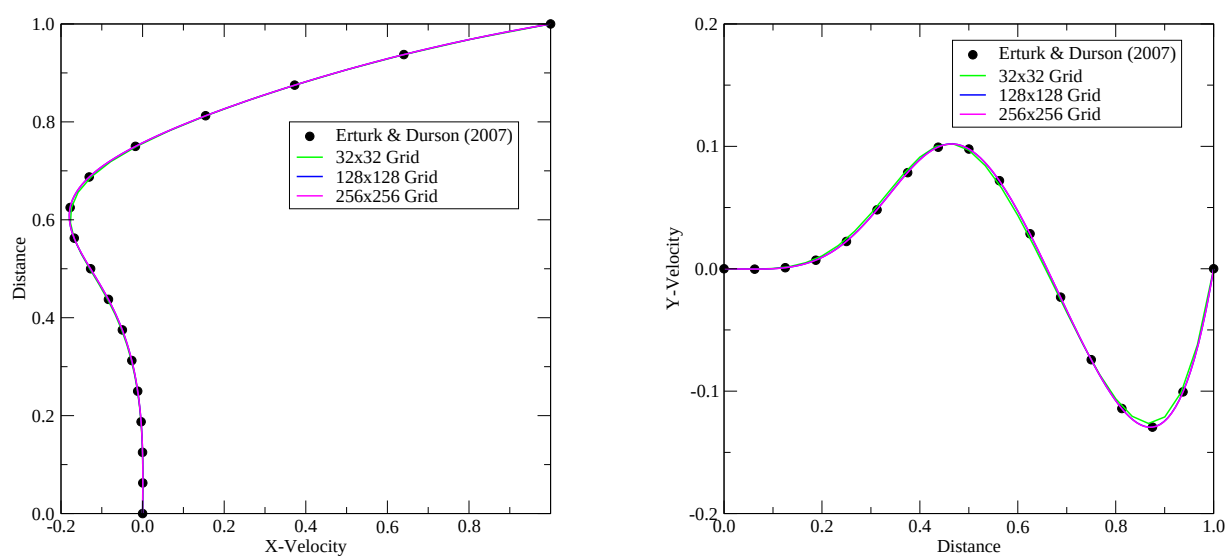

(a) (b)

Figure 2.9: 30° lid-driven cavity: (a) x-velocity, (b) y-velocity.

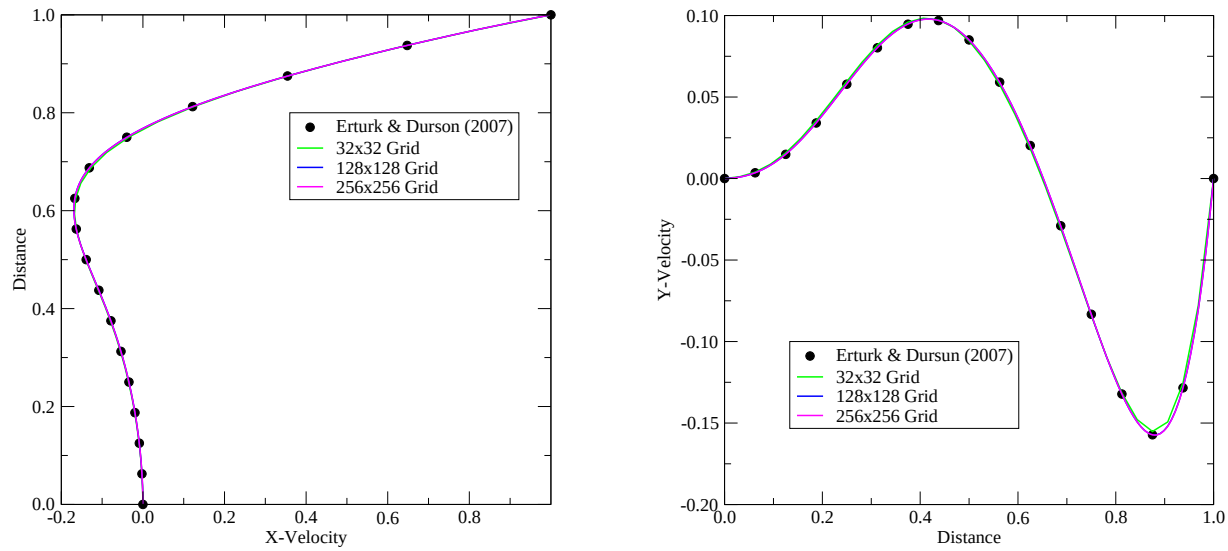

(a) (b)

Figure 2.10: 45° lid-driven cavity: (a) x-velocity, (b) y-velocity.

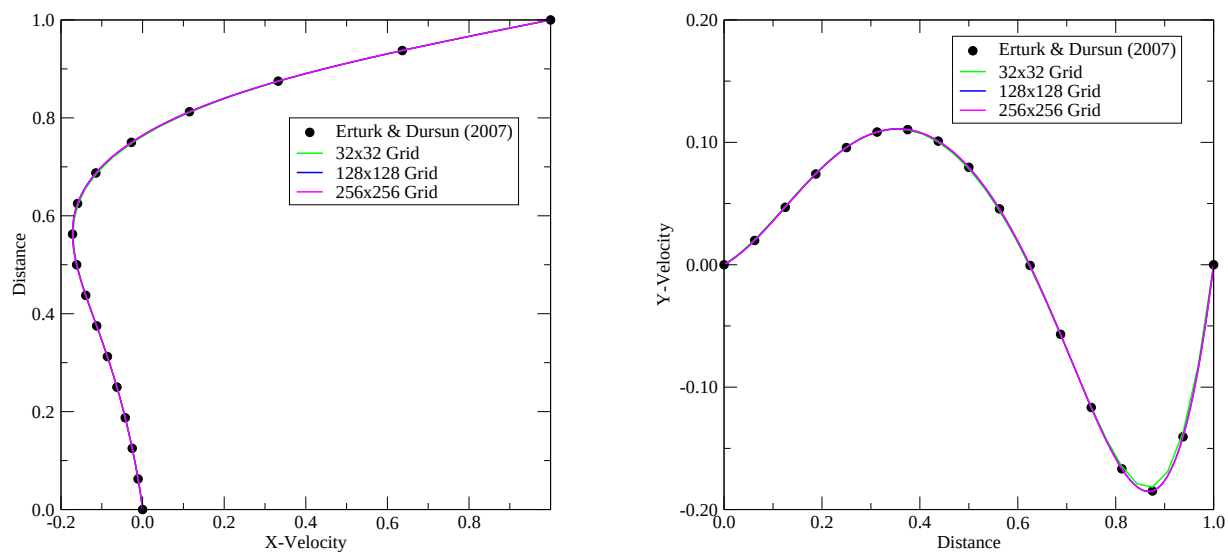

(a) (b)

Figure 2.11: 60° lid-driven cavity: (a) x-velocity, (b) y-velocity.

Cavity Angle	Global Kinetic Energy Correlation
15°	$0.00020907 - 0.006877\ h^2$
30°	$0.00038731 - 0.010046\ h^2$
45°	$0.00053854 - 0.014590\ h^2$
60°	$0.00067314 - 0.019690\ h^2$
90°	$0.00086136 - 0.029630\ h^2$

Table 2.3: Convergence behavior of the global kinetic energy vs. h for the lid-driven skewed cavities.

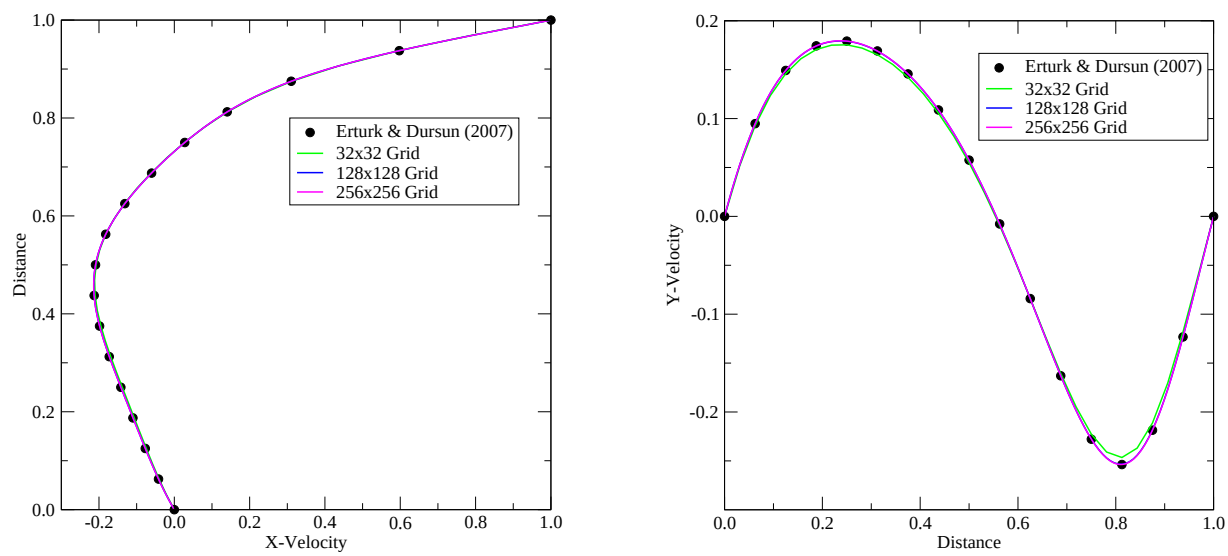

(a) (b)

Figure 2.12: 90° lid-driven cavity: (a) x-velocity, (b) y-velocity.

2.2.5 Mesh Files

The mesh files may be found in the `2D/lid_driven_cavity` directory and are named ldcα_32x32.exo, ldcα_128x128.exo, dcα_256x256.exo where $\alpha = 15,\ 30,\ 45,\ 60,\ 90^o$.

```
# This is a comment

title
Re=100 lid-driven cavity

cc_navierstokes

  nsteps  1200
  deltat  0.01
  term    40.0

  time_integration
    type    fixed_cfl
    CFLinit 1.0
    CFLmax  10.0
    dtmax   0.05
    dtscale 1.025
    thetaa  1.0
    thetak  1.0
    thetaf  1.0
  end

  # Output options
  pltype exodusii
  filetype serial
  plti   20
  ttyi   20
  dump   0

  # Material model setup & assignment to sets
  material
    id  1
    rho 1.0
    mu  1.0e-2
  end

  materialset
    id 10
    material 1
    block 1
  end

  plotvar
    elem density
    elem vel
    elem procid
    elem div
    node lambda
    node pressure
    node vel
    node vorticity
  end
```

```
# Simple IC's
  initial
    velx 0.0
    vely 0.0
    velz 0.0
  end

  hydrostat
    nodeset 2 -1 0.0
  end

  velocity
    velx sideset 1 -1 0.0 # Left wall
    vely sideset 1 -1 0.0
    velz sideset 1 -1 0.0
    velx sideset 2 -1 0.0 # Right wall
    vely sideset 2 -1 0.0
    velz sideset 2 -1 0.0
    velz sideset 3 -1 0.0 # Front/back
    velx sideset 4 -1 1.0 # Top wall (lid)
    vely sideset 4 -1 0.0
    velz sideset 4 -1 0.0
    velx sideset 5 -1 0.0 # Bottom wall
    vely sideset 5 -1 0.0
    velz sideset 5 -1 0.0
  end

  ppesolver
    type  AMG
    itmax 100
    itchk 1
    coarse_size 1000
    diagnostics off
    convergence off
    eps   1.0e-5
  end

  momentumsolver
    type  ILUFGMRES
    itmax 50
    itchk 2
    restart 45
    diagnostics off
    convergence off
    eps   1.0e-5
  end

end

exit
```

Figure 2.13: A representative control file for the lid-driven cavity problem.

CASL-U-2013-0324-000-b

2.3 Natural Convection in a Square Cavity

2.3.1 Problem Description

The thermal cavity benchmark introduced by De Vahl Davis [8, 7] is used here to demonstrate an application with buoyancy-driven flow, and the use of surface output to calculate the wall heat transfer.

2.3.2 Problem Setup

Figure 2.14 shows the computational domain, mesh, and sets used for the differentially heated cavity. In this example, a series of 5 meshes are provided for this example as shown in Table 2.4.

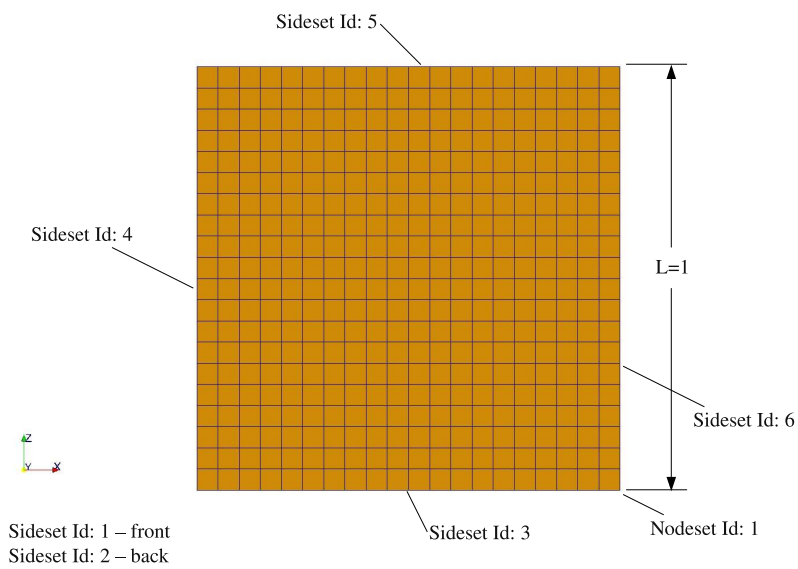

Figure 2.14: 20 x 20 thermal cavity mesh.

Mesh	Mesh Size	h
A	20×20	5.000E-2
B	40×40	2.500E-2
D	80×80	1.250E-2
D	160×160	6.250E-3
E	320×320	3.125E-3

Table 2.4: Meshes used for the De Vahl Davis benchmark problem

The non-dimensional governing equations for time-dependent thermal convection (in vector form) are the incompressible Navier-Stokes equations, conservation of mass, and the energy equation in terms of temperature:

$$\frac{\partial \mathbf{v}}{\partial t} + \mathbf{v} \cdot \nabla \mathbf{v} = -\nabla P + Pr \nabla^2 \mathbf{v} + RaPr\hat{k}\theta, \tag{2.4}$$

$$\nabla \cdot \mathbf{v} = 0, \tag{2.5}$$

and

$$\frac{\partial \theta}{\partial t} + \mathbf{v} \cdot \nabla \theta = \nabla^2 \theta, \tag{2.6}$$

where $\mathbf{v}$, P and θ are the velocity, the deviation from hydrostatic pressure, and temperature respectively, and $\hat{k}$ the unit vector in the z-direction. These non-dimensional equations were obtained using the characteristic length L, velocity $V = \alpha/L$, time scale $\tau = L^2/\alpha$, and pressure $\tilde{P} = \rho V^2$ as described in De Vahl Davis [7]. Here, ρ is the mass density, g the gravitational acceleration, $\alpha = k/\rho C_p$ is the thermal diffusivity, and ν is the kinematic viscosity. The Prandtl number is $Pr = \nu/\alpha$ and fixed at $Pr = 0.71$. The Rayleigh number is

$$Ra = \frac{g\beta(T_h - T_c)L^3}{\nu\alpha}, \tag{2.7}$$

where $T_h - T_c$ is the temperature difference between the hot and cold walls, and β the coefficient of thermal expansion. The non-dimensional temperature is defined in terms of the wall temperature difference

$$\theta = \frac{T - T_c}{T_h - T_c}, \tag{2.8}$$

where T_h is the prescribed temperature of the hot wall, and T_c is the temperature of the cold wall.

The boundary conditions for this problem consist of no-slip and no-penetration walls with the top and bottom walls insulated. The left wall is held at hot temperature, and the right wall at the cold temperature corresponding to $\theta = 1$ along $x = 0$ and $\theta = 0$ along $x = 1$. The initial conditions are prescribed with $\mathbf{v} = \mathbf{0}$ and $T = (T_h + T_c)/2$ which corresponds to $\theta(\mathbf{x}, 0) = 1/2$. The control file for the $Ra = 10^4$ case using the 80×80 grid is shown in Figure 2.15. Here, the hydrostatic pressure is prescribed at a single node (using a nodeset) at the lower right-hand corner of the differentially-heated cavity.

2.3.3 Results

A series of 4 calculations are presented below for $10^3 \leq Ra \leq 10^6$ using meshes B – E. In each calculation, the total duration of the calculation is 2.0 time units which corresponds to twice the diffusional time-scale for the differentially-heated cavity. This is sufficient for the flow to establish steady-state conditions. As illustrated in the control file, a backward-Euler time integrator is selected with `CFLmax` = 40. An initial time step `deltat` = $1.0e{-}3$ is used to permit a smooth startup during the early time period where heat conduction dominates the thermal-convective process.

Time-integration is carried out until an essentially steady-state condition results. This is easily monitored in terms of time-history data for the integrated wall heat transfer rate, velocity, temperature and kinetic energy. The use of the **histvar** – **end** block in the control file activates time-history data to monitor the velocity and temperature at the elements at the mid-side of the vertical walls, and to output the integrated heat transfer rate on the heated wall. Figure 2.16(a) shows the variation in the Nusselt number along the vertical heated wall for the Rayleigh numbers considered here. Figure 2.16(b) shows the time-history of the kinetic energy. From this plot, it

CASL-U-2013-0324-000-b

```
title
Ra=1.0e+3, Pr=0.71 De Vahl Davis benchmark

cc_navierstokes

  nsteps  2000
  deltat  1.0e-3
  term    2.0

  time_integration
    type    fixed_cfl
    CFLinit 1.0
    CFLmax  40.0
    dtmax   0.25
    dtscale 1.025
    thetaa  1.0
    thetak  1.0
    thetaf  1.0
  end

  # Output options
  plti 100

  # Energy equation
  energy temperature

  # Material model setup
  material
    id  1
    rho 1.0
    Cp  1.0
    mu  0.71
    k11 1.0
    beta 7.1e+2
    Tref 0.5
  end

  materialset
    id 10
    material 1
    block 1
  end

  plotvar
    elem density
    elem vel
    elem procid
    elem div
    elem temp
    node lambda
    node pressure
    node vel
    node vorticity
    node temp
    side 4 heatflux
  end

  histvar
    elem 40  vel
    elem 40  temp
    elem 6359 vel
    elem 6359 temp
    side 4 heatflow
  end

  # Simple IC's
  initial
    velx 0.0
    vely 0.0
    velz 0.0
    temp 0.5
  end

  # Boussinesq body force
  boussinesqforce
    gx  0.0
    gy  0.0
    gz -1.0
  end

  velocity
    # Front wall
    vely sideset 1 -1 0.0
    # Back wall
    vely sideset 2 -1 0.0
    # Bottom wall
    velx sideset 3 -1 0.0
    vely sideset 3 -1 0.0
    velz sideset 3 -1 0.0
    # Left wall
    velx sideset 4 -1 0.0
    vely sideset 4 -1 0.0
    velz sideset 4 -1 0.0
    # Top wall
    velx sideset 5 -1 0.0
    vely sideset 5 -1 0.0
    velz sideset 5 -1 0.0
    # Right wall
    velx sideset 6 -1 0.0
    vely sideset 6 -1 0.0
    velz sideset 6 -1 0.0
  end

  temperature
    # Left Wall
    sideset 4 -1 1.0
    # Right Wall
    sideset 6 -1 0.0
  end

  hydrostat
    nodeset 1 -1 0.0
  end

  ppesolver
    type  AMG
    itmax 100
    itchk 1
    coarse_size 1000
    diagnostics off
    convergence off
    eps   1.0e-8
  end

  momentumsolver
    type  ILUFGMRES
    itmax 50
    itchk 2
    restart 45
    diagnostics off
    convergence off
    eps   1.0e-8
  end

end

exit
```

Figure 2.15: Control file for the $Ra = 10^3$ differentially heated cavity.

is clear that an asymptotic steady-state flow is achieved by approximately 1 time unit. This was confirmed by checking the velocity and temperature time-histories. Figure 2.16(c) and (d) show the x- and y-velocity profiles along the vertical and horizontal centerlines of the cavity respectively. Figure 2.17 shows the temperature distribution for the four Rayleigh numbers.

Pointwise comparison data is presented in Table 2.5 using the data obtained by Richardson extrapolation by De Vahl Davis [7]. Here, the minimum and maximum velocities are computed along the horizontal and vertical centerlines of the cavity.

The mean Nusselt number is computed as

$$\overline{Nu} = \frac{1}{A} \int_{\Gamma} \nabla\theta \cdot \mathbf{n} \, d\Gamma \tag{2.9}$$

where A is the surface area. For this comparison, the `heatflow` time-history request results in the output of the integrated non-dimensional heat flow over the heated surface. For all computations, a z-dimension of $\Delta z = 0.0125$ was used with $L = 1$ resulting in an area $A = 0.0125$. In order to compute the mean Nusselt number, the `heatflow` output is scaled by $1/A$. The minimum and maximum Nusselt numbers pointwise correspond to the non-dimensional output requested with the `heatflux` plot variable output. Here, the minimum/maximum Nusselt numbers were extracted from the non-dimensional heat flux distribution along the heated wall. As can be seen, for the selection of meshes used here, there is very good agreement between the results computed with Hydra-TH and the the De Vahl Davis benchmark data.

	Rayleigh Number (Ra)							
	10^3		10^4		10^5		10^6	
	Ref. [7]	80×80	Ref. [7]	160×160	Ref. [7]	320×320	Ref. [7]	320×320
$v_{x_{max}}$	3.659	3.648	16.178	16.179	34.73	34.79	64.63	64.91
$v_{z_{max}}$	3.697	3.692	19.617	19.574	68.59	68.62	219.36	220.33
$\overline{Nu}$	1.118	1.118	2.243	2.246	4.519	4.523	8.800	8.841
Nu_{min}	0.692	0.691	0.586	0.585	0.729	0.727	0.989	0.978
Nu_{max}	1.505	1.507	3.528	3.536	7.717	7.727	17.925	17.643

Table 2.5: Maximal velocities, mean and maximal Nusselt numbers compared with the extrapolated benchmark results obtained by De Vahl Davis [7].

2.3.4 Control Files

The control files may be found in the `2D/diff_heated_cavity` directory. They are named: dd_20x20_Ra1e3.cntl, dd_40x40_Ra1e3.cntl, dd_80x80_Ra1e3.cntl, dd_160x160_Ra1e4.cntl, dd_320x320_Ra1e5.cntl, and dd_320x320_Ra1e6.cntl

2.3.5 Mesh Files

The mesh files may be found in the `2D/diff_heated_cavity` directory. They are named: dd_20x20.exo, dd_40x40.exo, dd_80x80.exo, dd_160x160.exo, and dd_320x320.exo.

CASL-U-2013-0324-000-b

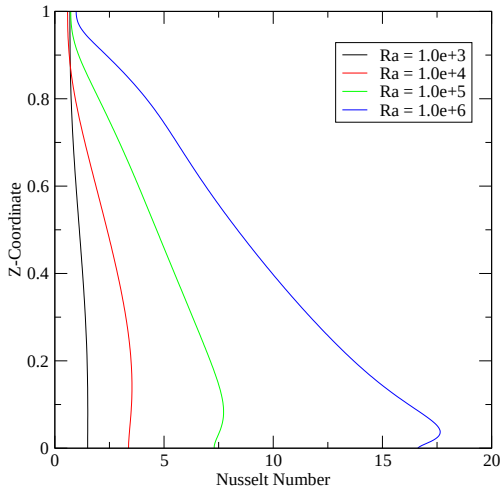

(a)

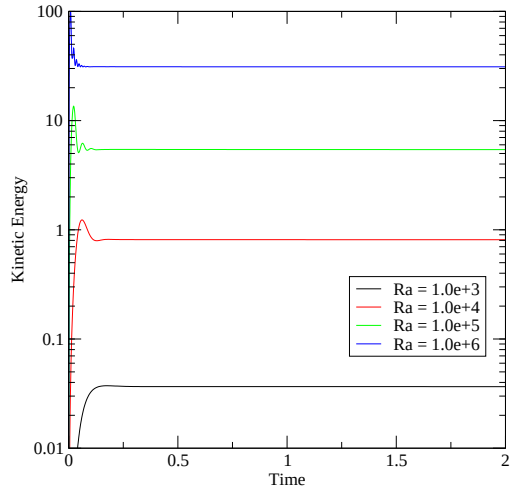

(b)

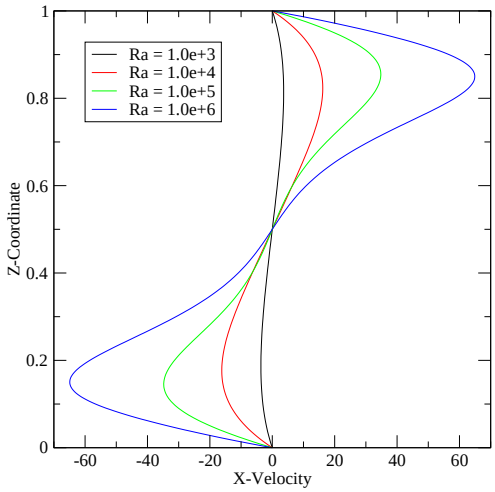

(c)

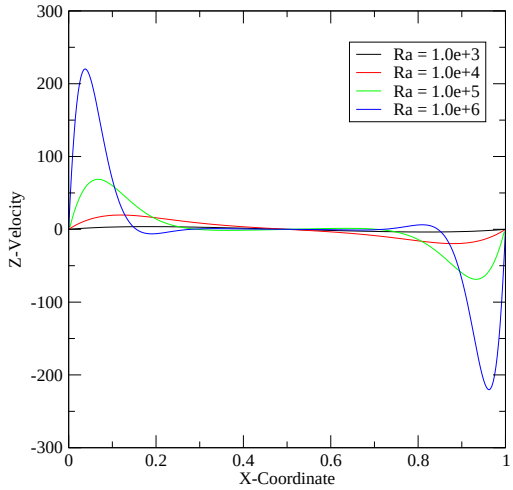

(d)

Figure 2.16: (a) Nusselt number profile along vertical heated wall, (b) global kinetic energy time history, (c) x velocity along vertical centerline, and (d) z-velocity along the horizontal centerline for $Ra = 10^3, 10^4, 10^5, 10^6$.

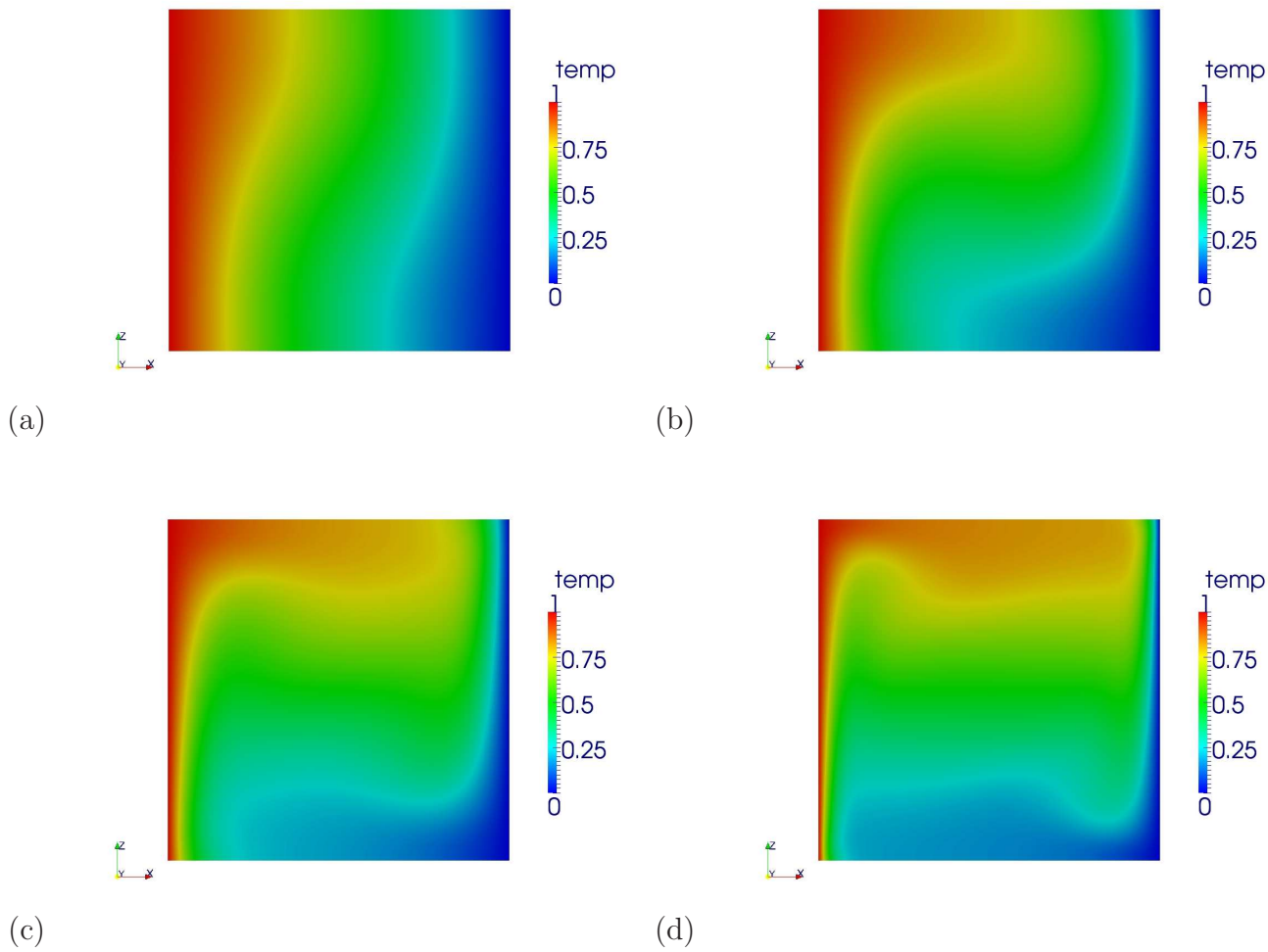

Figure 2.17: Temperature distribution at $t = 2$ time units for (a) $Ra = 10^3$ using mesh B, (b) $Ra = 10^4$ using mesh C, (c) $Ra = 10^5$ using mesh D, and (d) $Ra = 10^6$ using mesh E.

CASL-U-2013-0324-000-b

2.4 Flow Past A Flat Plate

2.4.1 Problem Description

The objective of this problem is to demonstrate the effect that the grid stretching ratio (SR) normal to a no-slip surface can have on the quality of solution for incompressible boundary layer flows. The test problem chosen in this case is the steady flow past a flat plate, in which the numerical solution can be compared with the classical Blasius solution.

2.4.2 Problem Setup

In this experiment, the Reynolds number based on the length of the flat plate is $Re = 100,000$. The computational domain is bounded from -0.5 to 1.0 along the x-direction, from 0 to 1.0 along the y-direction, and from 0 to 0.1 along the z-direction. The no-slip/no-penetration plate surface starts at point $(0, 0, z)$ and extends to $(1, 0, z)$. The first three hexahedral grids used in this computation have the same number of cells $(25 + 50) \times 30 \times 1$, with $25 \times 30 \times 1$ cells ahead of the flat plate and $50 \times 30 \times 1$ cells for the flat plate, the same distribution of the grid points in the x-direction, but a different distribution of grid points in the y-direction. In order to cluster points near the flat plate, the point distribution in the y-direction follows a geometric stretching. The stretching ratio (SR) is the ratio of the heights of two successive elements in the plate-normal direction. An SR value of 1.15, 1.20 and 1.30 is used for the three grids in the computation, respectively. The grids are plotted in Figures 2.19(a) through 2.19(c). The computational grids were generated with Gridgen V15.17 and exported in the Exodus-II format for Hydra-TH.

A quantitative description of the mesh in the boundary layer is shown in Table 2.6. For example, for the grid with an SR of 1.15, the height of the first element is 2.3002×10^{-3}, and is also characterized with the normalized height of $y^+ = 12.35$. As a result, the grid with an SR of 1.30 provides the best grid resolution in the boundary layer region.

The inflow boundary condition when $x = 0$ is prescribed with $v = (1, 0, 0)$. No-slip and no-penetration conditions $v = (0, 0, 0)$ are prescribed when $y = 0$ for $x \in [0, 1]$. A slip condition is prescribed along the bottom side of the domain for $x \in [-0.5, 0]$ with $v_y = 0$. Symmetry conditions are prescribed in the 1-cell thick region with $v_z = 0$. The pressure at outflow boundary is prescribed to be $P = 0$ on the top side ($y = 1$) and right side ($x = 1$).

By default, $\frac{\partial v}{\partial n} = 0$ and $p = 0$ is prescribed at the outflow boundary. These conditions do not match the exact Blasius solution. For this reason in addition to the traditional setup of this problem, another set of computational domains are defined by extending the right boundary, and also the end of flat plate to 1.5 along the x-direction. Another three grids where 3 grid points are equally spaced for $x \in (1, 1.5)$ as shown in Figures 2.25(a) through 2.25(c).

2.4.3 Computational Results

In this section, results from both grid sets are presented. All plots are computed using cell-centered data, and the velocity profiles are plotted with the Blasius boundary solution for comparison.

Figure 2.20 shows the time history of kinetic energy obtained from the solutions on three grids with a unit plate length. As one can observe, the kinetic energy computed from the grid of $SR = 1.15$ is clearly lower than from the other two grids, indicating an under-resolved boundary layer. Figure

2.21 shows the logarithmic plots of the computed skin friction coefficient c_f distributions along the flat plate $x \in [0, 1]$. The skin friction coefficient c_f is defined by

$$c_f = \frac{\tau_w}{\frac{1}{2}\rho U_\infty^2}$$

where τ_w is the local wall shear stress, ρ is the fluid density ($\rho = 1$) and U_∞ is the free-stream velocity ($U_\infty = 1$). The wall shear stress τ_w is given by

$$\tau_w = \mu \left(\frac{\partial u}{\partial y}\right)_{y=0} \approx \mu \frac{u_w}{\Delta y_w}$$

where μ is the dynamic viscosity ($\mu = \frac{1}{Re}$), u_w is the $x-$direction flow velocity at the center of the cell adjacent to plat plate, and Δy_w is the y coordinate of the corresponding cell center (Δy_w equals half of the first layer height). The cell-centered flow variables are extracted from the Hydra-TH generated *plot* file using ParaView (`www.paraview.org`), and the presented figures are plotted using GNUPlot (`www.gnuplot.info`). As expected, the grid of $SR = 1.30$ provided the best prediction of c_f. The grid with $SR = 1.20$ over-predicted the c_f distribution near the plate leading edge due to the insufficient grid resolution. The grid with $SR = 1.15$ predicted the worst c_f distribution because of a very coarse grid near the leading edge region.

Figures 2.22 through 2.24 show the plots of computed v_x and v_y profiles along the cells cut through by plane of $x = 0.10$, $x = 0.50$ and $x = 0.99$ in the boundary layer region. Similar to c_f results the grid with $SR = 1.15$ is under resolved and hence over-predicts v_y at $x = 0.1$ and 0.5. The velocity component in the y-direction improves for $SR = 1.20$ and 1.30. However at $x = 0.99$, the cells are adjacent to the outflow boundary, and since $\frac{\partial v}{\partial n} = 0$ at this outflow, the velocity results demonstrate that the Blasius solution can not be matched.

The comparison to Blasius improves for the extended plate grid, as shown in Figures 2.28 through 2.30. Here the outflow boundary has moved away from $x = 0.99$ and the v_y now matches the Blasius solution. The kinetic energy and skin friction results, plotted in Figures 2.26 and 2.27, remain relatively unchanged from the previous grid definitions.

Table 2.6: Boundary layer thickness of the mesh for steady flow past a flat plate at $Re = 100,000$

Stretching Ratio (SR)	Height of the first layer	y^+ of the first layer
1.15	2.3002×10^{-3}	12.35
1.20	8.4611×10^{-4}	4.542
1.30	1.1455×10^{-4}	0.615

2.4.4 Control File

The control file, `blasius.cntl` may be found in the `2D/blasius` directory.

CASL-U-2013-0324-000-b

2.4.5 Mesh Files

The mesh files may be found in the `2D/blasius` directory, and are named blasius0115.exo, blasius0120.exo, blasius0130.exo, and blasius0115_3blk.exo, blasius0120_3blk.exo, blasius0130_3blk.exo.

```
title
Flow_past_a_flat_plate

cc_navierstokes

  nsteps 2000
  deltat 1.0e-1
  term   10.0

  time_integration
    type    fixed_cfl
    CFLinit 1.0
    CFLmax  100.0
    dtmax   0.2
    dtscale 1.025
    thetaa  1.0
    thetak  1.0
    thetaf  1.0
  end

  # Output options
  pltype exodusii
  filetype serial
  plti   100
  ttyi   1
  dump   100

  # Material model setup
  material
    id  1
    rho 1
    mu  1.0e-5
  end

  materialset
    id 10
    material 1
    block 1
    block 2
  end

  plotvar
    elem vel
    elem pressure
    node vel
    node pressure
  end

  # Simple IC's
  initial
    velx  1.0
    vely  0.0
    velz  0.0
  end

  velocity
    # plate surface (x=[0, 1]) (no-slip wall)
    velx sideset 1 -1  0.0
    vely sideset 1 -1  0.0
    velz sideset 1 -1  0.0
    # inflow plane
    velx sideset 2 -1  1.0
    vely sideset 2 -1  0.0
    velz sideset 2 -1  0.0
    # bottom plane (x=[-0.5, 0]) (slip wall)
    vely sideset 3 -1  0.0
    # front & back plane (symmetry)
    velz sideset 4 -1  0.0
  end

  # top & outflow plane
  pressure
    sideset 5 -1 0.0
  end

  ppesolver
    type  AMG
    amgpc HYPRE
    itmax 50
    itchk 1
    strong_threshold 0.6
    diagnostics off
    convergence off
    coarse_size 100
    eps 1.0e-10
  end

  momentumsolver
    type  ILUFGMRES
    itmax 50
    itchk 2
    restart 20
    eps   1.0e-5
  end

  transportsolver
    type  ILUFGMRES
    itmax 50
    itchk 2
    restart 20
    eps   1.0e-5
  end

end

exit
```

Figure 2.18: Control file for laminar flow past a flat plate

CASL-U-2013-0324-000-b

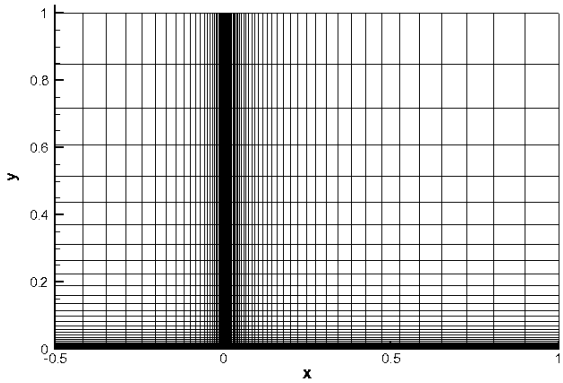

(a)

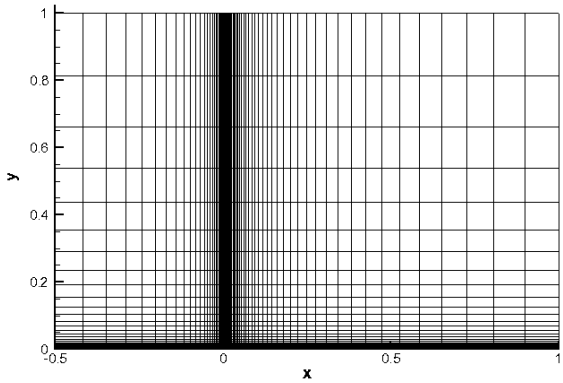

(b)

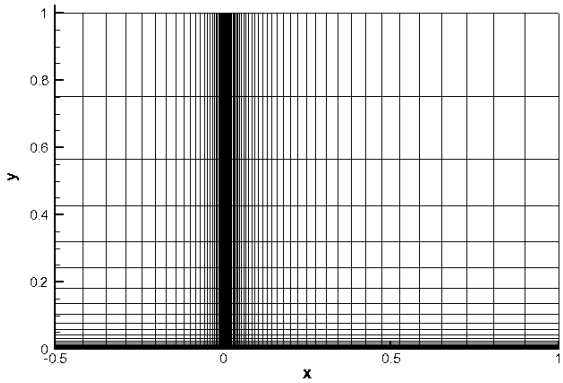

(c)

Figure 2.19: Plot of the $(25 + 50) \times 30 \times 1$ hexahedral grids for steady flow past a flat plate at $Re = 100,000$: (a) $SR = 1.15$ in y-direction; (b) $SR = 1.20$ in y-direction; (c) $SR = 1.30$ in y-direction

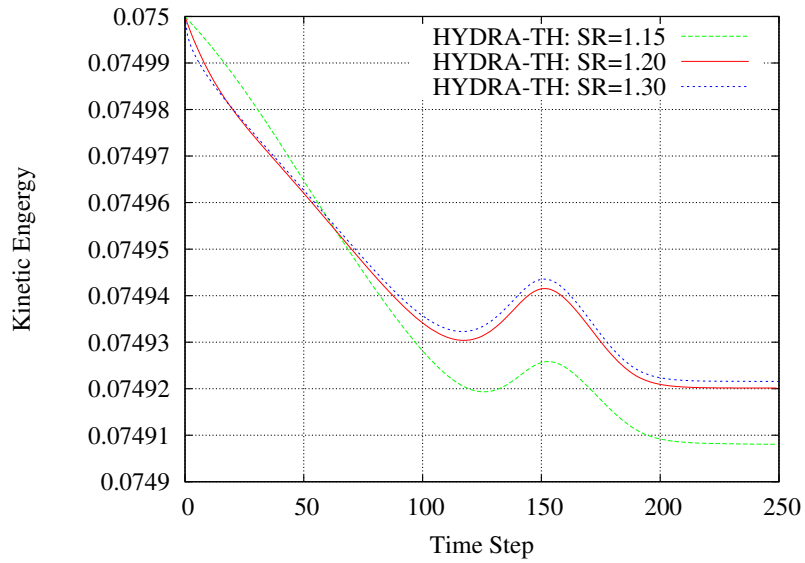

Figure 2.20: Time history plots for kinetic energy obtained on the $(25 + 50) \times 30 \times 1$ hexahedral grids

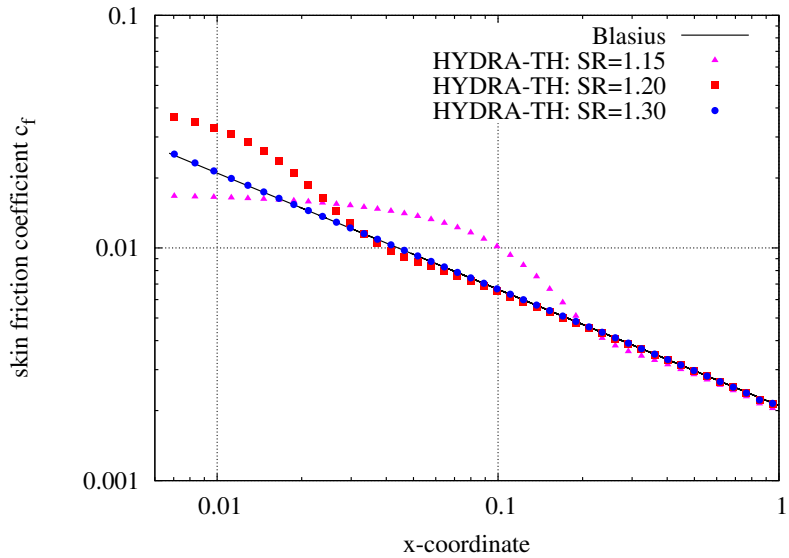

Figure 2.21: Logarithmic plot of the computed skin friction coefficient distribution obtained on the $(25 + 50) \times 30 \times 1$ hexahedral grids compared with the analytical solution along the flat plate $x = [0, 1]$

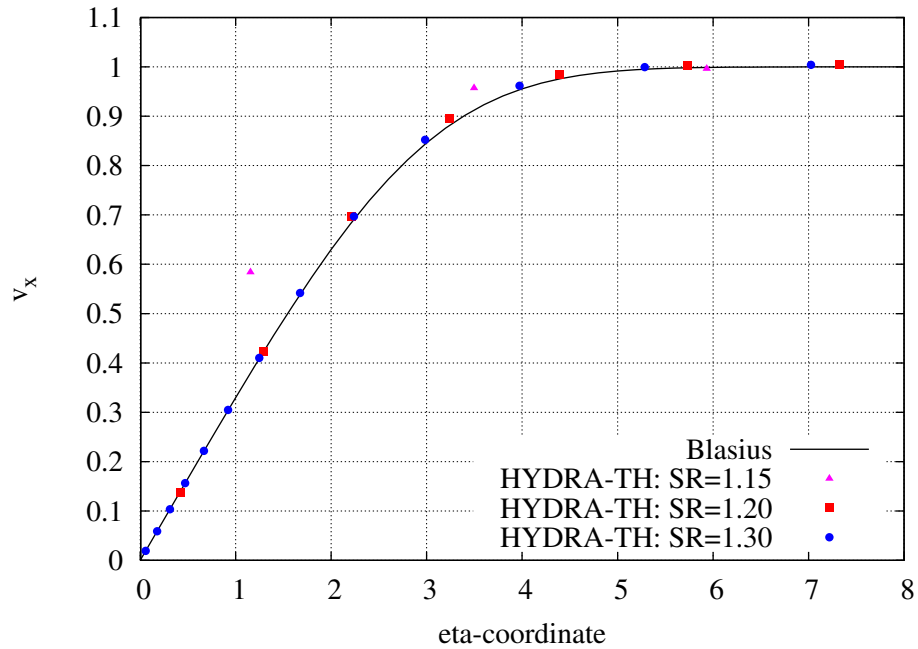

(a)

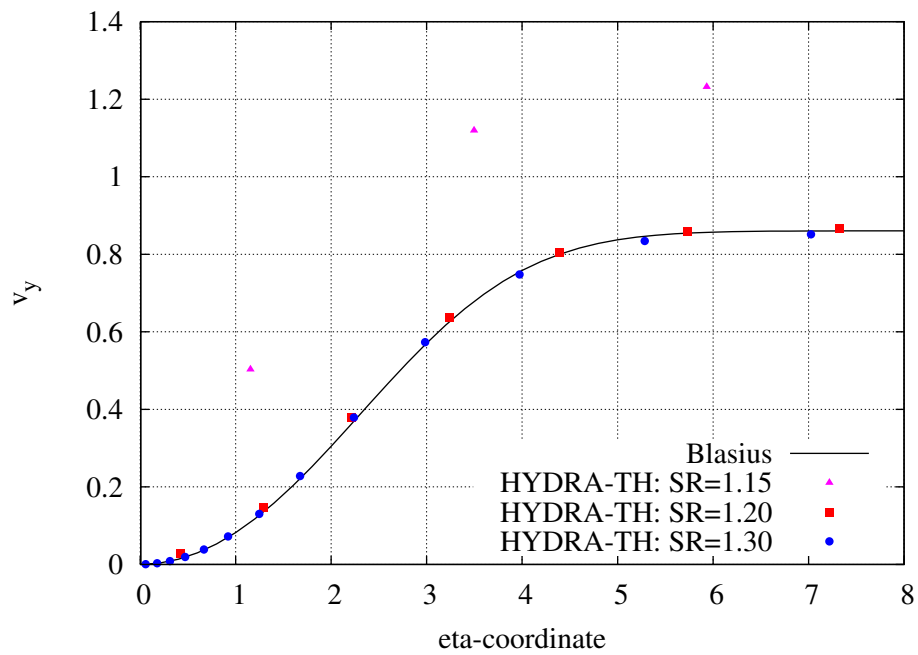

(b)

Figure 2.22: Plot of the (a) v_x and (b) v_y profiles obtained on the $(25 + 50) \times 30 \times 1$ hexahedral grids compared with the analytical solutions along the cells cut through by plane of $x = 0.10$ in the boundary layer region

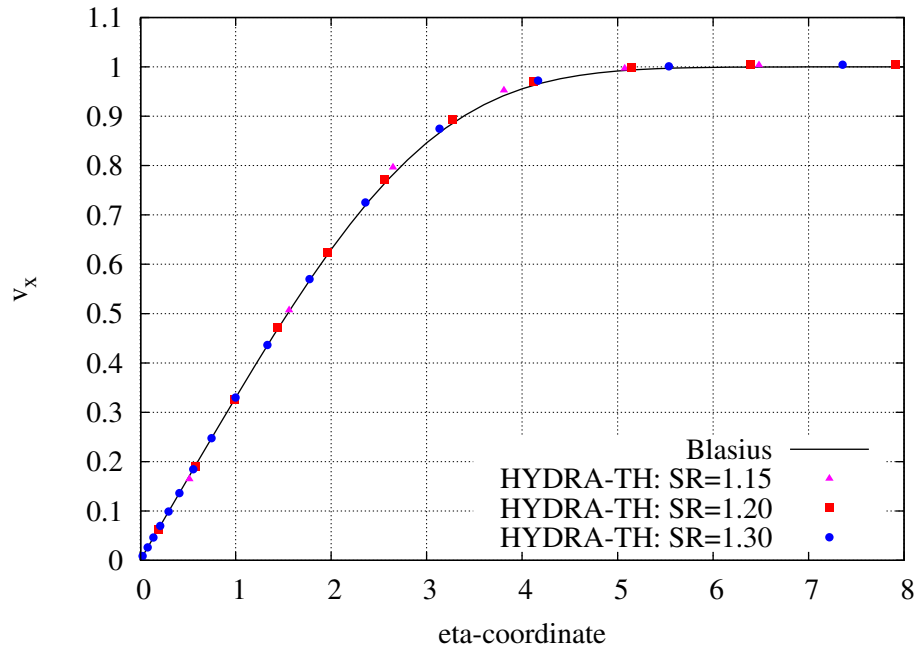

(a)

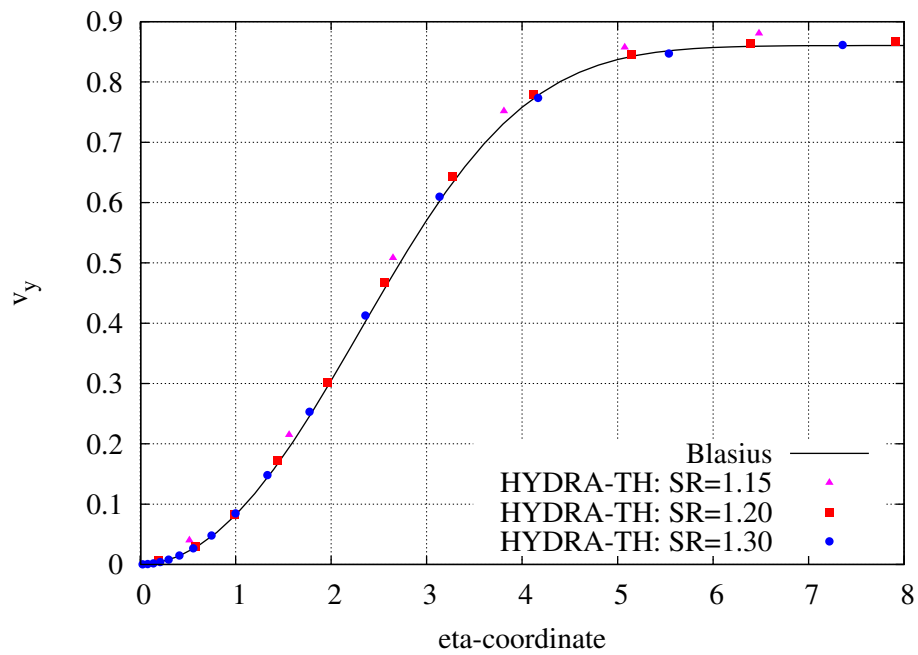

(b)

Figure 2.23: Plot of the (a) v_x and (b) v_y profiles obtained on the $(25 + 50) \times 30 \times 1$ hexahedral grids compared with the analytical solutions along the cells cut through by plane of $x = 0.50$ in the boundary layer region

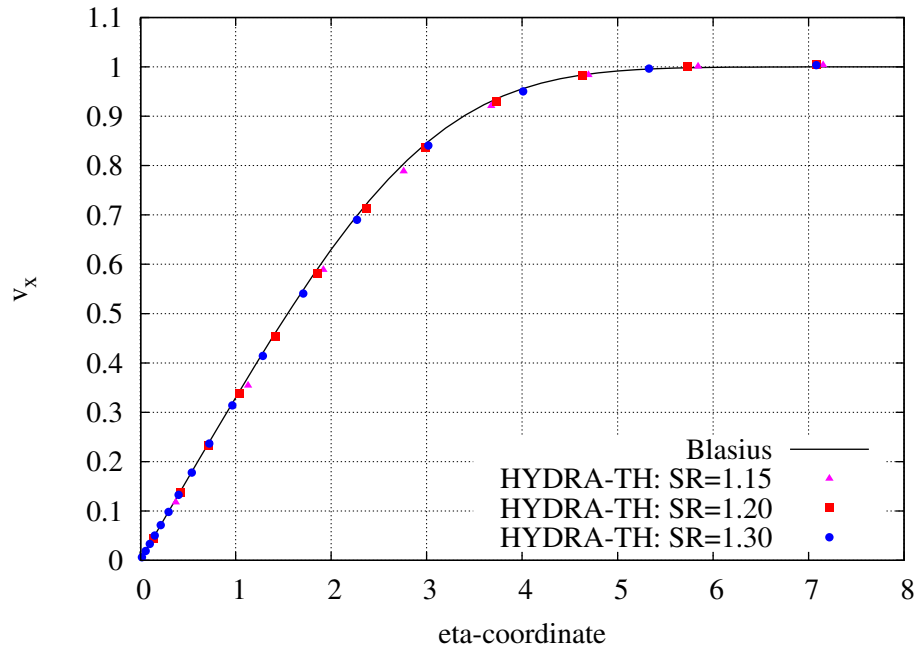

(a)

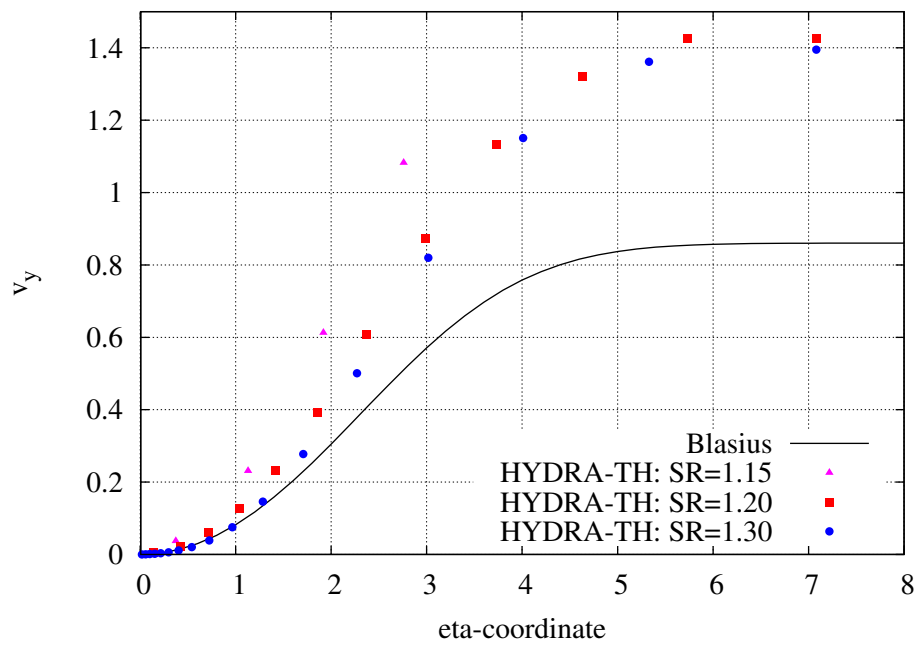

(b)

Figure 2.24: Plot of the (a) v_x and (b) v_y profiles obtained on the $(25 + 50) \times 30 \times 1$ hexahedral grids compared with the analytical solutions along the cells cut through by plane of $x = 0.99$ in the boundary layer region

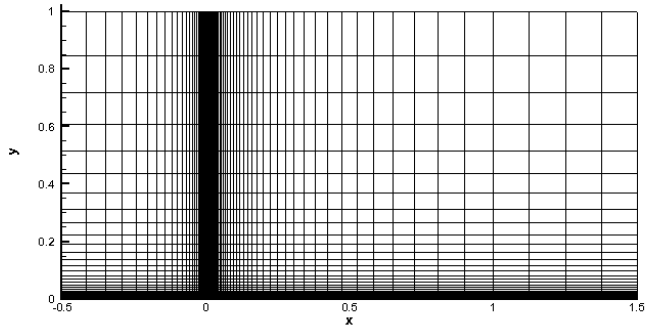

(a)

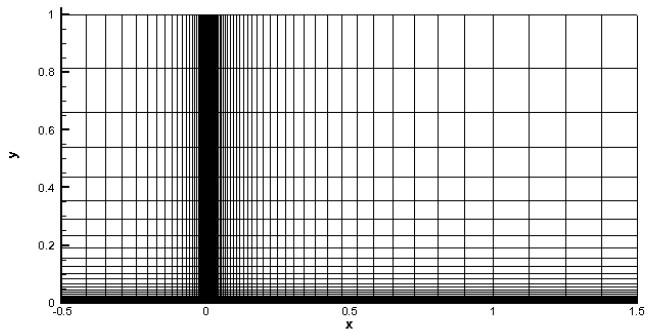

(b)

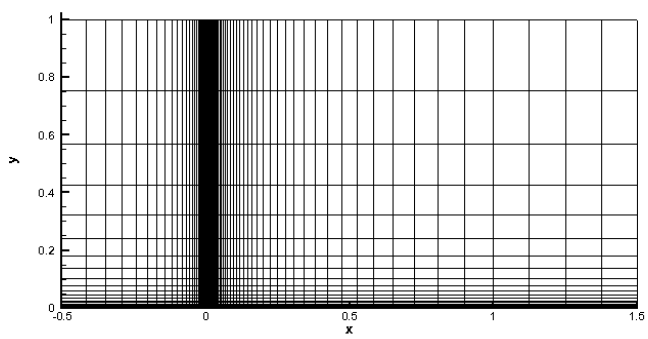

(c)

Figure 2.25: Plot of the $(25 + 50 + 4) \times 30 \times 1$ hexahedral grids for steady flow past a flat plate at $Re = 100,000$: (a) $SR = 1.15$ in y-direction; (b) $SR = 1.20$ in y-direction; (c) $SR = 1.30$ in y-direction

CASL-U-2013-0324-000-b

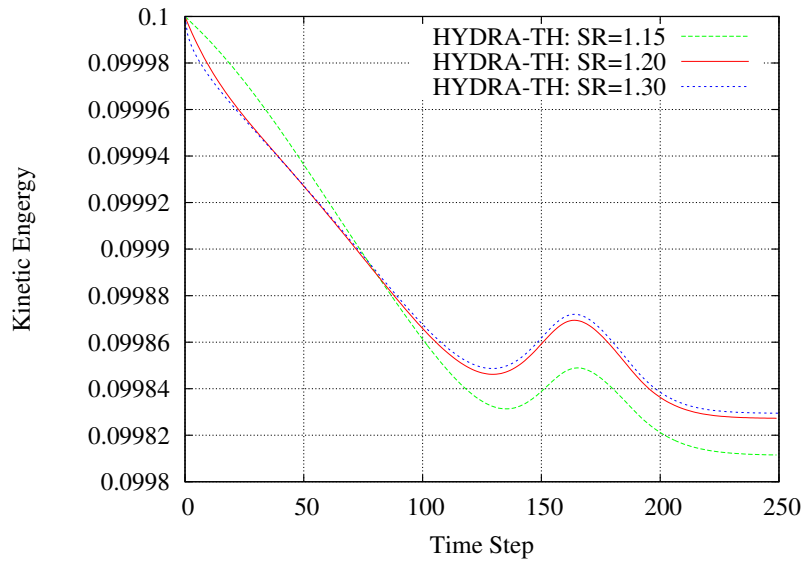

Figure 2.26: Time history plots for kinetic energy obtained on the $(25+50+4)\times 30\times 1$ hexahedral grids

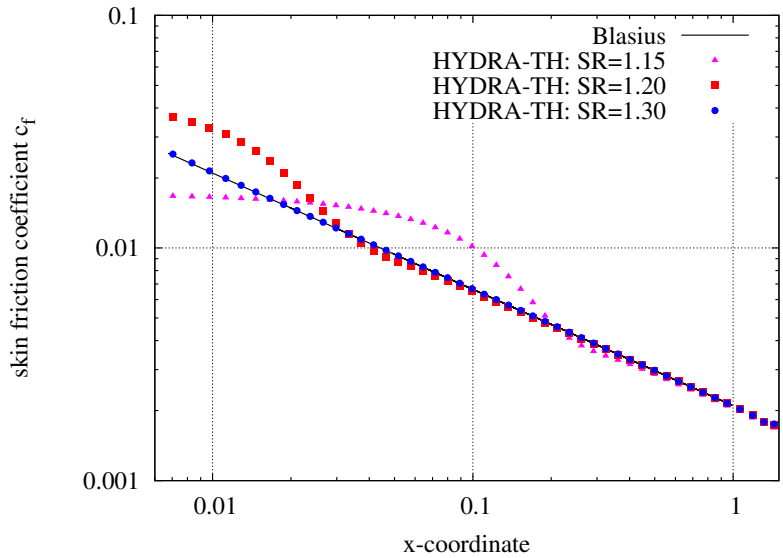

Figure 2.27: Logarithmic plot of the computed skin friction coefficient distribution obtained on the $(25+50+4)\times 30\times 1$ hexahedral grids compared with the analytical solution along the flat plate $x=[0,1.5]$

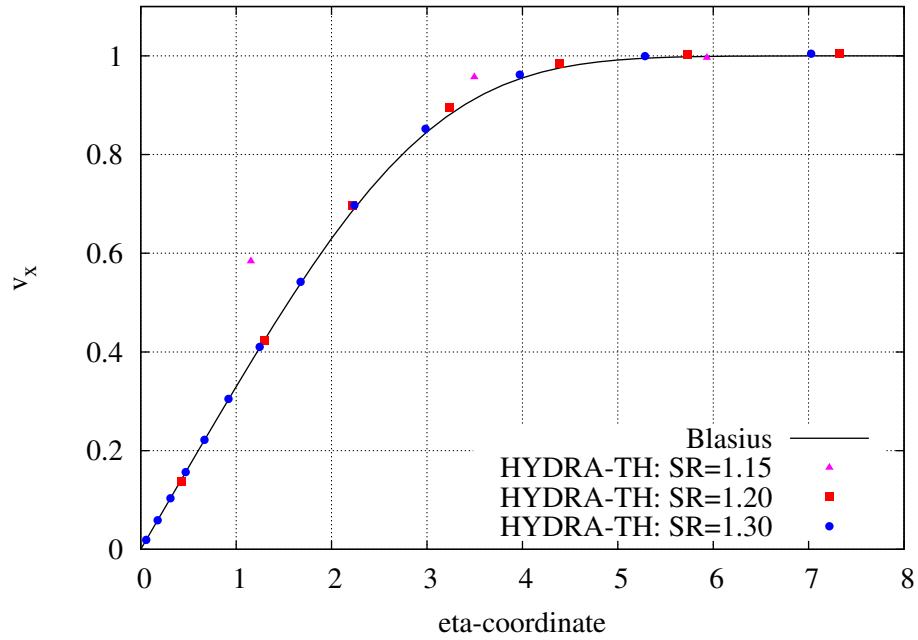

(a)

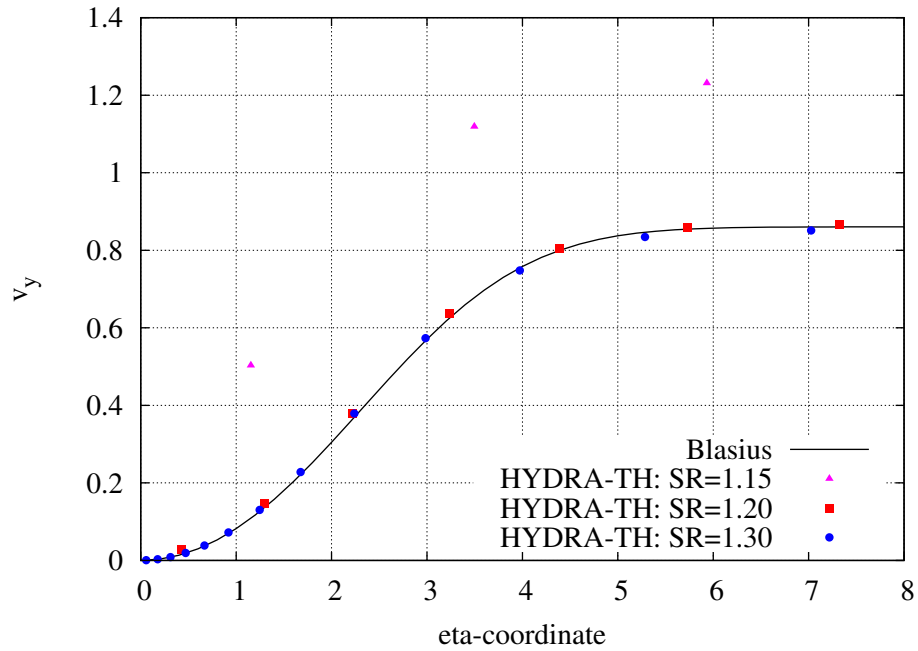

(b)

Figure 2.28: Plot of the (a) v_x and (b) v_y profiles obtained on the $(25 + 50 + 4) \times 30 \times 1$ hexahedral grids compared with the analytical solutions along the cells cut through by plane of $x = 0.10$ in the boundary layer region

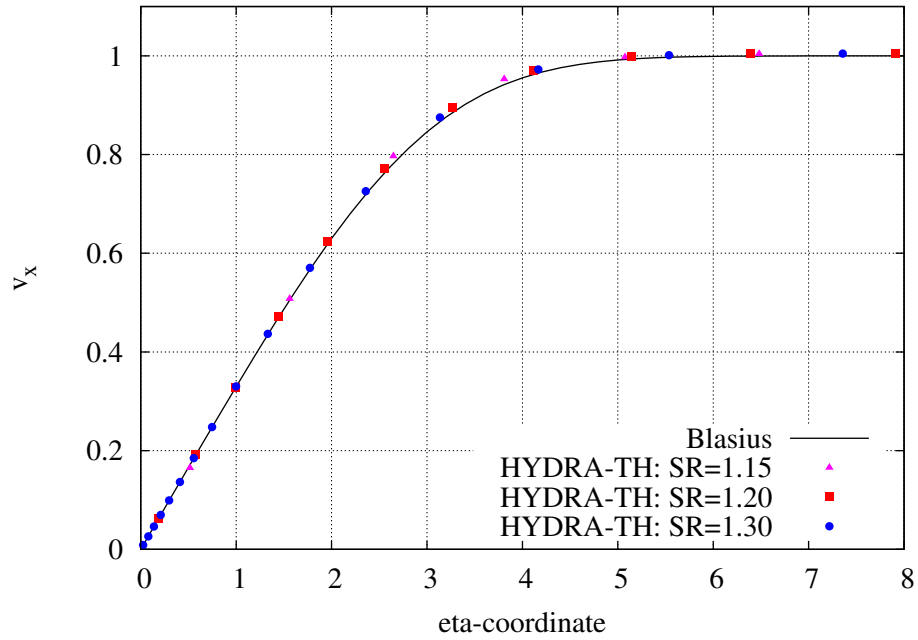

(a)

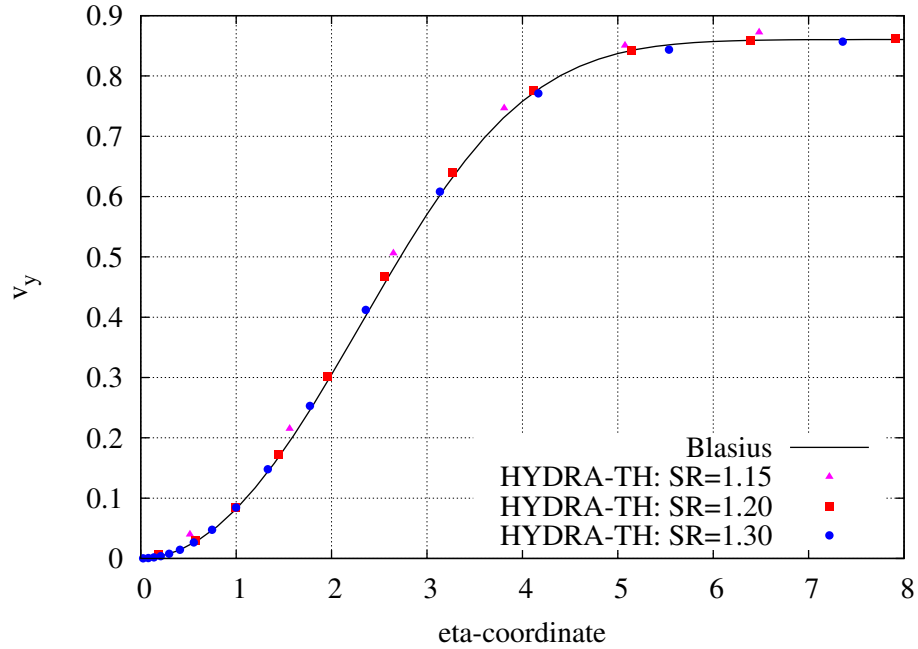

(b)

Figure 2.29: Plot of the (a) v_x and (b) v_y profiles obtained on the $(25 + 50 + 4) \times 30 \times 1$ hexahedral grids compared with the analytical solutions along the cells cut through by plane of $x = 0.50$ in the boundary layer region

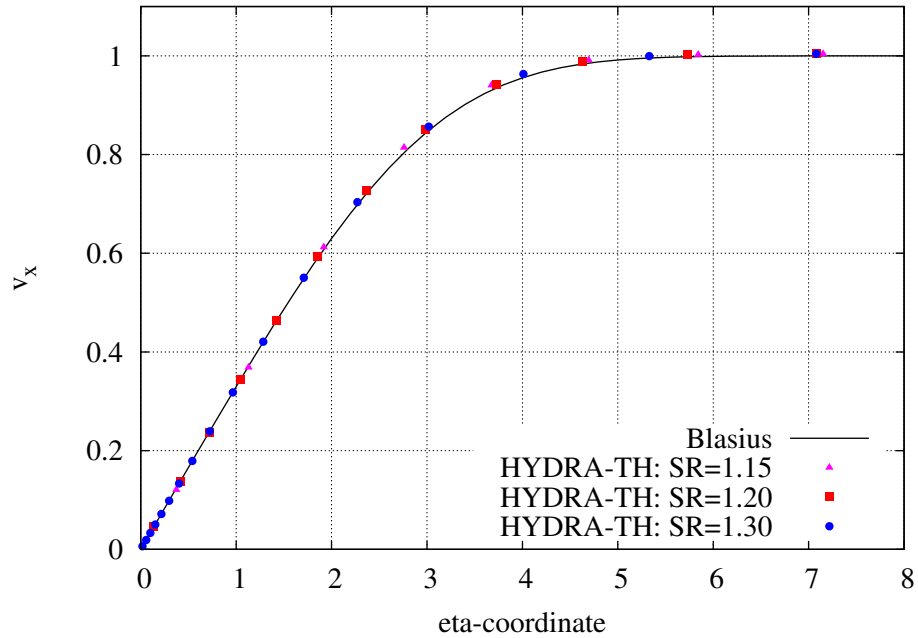

(a)

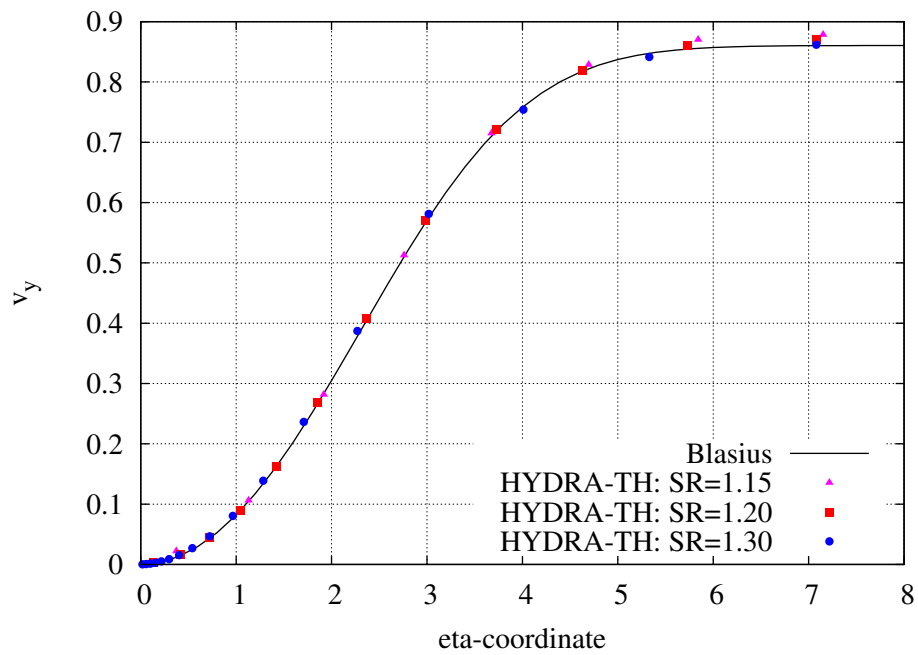

(b)

Figure 2.30: Plot of the (a) v_x and (b) v_y profiles obtained on the $(25 + 50 + 4) \times 30 \times 1$ hexahedral grids compared with the analytical solutions along the cells cut through by plane of $x = 0.99$ in the boundary layer region

2.5 Turbulent Channel Flow

2.5.1 Problem Description

This problem is focused on the use of RANS models for the simulation of turbulent channel flow at a friction Reynolds number of $Re_\tau = 590$. The Spalart-Allmaras model and RNG $k - \varepsilon$ model are used for turbulence modeling.

2.5.2 Problem Setup

This 2-D turbulent flow problem considered here consists of a 2-D channel with a 20 : 1 aspect ratio and $Re = 10^4$. The problem is defined in a non-dimensional form, with $\partial p/\partial x = -2.785 \times 10^{-2}$. This choice of Reynolds number and pressure gradient results in an approximate posteriori friction Reynolds number of $Re_\tau = 590$. In this study, a computation is conducted for each of the turbulence models on a series of three successively refined hexahedral grids, as described in Table 2.7 and Table 2.8, respectively. The channel dimensions are 20 units in the x direction, 1 unit in the y direction, and 0.05 unit in the z direction, as shown in Figure 2.31. The grid is uniform in the streamwise x directions.

Table 2.7: Grids used for simulation of a turbulent channel flow, $Re_\tau = 590$, Spalart-Allmaras model.

Grid size	y-coordinate of cell center for first layer	y^+ of cell center for first layer
$50 \times 101 \times 1$	1.162×10^{-3}	1.371
$50 \times 201 \times 1$	9.343×10^{-5}	0.110
$50 \times 401 \times 1$	2.823×10^{-4}	0.333

Table 2.8: Grids used for simulation of a turbulent channel flow, $Re_\tau = 590$, RNG k-ε model.

Grid size	y-coordinate of cell center for first layer	y^+ of cell center for first layer
$50 \times 41 \times 1$	1.220×10^{-2}	14.390
$50 \times 81 \times 1$	6.173×10^{-3}	7.284
$50 \times 161 \times 1$	3.106×10^{-3}	3.665

In order to represent the constant pressure gradient, an inflow pressure boundary condition of $p = 0.557$ is prescribed with $p = 0$ at the outflow. At the inflow, $v_y = 0$ and $v_z = 0$. No-slip/no-penetration conditions $\mathbf{v} = (0, 0, 0)$ are prescribed along the top and bottom channel walls. The so-called "natural" velocity boundary conditions are applied at the outflow boundary. Slip conditions ($v_x = 0$ and $v_y = 0$) are prescribed on the front and back surfaces. The fluid is initially at rest ($\mathbf{v} = \mathbf{0}$). This choice of boundary conditions permits the inlet velocity to float and adapt to the pressure gradient which minimize entrance effects.

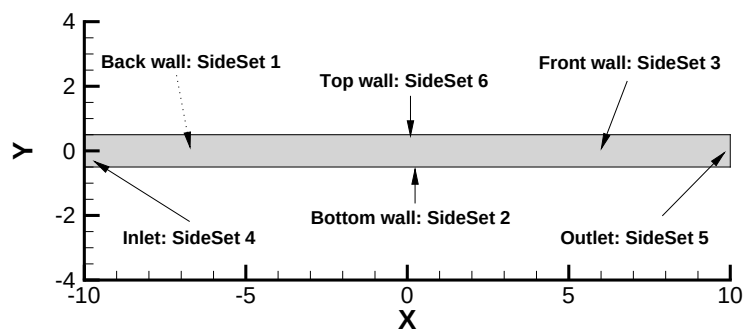

Figure 2.31: The bounded domain for simulation of a turbulent channel flow.

2.5.3 Results

A simulation time of $t = 500$ units was used for all computations in order to ensure that steady-state conditions have been achieved. Figure 2.33 and 2.34 show the time history of global kinetic energy and affirm that steady conditions are achieved at $t = 500$.

Figures 2.35 – 2.40 show the mean streamwise velocity v_x and the turbulent eddy viscosity ν_t for the Spalart-Allmaras and the RNG $k - \varepsilon$ models respectively. Figures 2.40) and 2.42 show the turbulent kinetic energy k and turbulent kinetic energy dissipation rate ε for the $k - \varepsilon$ model. In each of these figures, the data is extracted at $x = 5$ (3/4 of the channel length), and plotted versus the normal distance from the bottom wall to half width of the channel.

The normalized velocity profiles are plotted with the direct numerical simulation (DNS) results by Moser et al. [14] in Figure 2.37 and 2.38. DNS is a numerical technique where all scales of a turbulent flow are resolved [13]. The non-dimensional velocity v_x^+ is defined as $v_x^+ = v_x/u_\tau$, where u_τ is the friction velocity. u_τ is computed from the equation for friction Reynolds number $Re_\tau = u_\tau \delta/\nu$, where $\delta = 1/2$ is the half width of channel and $\nu = 10^{-4}$ is prescribed. The non-dimensional wall distance y^+ is defined as $y^+ = u_* y/\nu$, where u_* is the friction velocity at the nearest wall (equal to the u_τ in this context), and y is the distance to the nearest wall.

It is observed that the profiles obtained from the 50×201 and 50×401 grids almost coincide in Figure 2.35, 2.37 and 2.39. Moreover, both the unscaled and scaled velocity profiles by Spalart-Allmaras model match the DNS results quite well.

In Figure 2.38, it is observed that the scaled velocity profiles by RNG k-ε model show the convergence of the solution and can match the DNS profile in the log-layer region, but they do not

tend to approach the DNS profile once in the sublayer, due to the limitations of using wall functions which is explained in Hydra-TH Theory Manual [3], section 12.4.

2.5.4 Control Files

The control files for this problem are `channel_sa.cntl` for the Spalart-Allmaras model and `channel_ke.cntl` for the $k - \varepsilon$ model. The `channel_sa.cntl` file is listed in Figure 2.32. The control files may be found in the `2D/channel` directory.

2.5.5 Mesh Files

The mesh files may be found in the `2D/channel` directory, and are `channel_sa_101.exo`, `channel_sa_201.exo`, `channel_sa_401.exo` for the Spalart-Allmaras model, and `channel_ke_81.exo`, `channel_ke_161.exo`, `channel_ke_321.exo` for the $k - \varepsilon$ model.

```
title
Re_tau = 590 channel flow

cc_navierstokes

  nsteps 10000
  deltat 1.0e-4
  term    500.00

  time_integration
    type    fixed_cfl
    CFLinit 1.0
    CFLmax  20.0
    dtmax   0.2
    dtscale 1.075
    thetaa  1.0
    thetak  1.0
    thetaf  1.0
  end

  load_balance
    method rcb
  end

  # Output options
  pltype exodusii
  filetype serial
  plti   100
  ttyi   25
  dump   2000

  # Turbulence model
  tmodel spalart_allmaras

  # Material model setup &
  # assignment to sets
  material
    id  1
    rho 1.0
    mu  1.0e-4
  end

  materialset
    id 10
    material 1
    block 1
  end

  plotvar
    elem density
    elem vel
    elem procid
    elem div
    elem turbnu
    node vel
    node lambda
    node pressure
    node dist
    node vorticity
    node helicity
    side 2 yplus
    side 2 wallshear
    side 6 yplus
    side 6 wallshear
  end

  histvar
    side 4 avgvel
    side 5 avgvel
  end

  # Simple IC's
  initial
    velx   0.0
    vely   0.0
    velz   0.0
    turbnu 3.1e-4
  end

 # Sideset - meaning
  #   1     - back
  #   2     - bottom
  #   3     - front
  #   4     - inlet
  #   5     - outlet
  #   6     - top

  # Drive problem with pressure
  pressure
    # 20 units long
    sideset 4 -1 0.5570
    sideset 5 -1 0.0
  end

  distance
    sideset 2 -1 0.0 # bottom
    sideset 6 -1 0.0 # top
  end

  turbnu
    sideset 2 -1 0.0 # bottom
    sideset 6 -1 0.0 # top
  end

  velocity
    # back
    velz sideset 1 -1  0.0

    # bottom
    velx sideset 2 -1  0.0
    vely sideset 2 -1  0.0
    velz sideset 2 -1  0.0

    # front
    velz sideset 3 -1  0.0

    #Inlet
    vely sideset 4 -1  0.0
    velz sideset 4 -1  0.0

    # top
    velx sideset 6 -1  0.0
    vely sideset 6 -1  0.0
    velz sideset 6 -1  0.0
  end

  ppesolver
    type  AMG
    amgpc hypre
    itmax 50
    itchk 1
    strong_threshold 0.90
    diagnostics off
    convergence off
    eps   1.0e-5
  end

  momentumsolver
    type  ILUFGMRES
    itmax 75
    itchk 2
    restart 15
    diagnostics off
    convergence off
    eps   1.0e-5
  end

  transportsolver
    type  ILUFGMRES
    itmax 75
    itchk 2
    restart 15
    diagnostics off
    convergence off
    eps   1.0e-5
  end

end

exit
```

Figure 2.32: Control file for turbulent channel flow using the Spalart-Allmaras model.

CASL-U-2013-0324-000-b

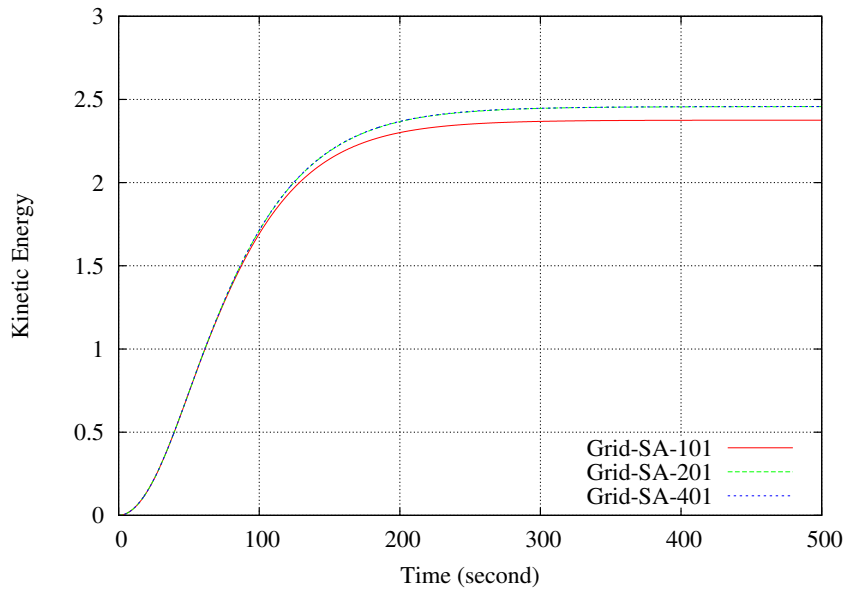

Figure 2.33: Time history of global kinetic energy for simulation of a turbulent channel flow, $Re_\tau = 590$, Spalart-Allmaras model.

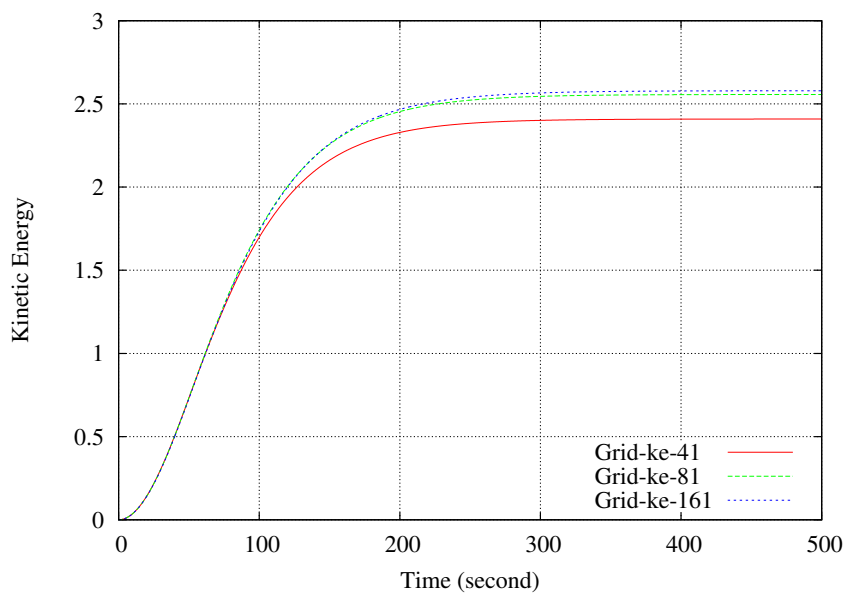

Figure 2.34: Time history of global kinetic energy for simulation of a turbulent channel flow, $Re_\tau = 590$, RNG k-ε model.

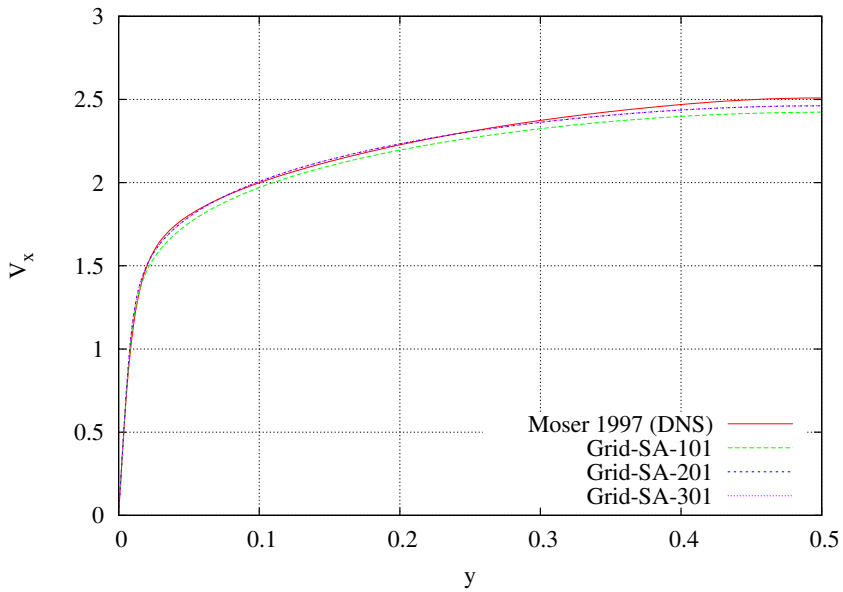

Figure 2.35: v_x versus normal distance from bottom wall for simulation of a turbulent channel flow, $Re_\tau = 590$, Spalart-Allmaras model.

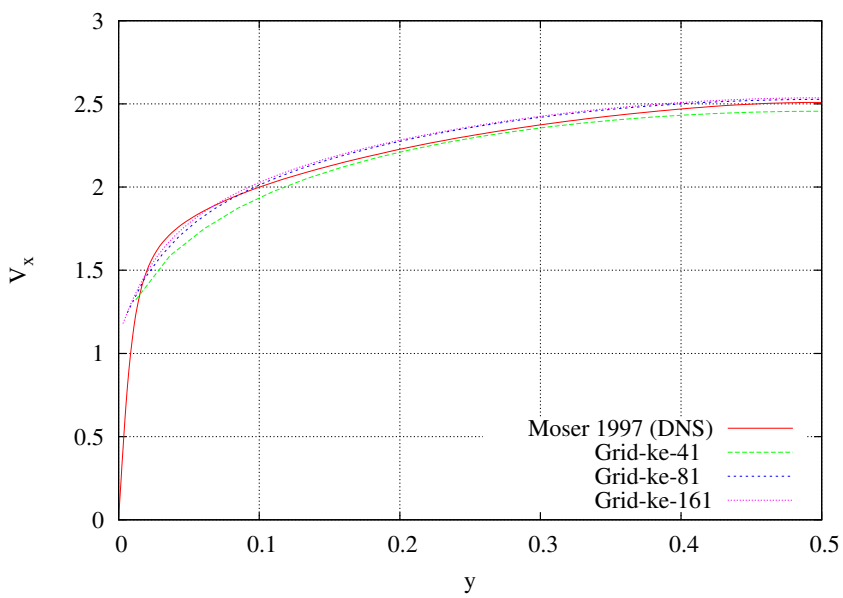

Figure 2.36: v_x versus normal distance from bottom wall for simulation of a turbulent channel flow, $Re_\tau = 590$, RNG k-ε model.

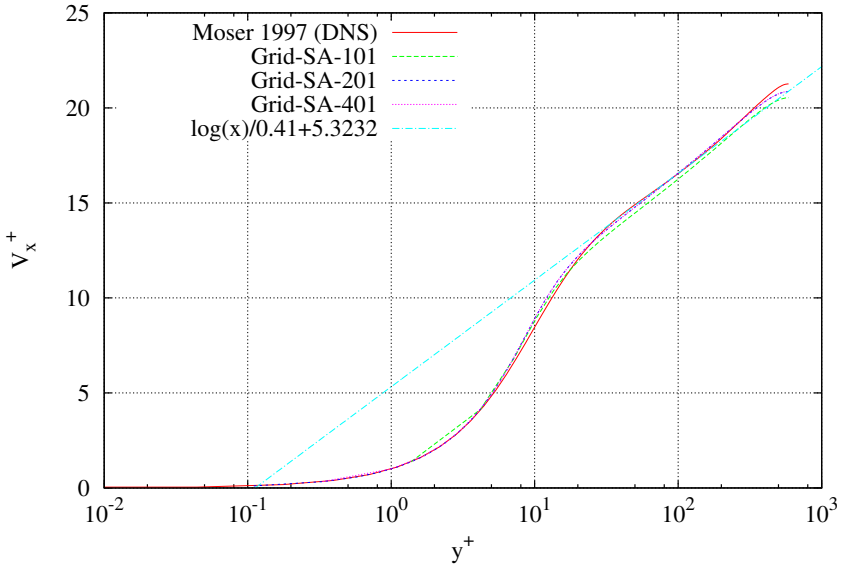

Figure 2.37: v_x^+ versus y^+ from bottom wall for simulation of a turbulent channel flow, $Re_\tau = 590$, Spalart-Allmaras model.

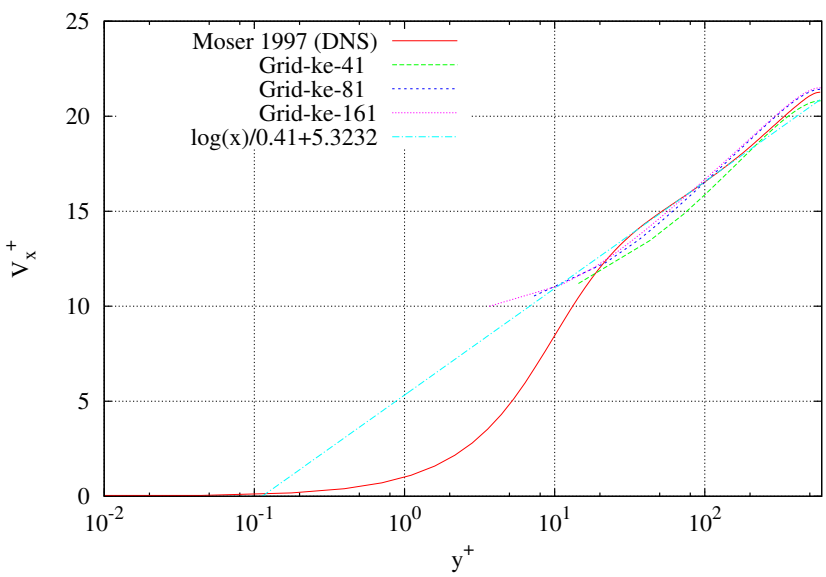

Figure 2.38: v_x^+ versus y^+ from bottom wall for simulation of a turbulent channel flow, $Re_\tau = 590$, RNG k-ε model.

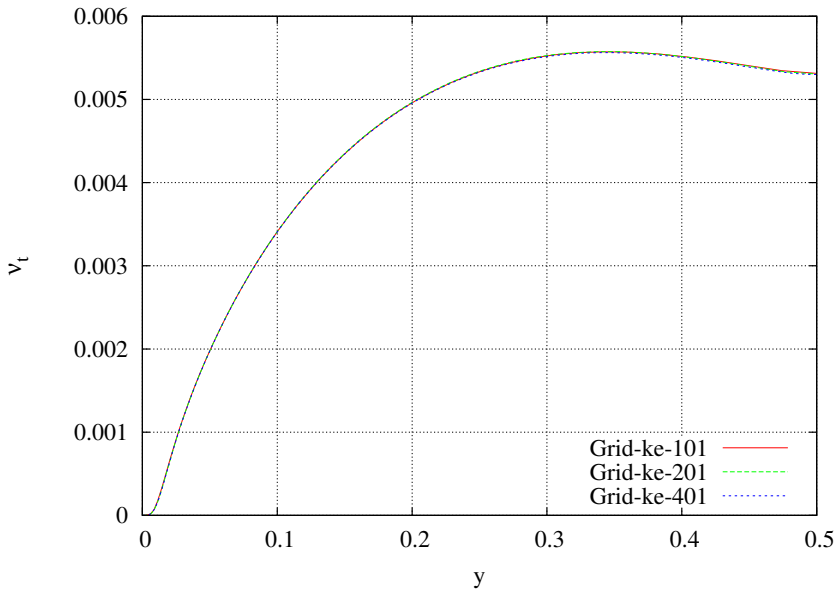

Figure 2.39: Turbulent eddy viscosity versus normal distance from bottom wall for simulation of a turbulent channel flow, $Re_\tau = 590$, Spalart-Allmaras model.

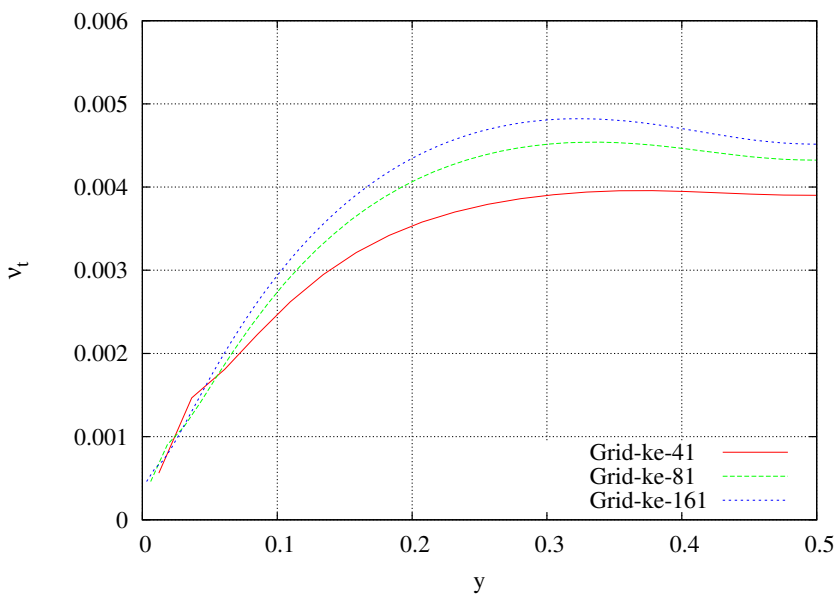

Figure 2.40: Turbulent eddy viscosity versus normal distance from bottom wall for simulation of a turbulent channel flow, $Re_\tau = 590$, RNG k-ε model.

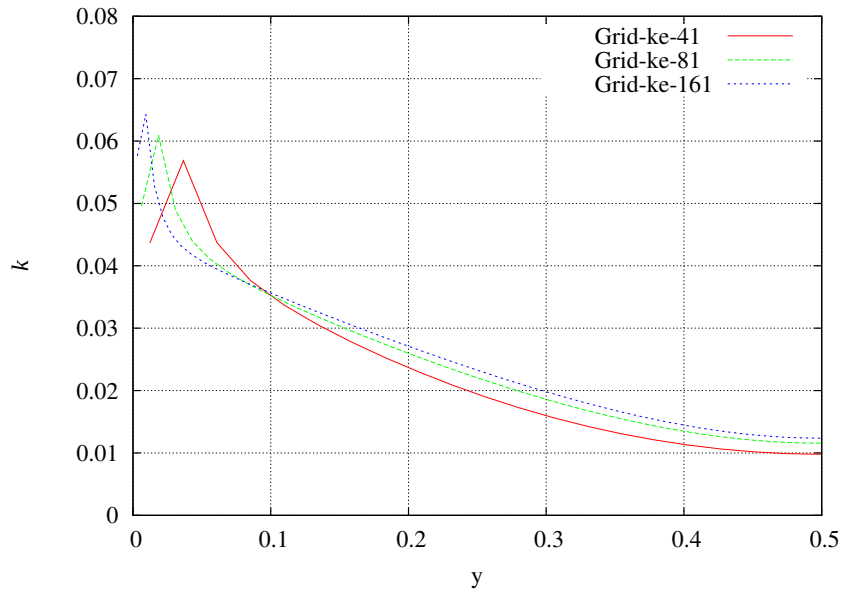

Figure 2.41: Turbulent kinetic energy versus normal distance from bottom wall for simulation of a turbulent channel flow, $Re_\tau = 590$, RNG k-ε model.

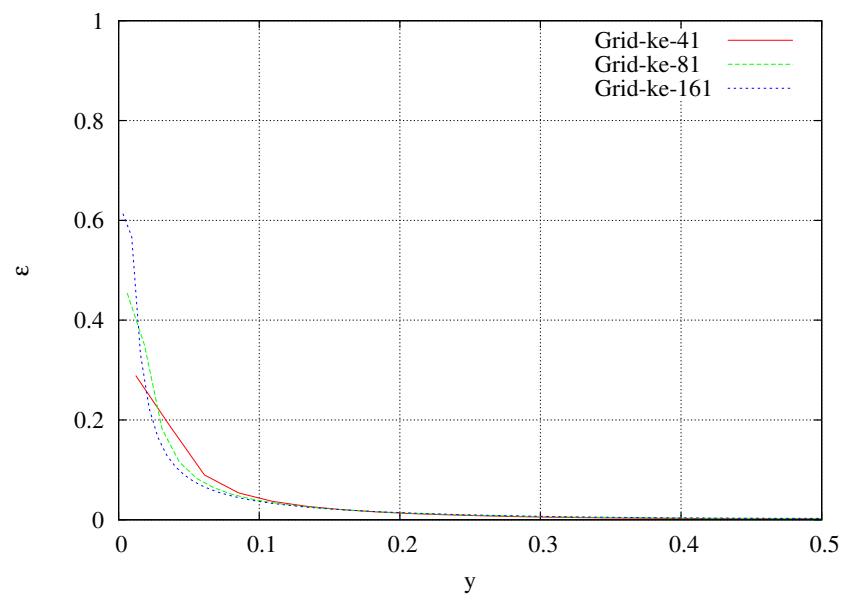

Figure 2.42: Turbulent kinetic energy dissipation rate versus normal distance from bottom wall for simulation of a turbulent channel flow, $Re_\tau = 590$, RNG k-ε model.

Chapter 3

Incompressible Navier-Stokes 3D Test Problems

3.1 Large-Eddy Simulation of a Lid-Driven Cavity Flow

3.1.1 Problem Description

This problem focuses on the large-eddy simulation (LES) of a lid-driven cavity flow at a Reynolds number of $Re = 10,000$. A grid refinement study is performed using Hydra-TH with the three turbulence models, implicit large-eddy simulation (ILES), wall-adapted large eddy (WALE) subgrid-scale model and the Smagorinsky subgrid-scale model. Once the time history of the kinetic energy reaches a statically stationary state, the mean velocity vector and Reynolds stress tensor are compared to experimental data published by Prasad and Koseff [15].

3.1.2 Problem Setup

Computations are conducted for each of the turbulence models on a series of three successively refined hexahedral grids, as shown in Figs. 3.2 and 3.3, for which the numbers of total cells are $32 \times 32 \times 16$ (coarse), $64 \times 64 \times 32$ (medium), and $128 \times 128 \times 64$ (fine). The cavity dimensions are 1 unit in the x and y directions, and 0.5 unit in the z direction. The grid is non-uniform in the streamwise x and vertical y directions, but is uniform in the span-wise z direction. Grid points are clustered near the walls in the x and y directions. The grid spacing is geometrically stretched away from the wall, where the minimum value is 5.0×10^{-3} for the coarse and medium grids, and 5.0×10^{-4} for the fine grid. On the bottom and side walls, no-slip/no-penetration boundary conditions are prescribed. Along the top "lid", a no-penetration boundary condition along with a unit lid velocity $u_b = 1$ are prescribed. The initial condition is that the velocity field is at rest with no random perturbations.

3.1.3 Results

All the tests in this experiment are run for approximately 500 time units with 20 time planes containing average statistics being written between for $100 \leq t \leq 500$ time unit. Figures. 3.4, 3.5 and 3.6 show the time histories of kinetic energy for each turbulence model. For $t > 100$, the kinetic

energy plots indicate that the flow computed with each turbulence model achieves a statistically stationary state.

The cell-centered solution of the mean velocity and Reynolds stress tensor is extracted and plotted along the center-lines on the span-wise mid-plane for direct comparison with the experimental data published by Prasad and Koseff [15]. This data is shown in Figures 3.7 - 3.9 for the ILES model, Figures 3.10 - 3.12 for the WALE model, and Figures 3.13 - 3.15 for the Smagorinsky model.

The mean $x-$ velocity $\langle u \rangle$ distribution is plotted along the vertical centerline, and the mean $y-$ velocity $\langle v \rangle$ distribution is plotted along the horizontal centerline in Figures 3.7, 3.10 and 3.13. Improvement of the mean velocities with increasing mesh resolution is clearly observed from the coarse grid to the medium grid for all of the three models. The mean velocities change only slightly when going from the medium grid to the fine grid for these models and agree quite well with the experimental data.

The scaled $\langle u'u' \rangle$ distribution is plotted along the vertical centerline, and the scaled $\langle v'v' \rangle$ distribution is plotted along the horizontal centerline as shown in Figures 3.8, 3.11 and 3.14. The scaled $\langle u'v' \rangle$ distribution is plotted along the vertical and horizontal center lines as shown in Figures 3.9, 3.12 and 3.15. The results indicate that the $\langle u'u' \rangle$ and $\langle u'v' \rangle$ profiles are significantly improved from the coarse grid to the medium grid. Also, a distinguished improvement of the $\langle u'u' \rangle$ and $\langle u'v' \rangle$ profiles can be seen from the medium grid to the fine grid in comparison to the experimental data. Further, comparison between the results obtained from these three models indicates that the performance of the ILES and WALE models is comparable, and that these models deliver far better results than Smagorinsky model in this test case.

3.1.4 Control Files

The control file for the ILES, WALE and Smagorinsky models are `ldc_Re1e4_iles.cntl`, `ldc_Re1e4_wale.cntl`, and `ldc_Re1e4_ssgs.cntl`, respectively. A representative control file for the ILES turbulence model is shown in Figure 3.1.5. The control files may be found in the `3D/ldc_grid_study` directory

3.1.5 Mesh Files

The mesh files are `ldc_Re1e4_coarse.exo`, `ldc_Re1e4_medium.exo`, and `ldc_Re1e4_fine.exo`. These files may be found in the `3D/ldc_grid_study` directory.

```
title
3-D Lid-Driven Cavity Re=10000

cc_navierstokes

  nsteps 100000
  deltat 0.01
  term   500.0

  time_integration
    type    fixed_cfl
    CFLinit 1.0
    CFLmax  10.0
    dtmax   0.2
    dtscale 1.025
    thetaa  1.0
    thetak  1.0
    thetaf  1.0
  end

  # Output options
  pltype exodusii
  filetype serial
  plti   100
  ttyi   1
  dump   0

  # Turbulence model
  #  Default is ILES, uncomment
  #  the appropriate line to
  #  change the turbulence
  #  model.
  #tmodel smagorinsky
  #tmodel wale

  # Material model setup and
  # assignment to sets
  material
    id  1
    rho 1.0
    mu  1.0e-4
  end

  materialset
    id 10
    material 1
    block 1
  end

  plotvar
    elem vel
    node vel
    node pressure
    node vorticity
  end

  statistics
    starttime   100.0
    endtime     500.0
    plotwinsize 20.0
  end

  plotstatvar
    elem <velocity>
    elem <pressure>
    elem <vorticity>
    elem tke
    elem reynoldsstress

    node <velocity>
    node <pressure>
    node <vorticity>
    node tke
    node reynoldsstress
  end

  # Simple IC's
  initial
    velx 0.0
    vely 0.0
    velz 0.0
  end

  hydrostat
    nodeset 1 -1 0.0
  end

  distance
    sideset 1 -1 0.0 # lid
    sideset 2 -1 0.0 # walls
  end

   velocity
    velx sideset 1 -1  1.0 #lid
    vely sideset 1 -1  0.0
    velz sideset 1 -1  0.0
    velx sideset 2 -1  0.0 #walls
    vely sideset 2 -1  0.0
    velz sideset 2 -1  0.0
  end

  ppesolver
    type  AMG
    itmax 250
    itchk 1
    solver cg
    smoother ICC
    coarse_size 1000
    diagnostics off
    convergence off
    eps   1.0e-5
  end

  momentumsolver
    type  ILUFGMRES
    itmax 50
    itchk 2
    restart 15
    diagnostics off
    convergence off
    eps   1.0e-5
  end

  transportsolver
    type  ILUFGMRES
    itmax 50
    itchk 2
    restart 15
    diagnostics off
    convergence off
    eps   1.0e-5
  end

end

exit
```

Figure 3.1: Control file for the lid driven cavity problem with the ILES turbulence model.

CASL-U-2013-0324-000-b

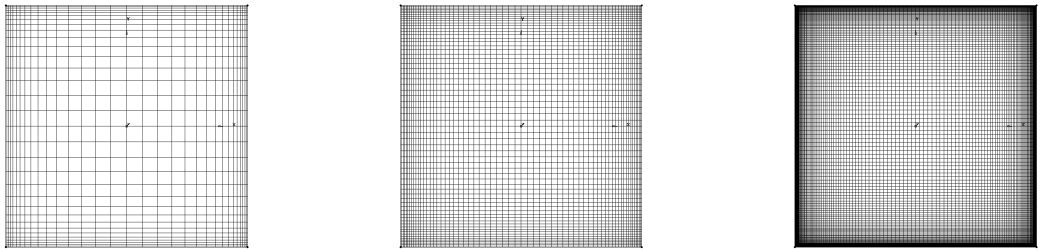

(a) (b) (c)

Figure 3.2: A series of refined grids, $32 \times 32 \times 16$, $64 \times 64 \times 32$, and $128 \times 128 \times 64$, for large-eddy simulation of a flow in lid-driven cavity at $Re = 10,000$, $x - y$ plane.

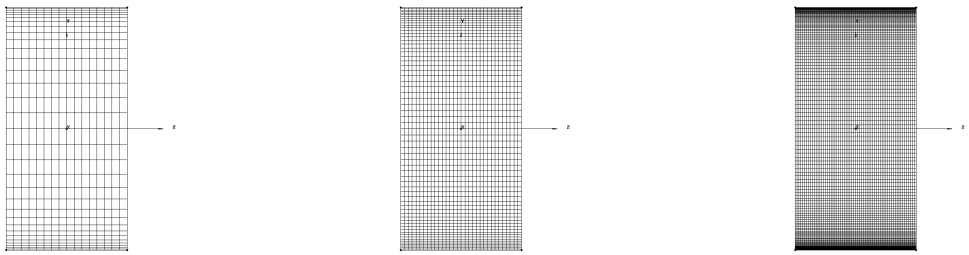

(a) (b) (c)

Figure 3.3: A series of refined grids, $32 \times 32 \times 16$, $64 \times 64 \times 32$, and $128 \times 128 \times 64$, for large-eddy simulation of a flow in lid-driven cavity at $Re = 10,000$, $z - y$ plane.

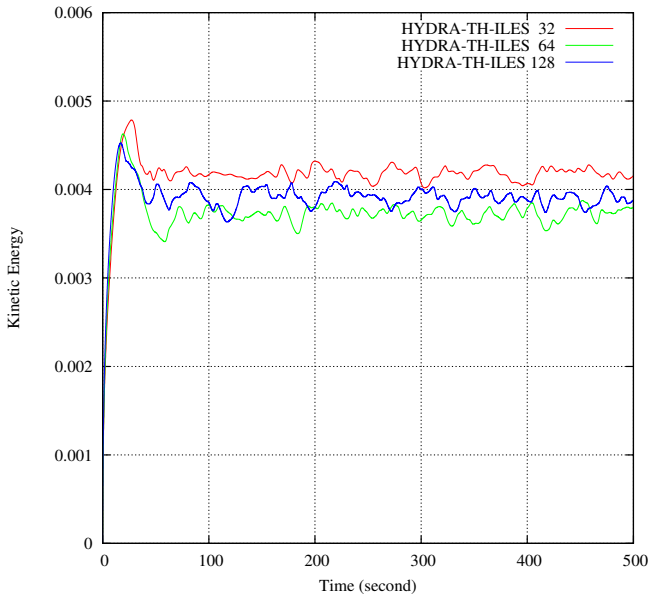

Figure 3.4: Time history of global kinetic energy for large-eddy simulation of a flow in lid-driven cavity at $Re = 10,000$, obtained on a series of refined grids, $32 \times 32 \times 16$, $64 \times 64 \times 32$, and $128 \times 128 \times 64$, using ILES model.

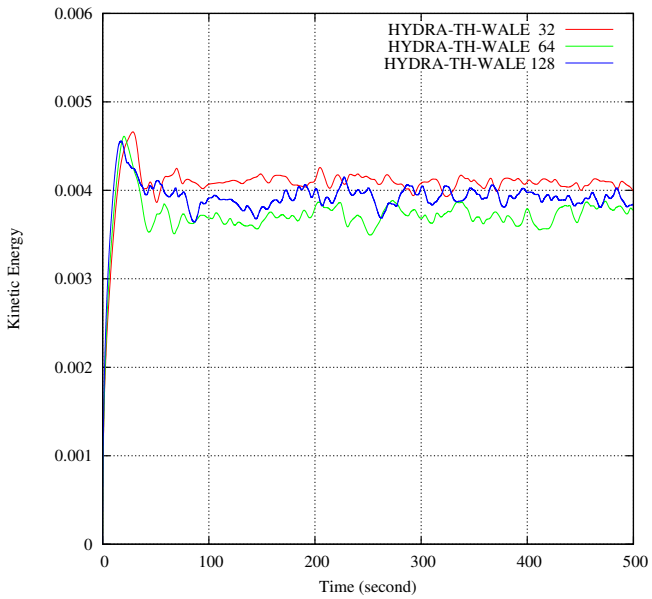

Figure 3.5: Time history of global kinetic energy for large-eddy simulation of a flow in lid-driven cavity at $Re = 10,000$, obtained on a series of refined grids, $32 \times 32 \times 16$, $64 \times 64 \times 32$, and $128 \times 128 \times 64$, using WALE model.

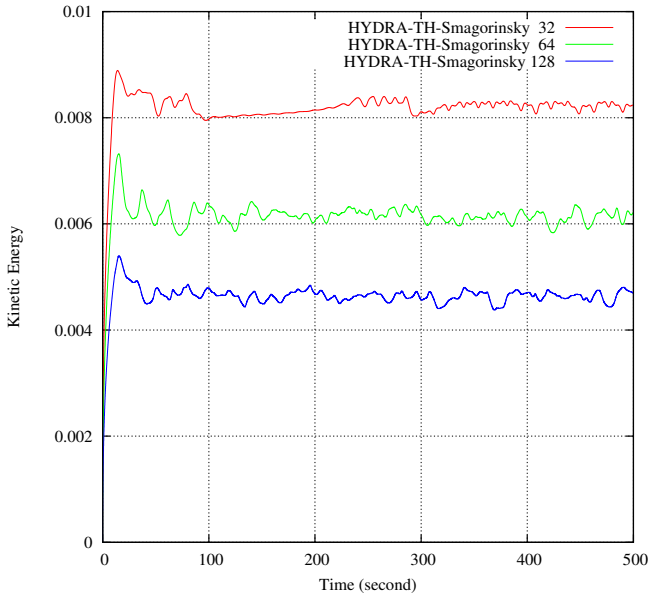

Figure 3.6: Time history of global kinetic energy for large-eddy simulation of a flow in lid-driven cavity at $Re = 10,000$, obtained on a series of refined grids, $32 \times 32 \times 16$, $64 \times 64 \times 32$, and $128 \times 128 \times 64$, using Smagorinsky model.

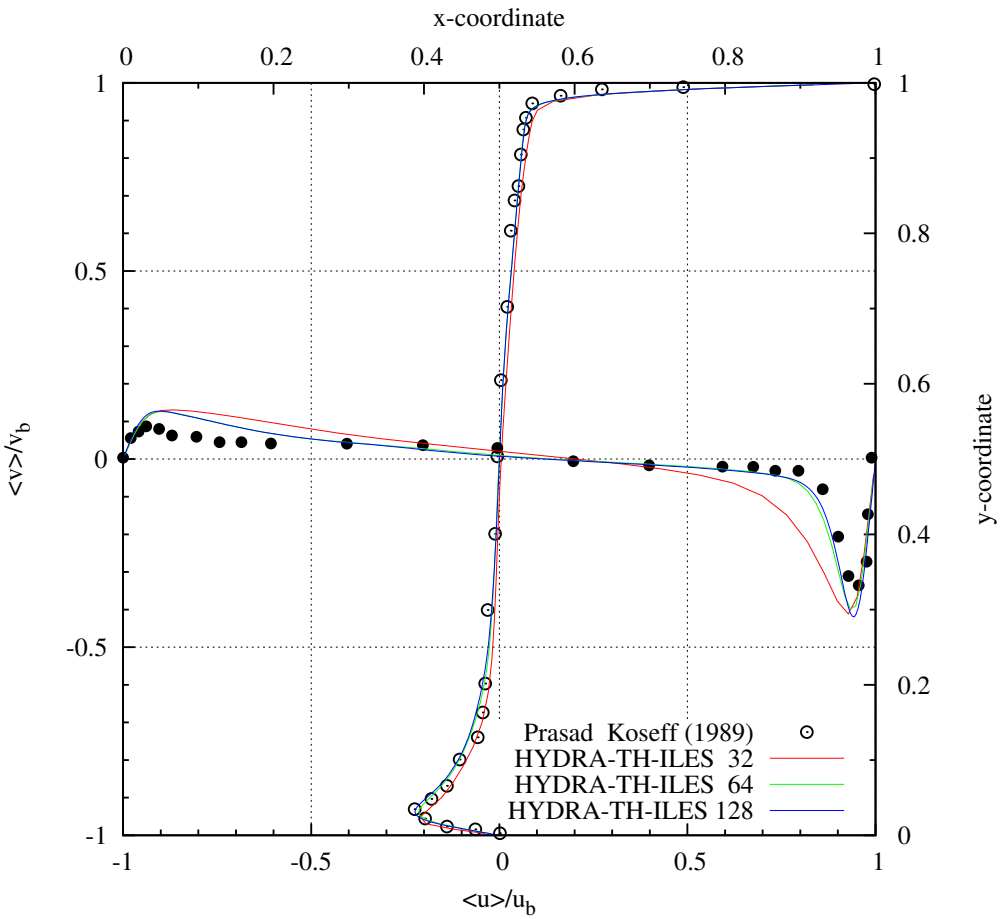

Figure 3.7: Comparisons of mean velocity components $\langle u \rangle / u_b$ and $\langle v \rangle / u_b$ in the spanwise mid-plane with experimental data for large-eddy simulation of a flow in lid-driven cavity at $Re = 10,000$, obtained on a series of refined grids, $32 \times 32 \times 16$, $64 \times 64 \times 32$, and $128 \times 128 \times 64$, using ILES model.

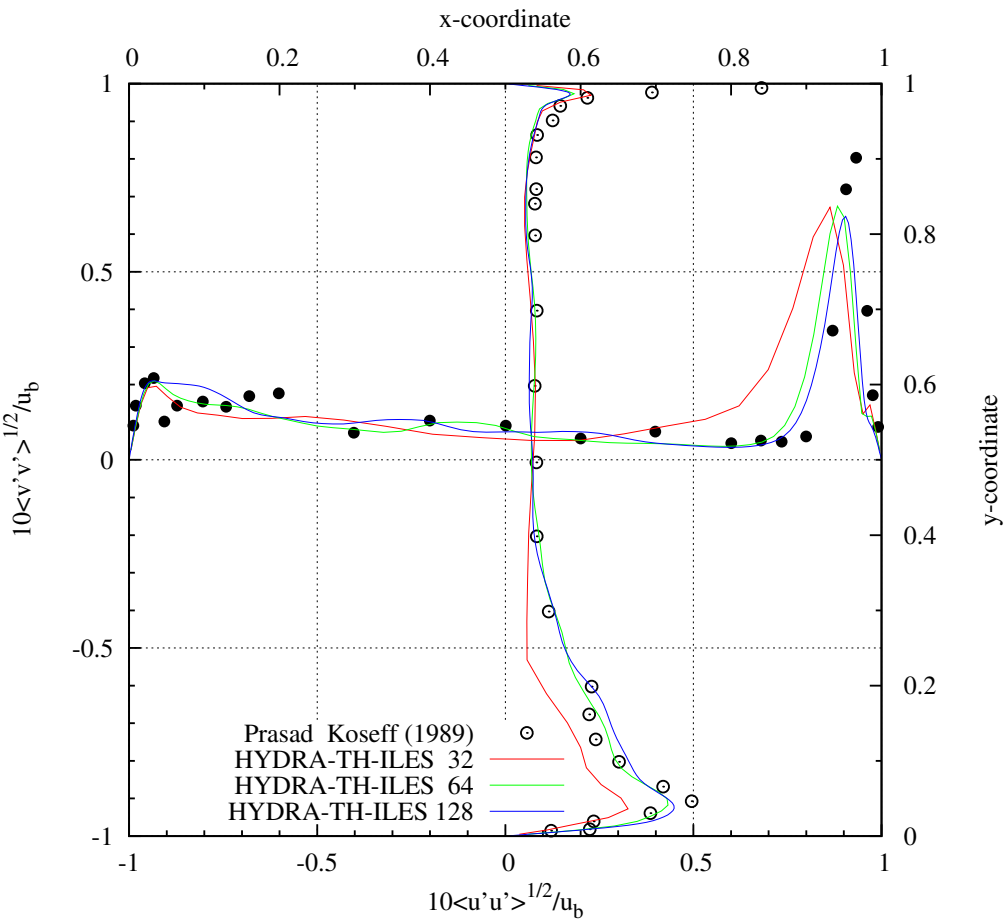

Figure 3.8: Comparisons of scaled RMS velocity components $10\sqrt{\langle u'u' \rangle}/u_b$ and $10\sqrt{\langle v'v' \rangle}/u_b$ in the spanwise mid-plane with experimental data for large-eddy simulation of a flow in lid-driven cavity at $Re = 10,000$, obtained on a series of refined grids, $32 \times 32 \times 16$, $64 \times 64 \times 32$, and $128 \times 128 \times 64$, using ILES model.

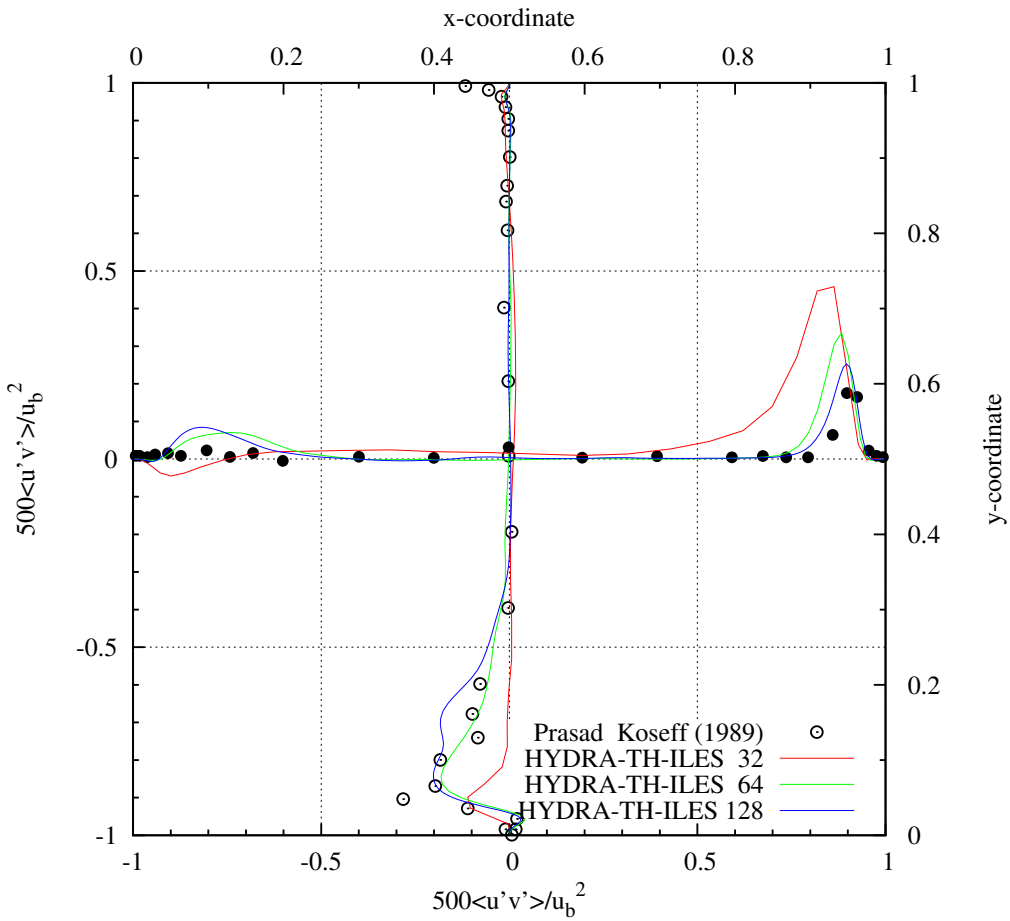

Figure 3.9: Comparisons of scaled Reynolds stress tensor components $500\langle u'v'\rangle/u_b^2$ in the spanwise mid-plane with experimental data for large-eddy simulation of a flow in lid-driven cavity at $Re = 10,000$, obtained on a series of refined grids, $32 \times 32 \times 16$, $64 \times 64 \times 32$, and $128 \times 128 \times 64$, using ILES model.

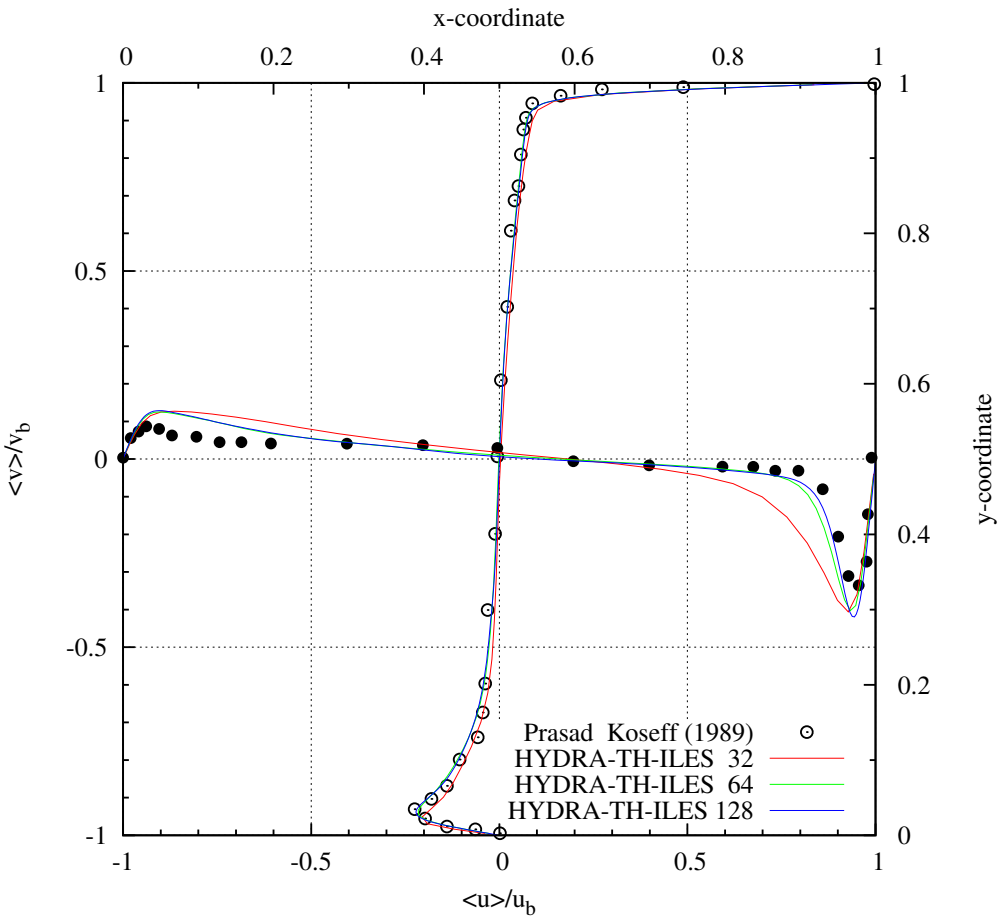

Figure 3.10: Comparisons of mean velocity components $\langle u \rangle / u_b$ and $\langle v \rangle / u_b$ in the spanwise mid-plane with experimental data for large-eddy simulation of a flow in lid-driven cavity at $Re = 10,000$, obtained on a series of refined grids, $32 \times 32 \times 16$, $64 \times 64 \times 32$, and $128 \times 128 \times 64$, using WALE model.

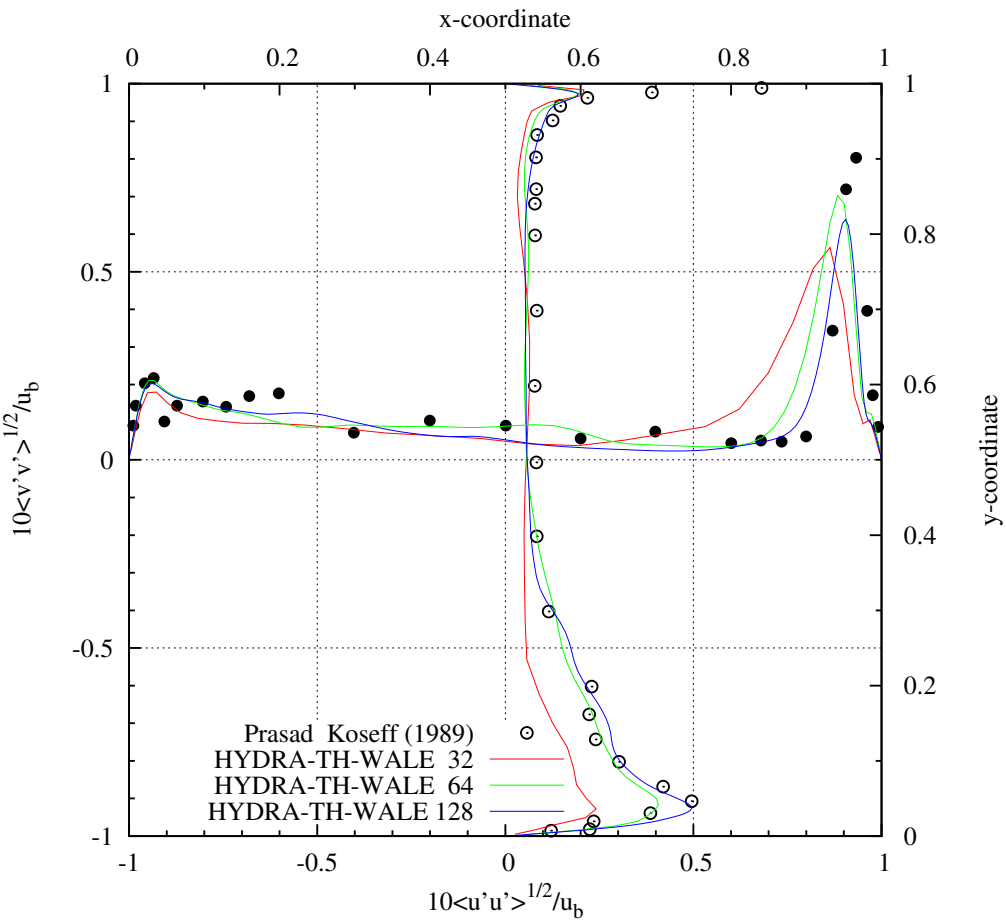

Figure 3.11: Comparisons of scaled RMS velocity components $10\sqrt{\langle u'u' \rangle}/u_b$ and $10\sqrt{\langle v'v' \rangle}/u_b$ in the spanwise mid-plane with experimental data for large-eddy simulation of a flow in lid-driven cavity at $Re = 10,000$, obtained on a series of refined grids, $32 \times 32 \times 16$, $64 \times 64 \times 32$, and $128 \times 128 \times 64$, using WALE model.

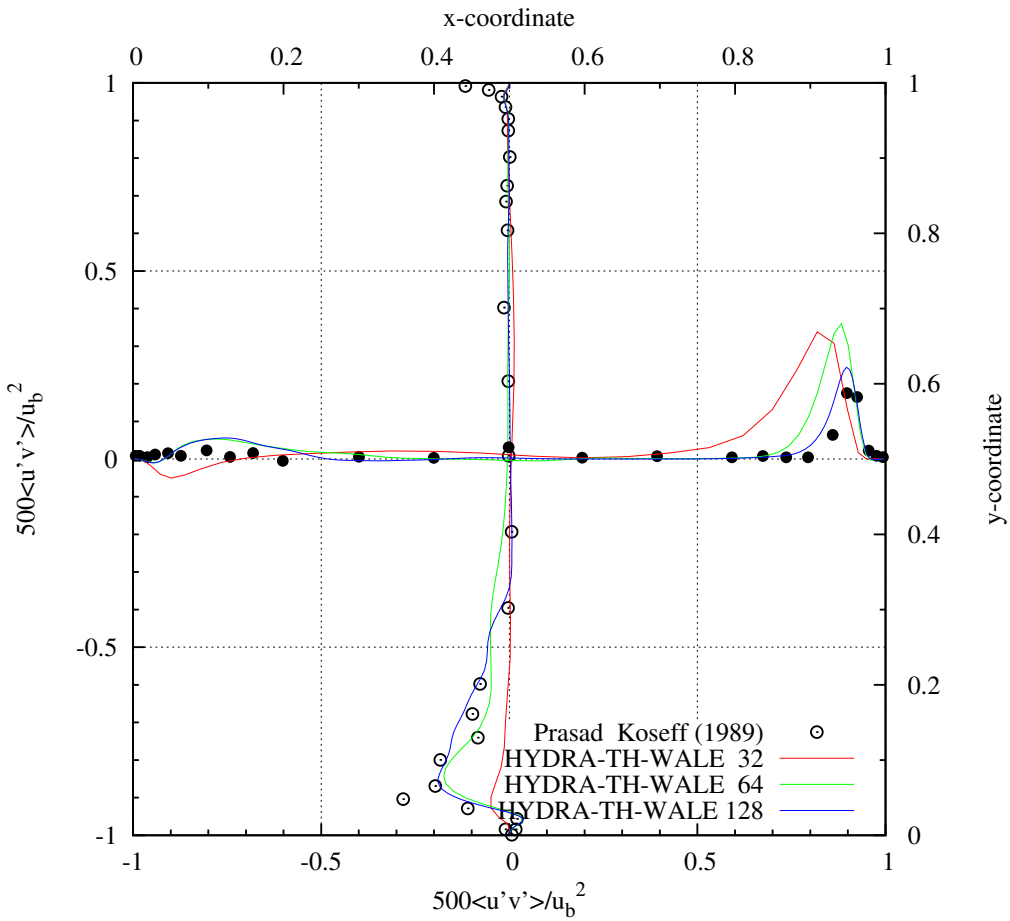

Figure 3.12: Comparisons of scaled Reynolds stress tensor components $500\langle u'v'\rangle/u_b^2$ in the spanwise mid-plane with experimental data for large-eddy simulation of a flow in lid-driven cavity at $Re = 10,000$, obtained on a series of refined grids, $32 \times 32 \times 16$, $64 \times 64 \times 32$, and $128 \times 128 \times 64$, using WALE model.

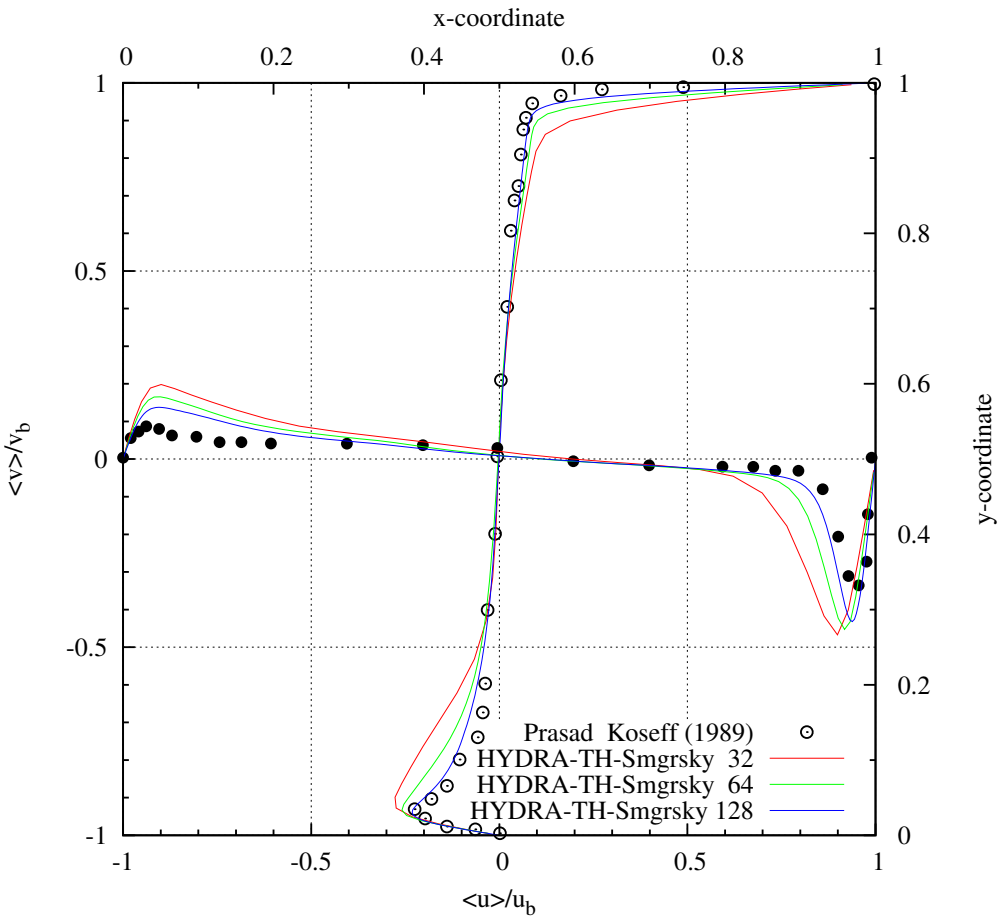

Figure 3.13: Comparisons of mean velocity components $\langle u \rangle / u_b$ and $\langle v \rangle / u_b$ in the spanwise mid-plane with experimental data for large-eddy simulation of a flow in lid-driven cavity at $Re = 10,000$, obtained on a series of refined grids, $32 \times 32 \times 16$, $64 \times 64 \times 32$, and $128 \times 128 \times 64$, using Smagorinsky model.

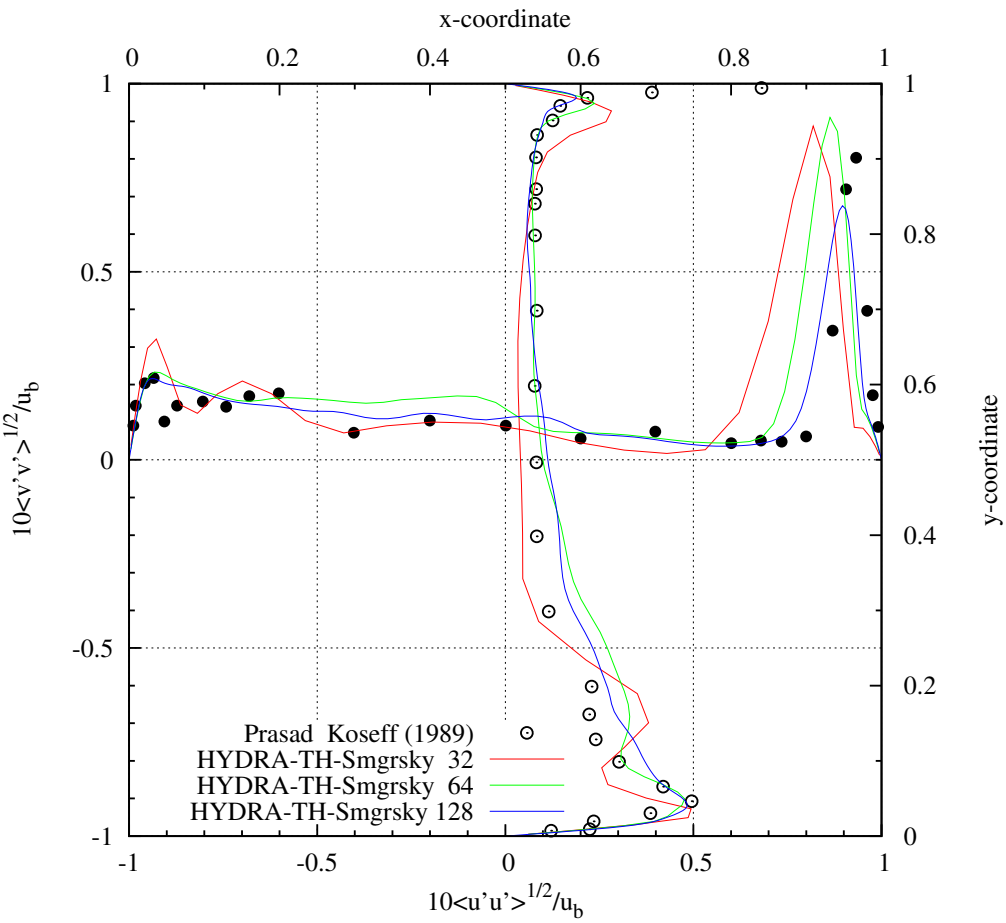

Figure 3.14: Comparisons of scaled RMS velocity components $10\sqrt{\langle u'u' \rangle}/u_b$ and $10\sqrt{\langle v'v' \rangle}/u_b$ in the spanwise mid-plane with experimental data for large-eddy simulation of a flow in lid-driven cavity at $Re = 10,000$, obtained on a series of refined grids, $32 \times 32 \times 16$, $64 \times 64 \times 32$, and $128 \times 128 \times 64$, using Smagorinsky model.

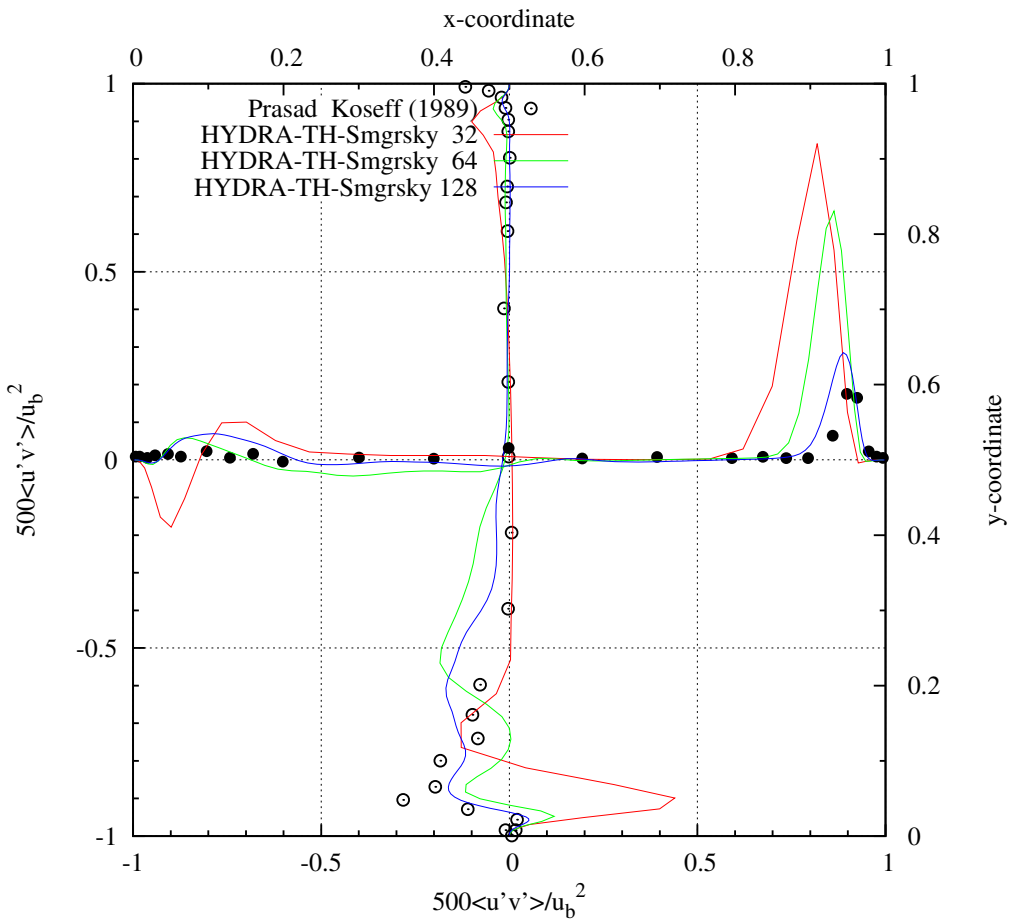

Figure 3.15: Comparisons of scaled Reynolds stress tensor components $500\langle u'v'\rangle/u_b^2$ in the spanwise mid-plane with experimental data for large-eddy simulation of a flow in lid-driven cavity at $Re = 10,000$, obtained on a series of refined grids, $32 \times 32 \times 16$, $64 \times 64 \times 32$, and $128 \times 128 \times 64$, using Smagorinsky model.

Chapter 4

Thermal-Hydraulic Benchmark Problems

The Thermal-Hydraulic benchmark problems described here were motivated by the benchmarks designed for the Thermal-Hydraulics Methods focus area of the Consortium for Advanced Simulation of Light-Water reactors (CASL). The problems presented here can require significant computing resources, and those with grid resolution of $\approx 100 \times 10^6$ elements may be considered in some respects as "hero" calculations.

4.1 3×3 Grid-to-Rod Fretting Rod Bundle

4.1.1 Problem Description

Within the core of a pressurized-water nuclear reactor, water flow is used to cool the irradiated fuel rods. The flow in the reactor core can lead to a process known as grid-to-rod fretting. Grid-to-rod fretting (GTRF) is a flow-induced vibration problem that results in wear and failure of the rods. GTRF wear is one of the leading causes for leaking nuclear fuel and costs power utilities millions of dollars in preventive measures. In order to understand the root causes of such fuel leaks, we investigate the complex turbulent coolant flow around fuel-rod bundles. Our ultimate goal is to accurately predict the turbulent excitation forces on the fuel rods, along with the coupled structural response of the rods and their supports. To date, it has not been possible to completely characterize the flow-induced fluid-structure interaction (FSI) problem for GTRF. Indeed, given the incompressible nature of the coolant, the relatively high Reynolds number, and the flexible character of the fuel rods and spacers, the FSI problem at the reactor core scale is daunting.

This section discusses the use of large-eddy simulation (LES) with Hydra-TH for computing the GTRF problem. The second-order semi-implicit incremental projection method, discussed in [4], is used to solve the single-phase incompressible Navier-Stokes equations governing an isothermal flow. The calculations use hybrid meshes, containing different cell types, generated with Hexpress from Numeca [1] ,for a 3×3 rod-bundle sub-assembly. Here, we summarize calculations using implicit LES (ILES). Additional details on calculations using LES, DES, and the Spalart-Allmaras turbulence models using meshes generated by CUBIT may be found in [5]. More detailed studies are reported on in [1] and [12].

[1] http://www.numeca.be/index.php?id=hexhyb

4.1.2 Problem Setup

The flow conditions for the 3×3 GTRF rod bundle follow those used by Elmahdi, et al. [9] and Shadid, et al. [16]. For the calculations reported here, the working fluid is water at a temperature of 394.2 K, a density of 942.0 kg/m^3, and a dynamic viscosity of 2.32×10^{-4} $kg/m/s$. The inlet velocity is prescribed as $\mathbf{v} = (0, 0, 5)$ m/s. This corresponds to a Reynolds number, based on the rod diameter, of $Re_D = 1.93 \times 10^5$, while the Reynolds number based on the hydraulic diameter is $Re_{D_h} = 4.01 \times 10^5$. The hydraulic diameter is defined as $D_h = 4A_{flow}/P_{wet}$. No-slip, no-penetration conditions are prescribed at the rod and spacer surfaces. At the outlet, the hydrostatic pressure is specified to be $p_h = 0.0$ in conjunction with a zero shear stress condition. For the first set of calculations, no-penetration conditions with in-plane slip were applied at the subchannel boundaries as shown in Figure 4.1.

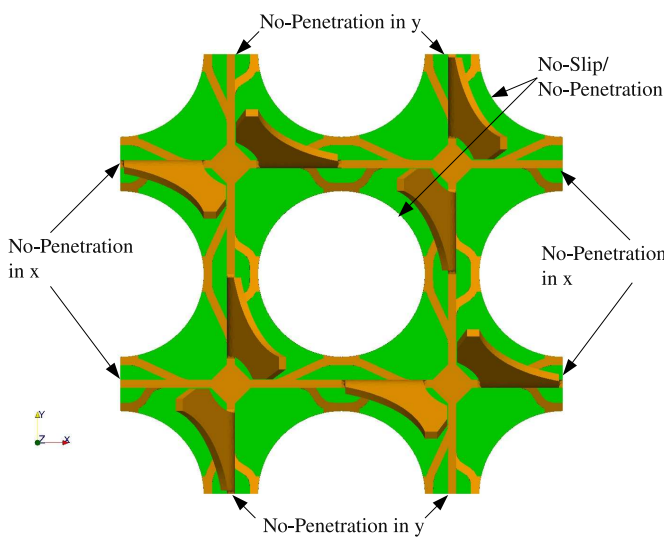

Figure 4.1: Boundary conditions on rod and spacer surfaces, and subchannel boundaries.

We generated a series of meshes for the V5H GTRF spacer geometry for the 3×3 rod bundle configurations. The approximate cell count for the 3×3 meshes are 2 million (M), 7M, 30M, 47M, 80M, and 185M. Snapshots of the 7M and 47M meshes for the 3×3 rod bundle are displayed in Figure 4.2. Visual inspection of these meshes reveal uniform cell sizes inside the domain with targeted refinement in corners and edges in the vicinity of the spacer and symmetry planes (not shown).

4.1.3 Results

Similar to our earlier LES calculations on the 3×3 rod-bundle [5], a series of preliminary coarse-mesh simulations were conducted using hybrid meshes, containing hex, wedge, tet, pyramid elements, to determine when a statistically stationary flow is achieved. The time-evolution of the domain-average kinetic energy (not shown) was used as an indicator, based on which the time of approximately 0.1 s was chosen as the starting point for collecting time-averaged flow statistics until the end of the

simulation at $t = 1.0\ s$. Six calculations, using meshes with approximately 2 million (M), 7M, 14M, 27M, 30M, and 47M cells have been carried out with a termination time of 1.0 s with statistics collected for $t > 0.1\ s$.

A representative picture of the instantaneous flow behind the mixing vanes is shown in Figure 4.3 with isosurfaces of the helicity. The vortices generated by the spacer and the mixing vanes are advected downstream. Figure 4.3 shows that the neutrally dissipative advection algorithm in Hydra-TH does an excellent job in maintaining the complex vortex structures far downstream, i.e., introduces minimal phase errors.

The instantaneous pressure is plotted in Figure 4.4 for some of the meshes considered in this study. The end-point coordinates of the lines along which the pressure line plots have been obtained are (3.3588E-3, -9.6520E-2, 3.3588E-3) and (3.3588E-3, 3.0480E-1, 0.3.3588E-3). For more detail on the flow geometry see [5]. The vertical lines in Figure 4.4 delineate the bounds of the spacer and the mixing vanes. It is reassuring that the pressure lines are qualitatively very similar for all mesh resolutions. Since the hydrostatic pressure at the outflow is fixed at $p = 0$, the value of the calculated inlet pressure determines the pressure drop over the whole domain.

The mean pressure along the rod is also plotted in Figure 4.4 for the 2M, 7M and 14M meshes. A large drop in the mean pressure through the spacer indicates that most of the pressure loss is due to the spacer. In spite of the turbulent flow induced by the spacer, the characteristic peaks and troughs in the profile of the mean pressure are very much reproducible throughout the spacer using the 2M, 7M, and 14M meshes. Downstream of the mixing vanes a slight wave in the mean pressure is apparent in the coarsest 2M-mesh simulation. The mean pressure using the 7M mesh appears as what one would intuitively expect for a turbulent pipe flow: from approximately $y = 0.175m$, the mean pressure linearly decreases to zero.

The RMS pressure along the rod is plotted in Figure 4.5(a) for the 2M, 7M and 14M meshes. The fluctuating pressure force is probably the most important quantity to compute accurately for a reasonable representation of the forces acting on the fuel rods. The RMS pressure peaks at the downstream end of the spacer for the 7M and 14M meshes. This is expected, since this is where the level of turbulent kinetic energy is the largest. While the downstream locations of the peaks are somewhat aligned for the varying meshes, their amplitudes and downstream evolution are quite different. The 2M mesh is too coarse to adequately capture the second pressure moment. At this point we are not in a position to draw any conclusions regarding the grid-convergence of the RMS pressure. Regardless, the turbulent kinetic energy (and the RMS pressure) must decay downstream as no energy production occurs downstream of the mixing vanes.

The total force and its two components, the pressure and viscous forces, have been extracted in time on the central rod and the spacer. Surface forces are computed by integrating pressure and shear stress over the given surface:

$$F_i(t) = -\int p(t) n_i \mathrm{d}A + 2\int \mu S_{ij}(t) n_j \mathrm{d}A, \tag{4.1}$$

where $\mathbf{F}$, p, $\mathbf{n}$, A, and $S_{ij} = (v_{i,j} + v_{j,i})/2$ denote the total force, pressure, outward surface normal, surface area, and the strain rate of the instantaneous velocity, $\mathbf{v}$, respectively. This gives the force time history that can be used to compute power spectral distributions or fed directly into structural dynamics codes to compute wear. The total, pressure, and viscous force time-histories for the 7M case are presented in Figure 4.7, which shows that the mean forces are similar to those computed using the CUBIT meshes presented in [5]. On the other hand the pressure force acting on the central

CASL-U-2013-0324-000-b

rod, probably the most important quantity for the GTRF problem, shows much larger fluctuations about the mean for the Spider mesh relative to the CUBIT results.

The total forces have also been integrated in 12 one-inch segments downstream of the mixing vanes. This gives details on the spatial distribution of the forces loading the central rod and allows for a more direct comparison with the LES results presented by Elmahdi, et al. [9]. In Figure 4.5(b) the RMS total force is given in segments for the 7M, 14M, and 27M meshes, compared to that of the Elmhadi, et al. results using a 47M-cell mesh. The RMS forces extracted from the 2M simulation are inadequate to provide meaningful second moments of the force loading the rod and are not shown. The RMS forces computed by Hydra-TH using the 7M, 14M, and 27M meshes are quite close and appear to converge to those reported by Elmhadi, et al. with a 47M mesh resolution.

Additional insight into the fluctuating velocity field is found by examining the turbulent kinetic energy and Reynolds stresses shown in Figure 4.6. In Figure 4.6(a) the downstream spatial evolution of the turbulent kinetic energy (TKE) is plotted for the 2M, 7M, and 14M meshes. Similar to the pressure variance in Figure 4.5, the TKE, $k = \langle \mathbf{v}' \cdot \mathbf{v}' \rangle / 2$, peaks in the vicinity of the mixing vanes and stays at a relatively high value until approximately 0.2m downstream. This reinforces our earlier observation that the highest level of TKE occurs close to the downstream edge of mixing vanes . Figure 4.6(a) also indicates that the 2M-cell mesh is too coarse to produce a qualitatively correct TKE evolution; similar to the RMS pressure, the TKE should also decay downstream.

Figure 4.6(b) depicts the downstream evolution of the different components of the Reynolds stress tensor, $\langle \mathbf{v}'\mathbf{v}' \rangle$ for the 14M mesh. The figure shows that the flow downstream of the mixing vanes remains highly anisotropic until the end of the computational domain: almost all kinetic energy is in the streamwise component, $\langle v'v' \rangle$, of the velocity, $\mathbf{v} = (u, v, w)$, i.e., the streamwise fluctuations are large compared that of both cross-stream components, $\langle u'u' \rangle$, $\langle w'w' \rangle$, in x and z directions, respectively.

4.1.4 Control Files

A representative control file for the 3×3 GTRF LES calculations is shown in Figure 4.1.4. The control file may be found in the `3D/3x3_gtrf` directory.

4.1.5 Mesh Files

The mesh files for this problem are extremely large, and are not provided for this problem.

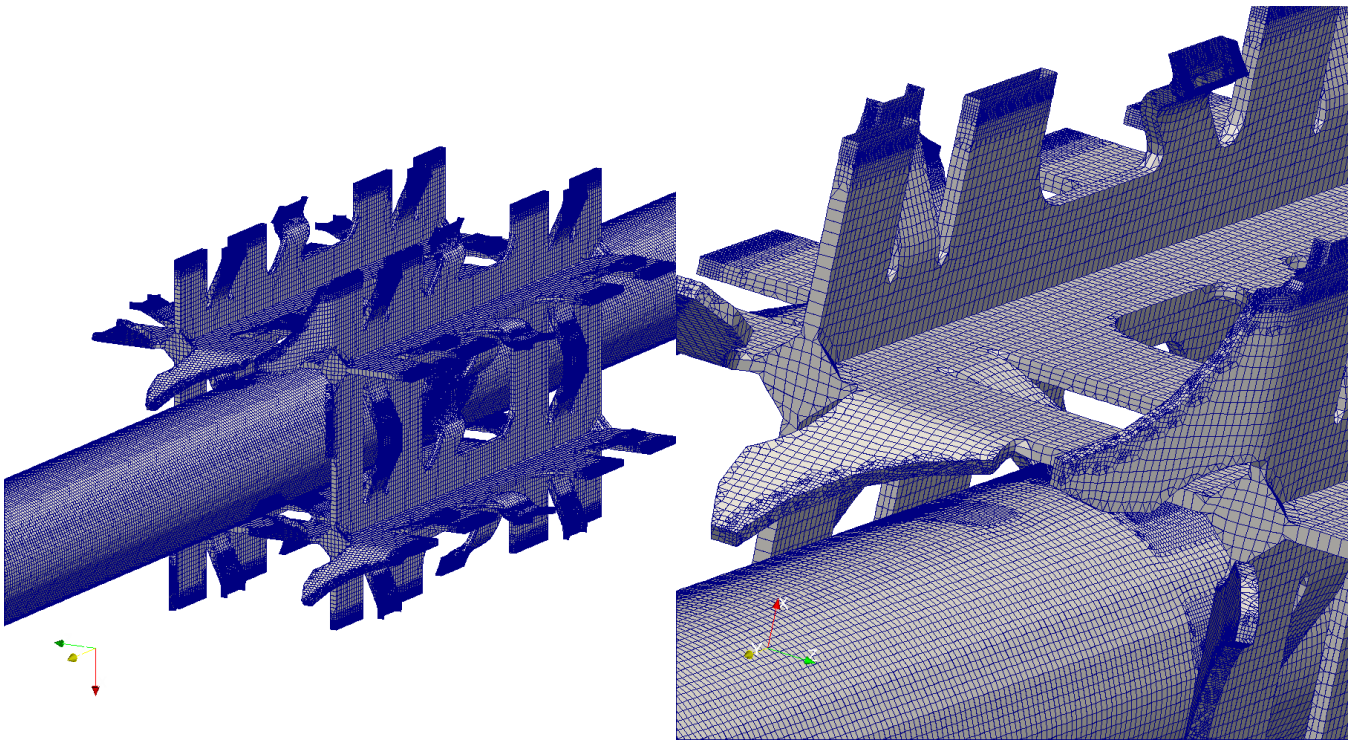

(a)

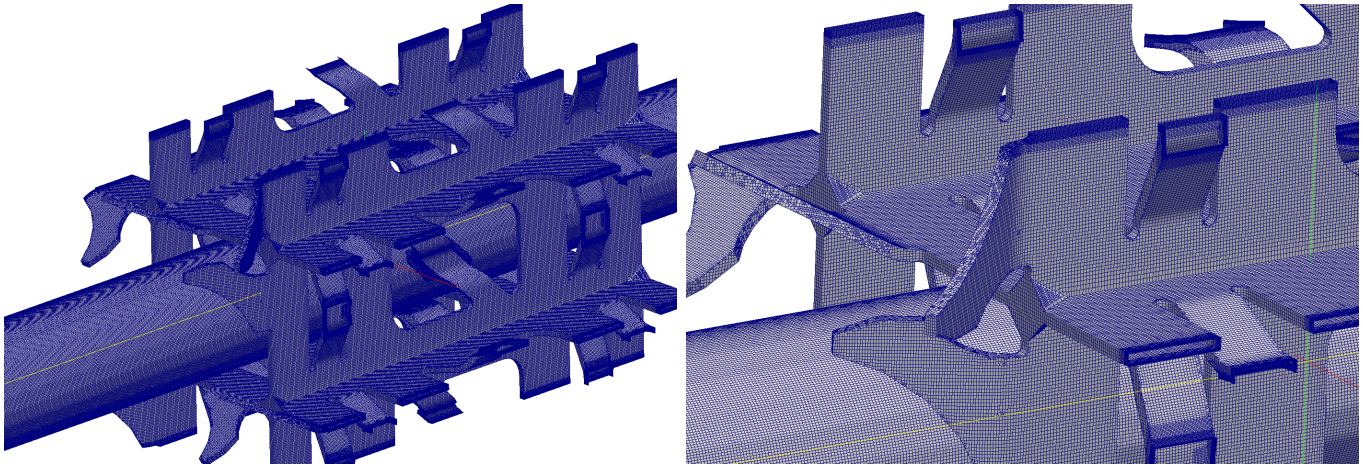

(b)

Figure 4.2: Surface meshes for the (a) 7M and (b) 47M grids for the V5H GTRF 3 × 3 rod bundle.

CASL-U-2013-0324-000-b

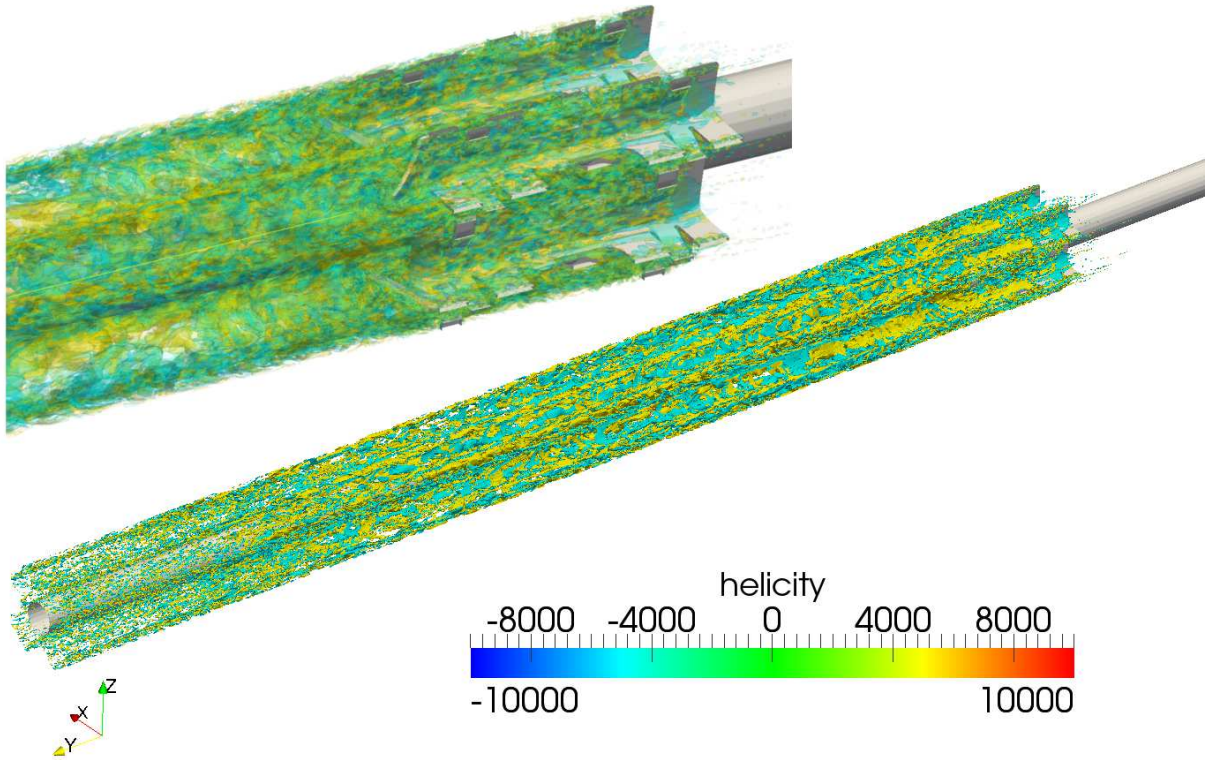

Figure 4.3: Instantaneous snapshots of helicity ($\mathbf{v}\cdot\omega$) isosurfaces for the 2M and 47M Spider meshes.

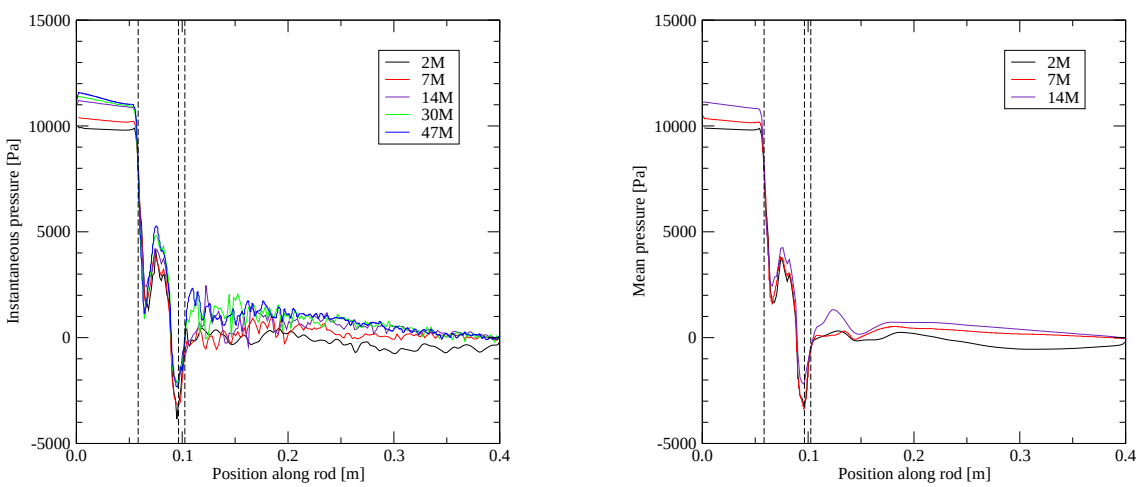

(a) (b)

Figure 4.4: Instantaneous (a) and mean (b) pressure line plots for different meshes.

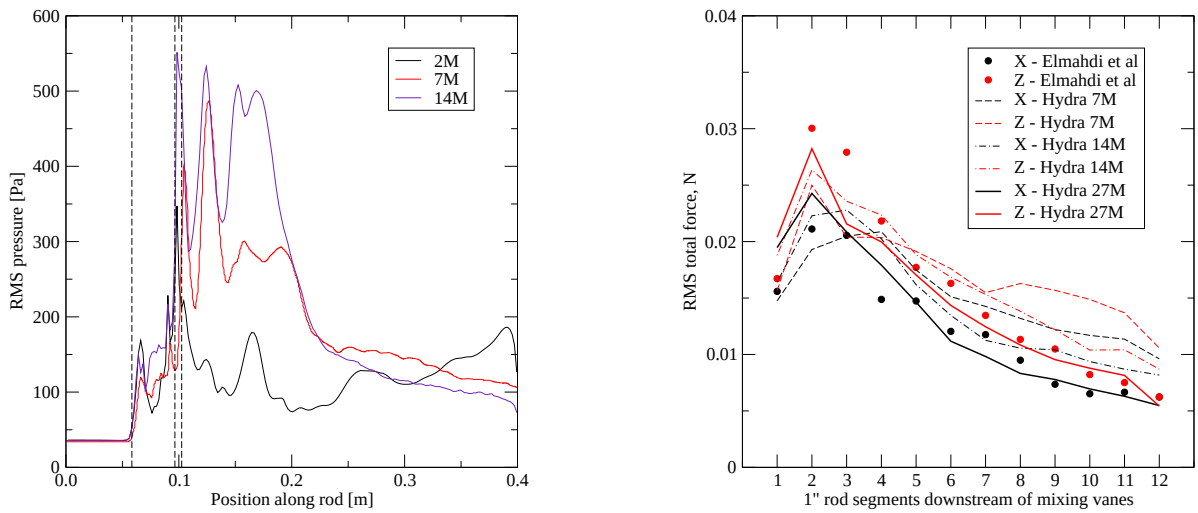

(a) (b)

Figure 4.5: (a) RMS pressure integrated over the full length of the central rod for three different meshes, (b) RMS total force on the central rod integrated in 1-inch segments downstream of the mixing vanes. The Star-CCM+ results are from the LES calculations in [9].

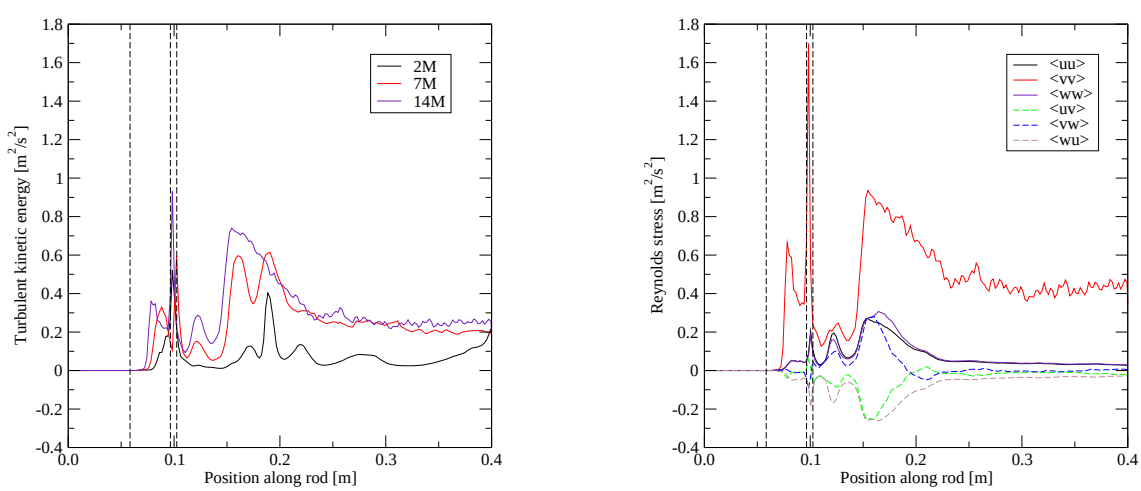

(a) (b)

Figure 4.6: Second moments of the fluctuating velocity field for three different meshes: (a) turbulent kinetic energy along the rod for three different meshes, (b) Reynolds stress along the rod for the 14M mesh.

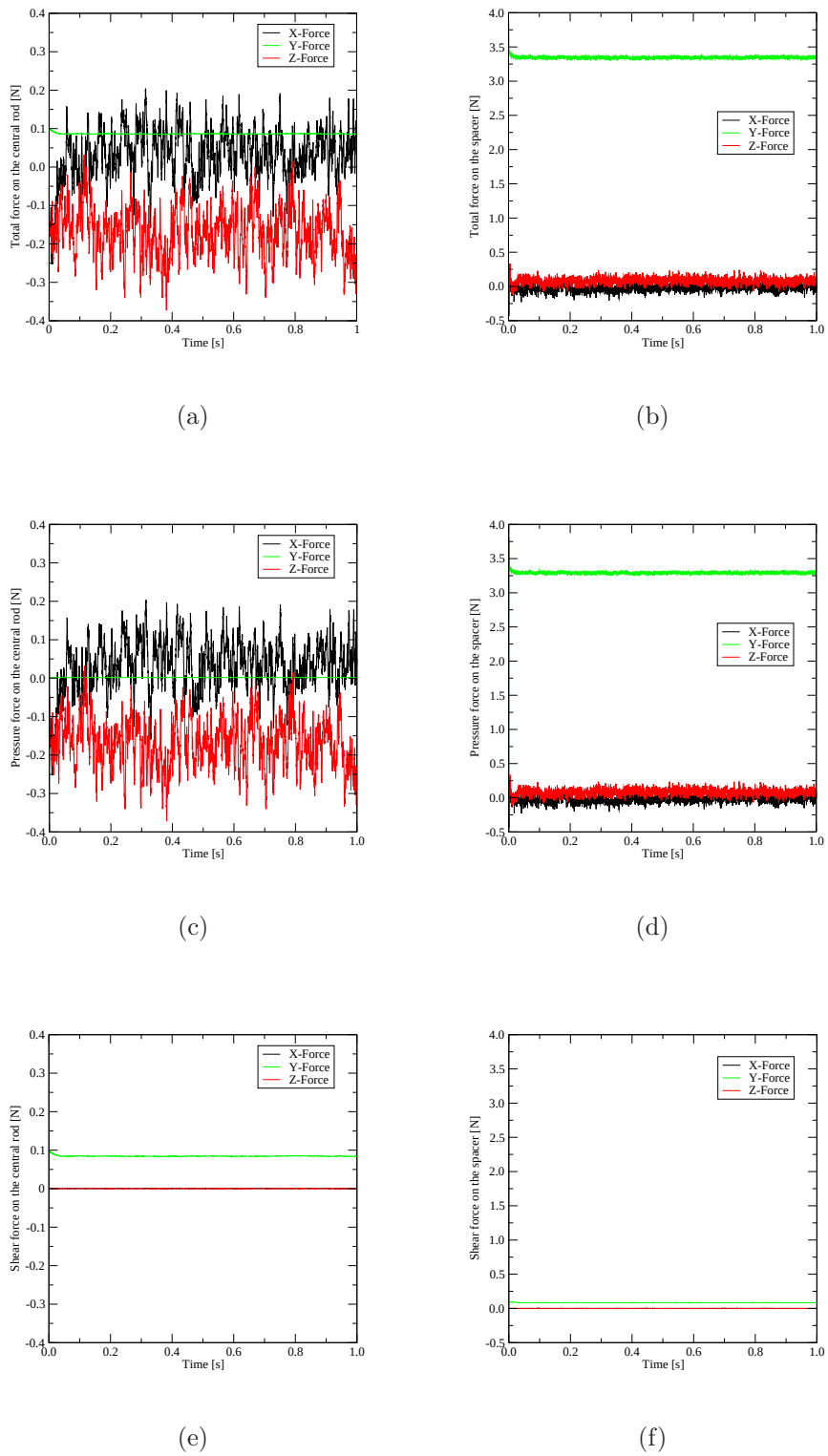

Figure 4.7: Total, pressure, and shear force time histories on the central rod and spacer for the 7M Spider mesh: (a) Total force on the central rod, (b) Total force on the spacer, (c) Pressure force on the central rod, (d) Pressure force on the spacer, (e) Shear force on the central rod, and (f) Shear force on the spacer.

```
title
GTRF Elmahdi Spider

cc_navierstokes

  nsteps  40000
  deltat  0.01
  term    1.0

  time_integration
    type    fixed_cfl
    CFLinit 1.0
    CFLmax  5.0
    dtmax   0.05
    dtscale 1.025
    thetaa  0.5
    thetak  0.5
    thetaf  0.5
  end

  # Output options
  pltype exodusii
  filetype distributed
  plti   250
  ttyi   500
  dump   2000

  # Material model setup &
  # assignment to sets
  material
    id  1
    rho 942.0
    mu  2.32e-4
  end

  load_balance
    method   rcb
  end

  materialset
    id 10
    material 1
    block 1
    block 2
    block 3
    block 4
  end

  # Simple IC's
  initial
    velx 0.0
    vely 5.0
    velz 0.0
    turbnu 5.0e-7
  end

  # Activate statistics
  statistics
    starttime   0.1
    endtime     1.0
    plotwinsize 0.05
  end

  plotvar
    elem div
    elem vel
    elem procid
    elem volume
    elem vginv2
    node dist
    node enstrophy
    node pressure
    node vel
    node vorticity
    node helicity

    # wall shear on the
    # rods and spacers
    side 8 wallshear
    side 9 wallshear
    side 10 wallshear

    # yplus on the rods
    # and spacer
    side 8 yplus
    side 9 yplus
    side 10 yplus

    # straction on the
    # rods and spacers
    side 8 straction
    side 9 straction
    side 10 straction
  end

  histvar
    # forces on the
    # rods and spacers
    side 8 force
    side 9 force
    side 10 force

    side 8 pressforce
    side 9 pressforce
    side 10 pressforce

    side 8 viscforce
    side 9 viscforce
    side 10 viscforce
  end

  plotstatvar
    node <pressure>
    node <pressure',pressure'>

    elem <velocity>
    elem <vorticity>
    elem <helicity>
    elem tke
    elem reynoldsstress

    side 9 <pressure>
    side 9 <pressure',pressure'>
  end

  pressure
    sideset 2 -1 0.0 # Outflow
  end

  velocity
    # X+ Symmetry
    velx sideset 4 -1 0.0
    # X- Symmetry
    velx sideset 6 -1 0.0

    # Z- Symmetry
    velz sideset 7 -1 0.0
    # Z+ Symmetry
    velz sideset 5 -1 0.0

    # Inflow
    velx sideset 3 -1 0.0
    vely sideset 3 -1 5.0
    velz sideset 3 -1 0.0

    # Rods
    velx sideset 9 -1 0.0
    vely sideset 9 -1 0.0
    velz sideset 9 -1 0.0

    velx sideset 10 -1 0.0
    vely sideset 10 -1 0.0
    velz sideset 10 -1 0.0

 # Spacer
    velx sideset 8 -1 0.0
    vely sideset 8 -1 0.0
    velz sideset 8 -1 0.0
  end

  ppesolver
    type  AMG
    amgpc HYPRE
    hypre_type BOOMERAMG
    strong_threshold 0.7
    levels 20
    itmax 100
    itchk 1
    coarse_size 1500
    diagnostics off
    convergence off
    eps   1.0e-5
  end

  momentumsolver
    type  ILUFGMRES
    itmax 50
    itchk 2
    restart 25
    diagnostics off
    convergence off
    eps   1.0e-5
  end

end

exit
```

Figure 4.8: Representative control file for 3 × 3 GTRF LES calculations.

CASL-U-2013-0324-000-b

4.2 5×5 Rod Bundle

4.2.1 Problem Description

This section presents the results of preliminary calculations for the 5×5 Westinghouse fuel rod bundle. The geometry was provided in CAD format by Westinghouse, and corresponds to the experimental configuration used at Texas A&M where PIV measurements were carried out. The flow domain is shown in Figure 4.9. Not shown here are the exterior walls of the flow housing used in the experimental facility. Additional details on the experimental configuration and results may be found in Conner, et al. [6].

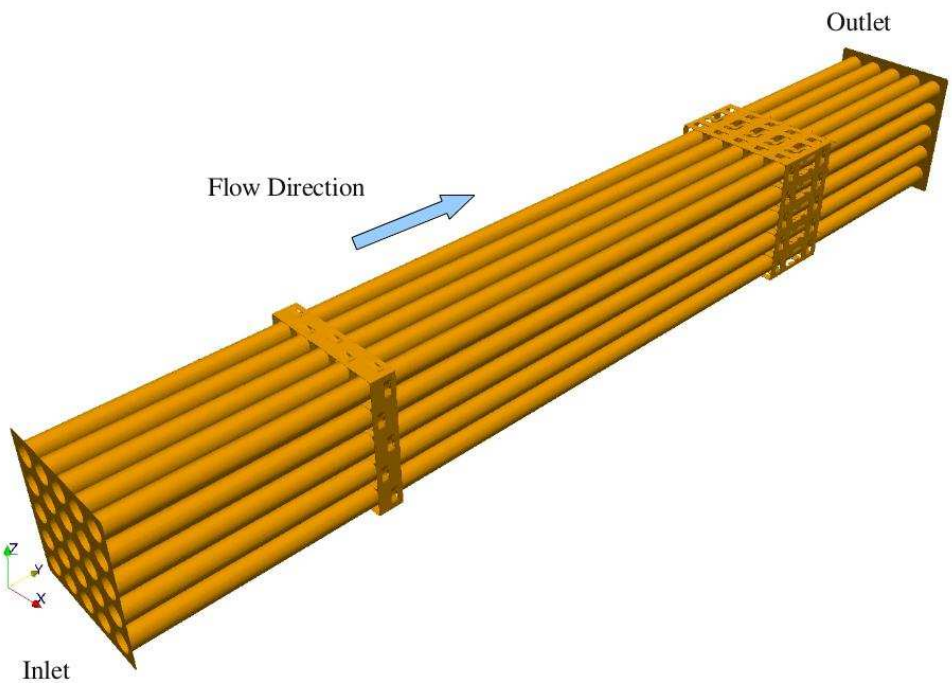

Figure 4.9: Flow domain for the 5×5 rod bundle showing the rods, the inlet/outlet planes, the support, and the spacer grid.

At the inlet of the flow domain, a constant prescribed velocity $(0.0, 2.48, 0.0)$m/s is applied with the fluid properties for water at 24°C and atmospheric pressure. This corresponds to a Reynolds number of approximately $28,000$ based on the hydraulic diameter for the rod bundle. At the surfaces of the flow housing, rods, support and spacer grids, no-slip/no-penetration velocity conditions were prescribed. Homogeneous Neumann conditions for velocity along with a zero-pressure condition were prescribed at the outflow plane. A fixed $CFL = 4$ condition was used with automatic time-step control for all computations.

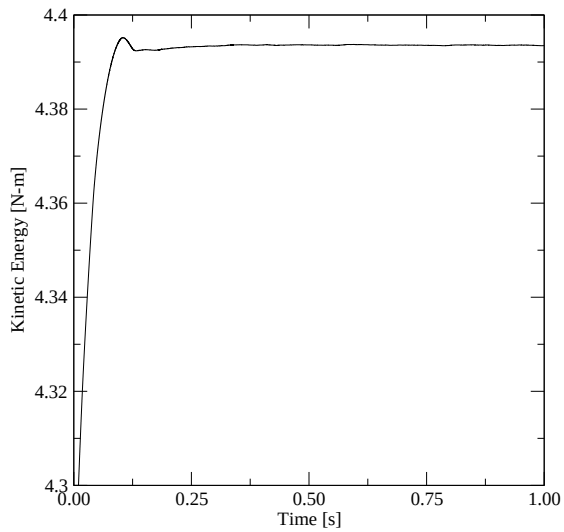

Figure 4.10: Domain-average kinetic energy, $\int \rho \mathbf{v} \cdot \mathbf{v}/2 \mathrm{d}\Omega$, vs. time for the 14M 5×5 rod bundle.

4.2.2 Problem Setup

Following the procedures to perform LES calculations on the 3×3 rod-bundle, outlined in [5], a series of preliminary coarse-mesh calculations were conducted to determine when a stationary turbulent state would be achieved and to test the sensitivity to mesh resolution and the time-step size. Figure 4.10 shows the global, i.e. domain-average, kinetic energy, $\int \rho \mathbf{v} \cdot \mathbf{v}/2 \mathrm{d}\Omega$, as a function of time. Here Ω denotes the volume of the flow domain. Based on these preliminary calculations, a time of approximately 0.2s was chosen as the starting point for collecting time-averaged flow statistics until the end of the simulation at $t = 1.0$s.

4.2.3 Results

In order to illustrate the impact of increasing mesh resolution on the flow, Figure 4.11 shows snapshots of the instantaneous helicity field for the 5×5 rod bundle for two different mesh resolutions. For the 14M mesh, there are relatively large coherent structures downstream of the support and spacer grid. In contrast, the flow structures captured by the 96M mesh are significantly smaller and appear more randomly distributed spatially. In both cases, the influence of the mixing vanes on the spacer grid is apparent.

In order to compare to the experimental data, discussed in [18], a series of line plots were extracted from the mean velocity field for the 14M-mesh 5×5 run at locations that fall in the planes of the PIV measurements. All line data were measured relative to the so-called "weld-nugget" located on the spacer grid. The "weld nugget" is located at 38.1 mm from the bottom of the spacer grid [17] as shown in Figure 4.12(a). The line-data extracted from the computation was located at the positions indicated in Figure 4.12. The coordinates of the sample points A – H are shown in Table 4.1 and are relative to the center of rod 13 in Figure 3 in [18]. In the flow direction, the line-data is extracted for $0.05 \leq y \leq 0.09$ m corresponding to the region where

CASL-U-2013-0324-000-b

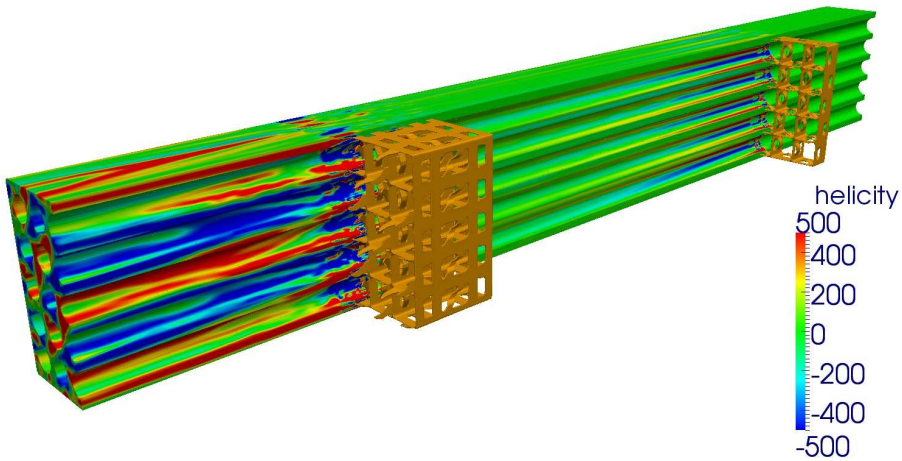

(a)

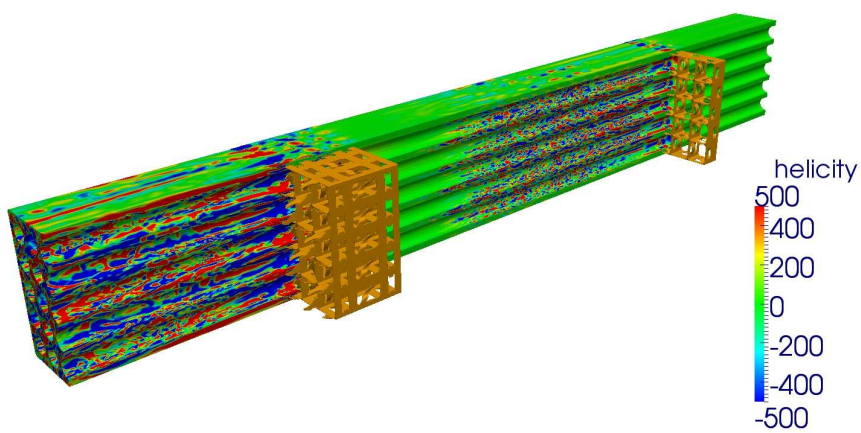

(b)

Figure 4.11: Snapshots of the instantaneous helicity field for the (a) 14M and (b) 96M element meshes.

Point	(x, z) Position $[10^{-3}m]$
A	(-6.3, 6.3)
B	(-6.3, 0.0)
C	(-6.3, -6.3)
D	(0.0, -6.3)
E	(6.3, -6.3)
F	(6.3, 0.0)
G	(6.3, 6.3)
H	(0.0, 6.3)

Table 4.1: Sample points A – H used to extract line-data for comparison with experimental data.

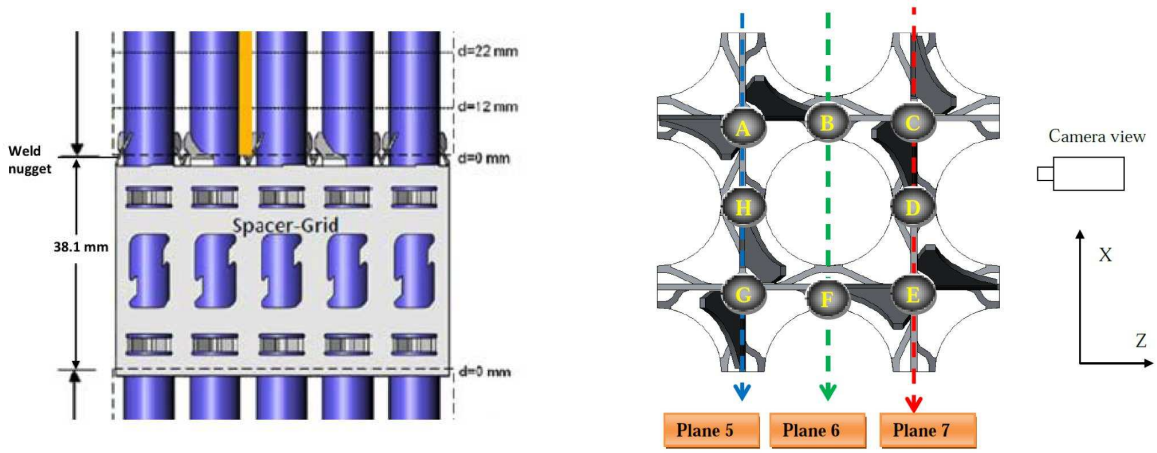

(a) Weld nugget location.

(b) Sample points.

Figure 4.12: Locations relative to the "weld nugget" used for extracting data along planes 5, 6 and 7. (Reproduced from [18]) without permission.)

PIV data is available in the region downstream of the spacer grid. Following Yan, et al. [18], mean velocities are compared at points A, C, D, E, G, and H as shown in Figure 4.14. Here, the streamwise velocity in the experiments corresponds to the y-velocity in the computation, while the lateral velocity corresponds to the x-velocity. Yan, et al. [18], estimated the systematic uncertainty in the velocities due to the PIV measurements, software acquisition, etc, to be a maximum of 0.199m/s. The statistical uncertainty, which is a function of the number of snapshots of the velocity, is estimated to be $\pm 0.167 V_{\text{inlet}}$ in the lateral direction, and $\pm 0.15 V_{\text{inlet}}$ in the axial direction, where $V_{\text{inlet}} = 2.48$m/s. All experimental data has been plotted with the uncertainty bounds provided by Dominguez-Ontiveros and Hassan, see also [6].

The line plots of velocity for the 96M mesh are presented in Figure 4.14 for stations A – H. The 96M results match the experimental data more closely at all points A – H. However, the streamwise velocity still appears to be slightly over-predicted. In contrast, the x-velocities fall within the uncertainty bounds for points A, C, E, and G, while the x-velocities at points D and H have similar profiles but are not quite within the uncertainty bounds. Overall, the 96M results compare very well to the experimental data.

Time-averaged velocities in plane-5, see Figure 4.12, from [6] are shown in Figure 4.15 with the computed time-averaged mean velocity fields. Similarly, the experimental and computed mean velocity fields on plane-7 are shown in Figure 4.16. The data in the figures have been scaled relative to the 2.48m/s inlet velocity. The peak velocities in the axial direction are slightly under-predicted in the Hydra-TH computations, while the lateral velocities are slightly over-predicted. This is likely due to the very coarse mesh used in this LES calculation. While the peak velocities appear to be relatively close to those found experimentally, inspection of Figures 4.15 and 4.16 indicates that the deflection in the velocity vectors due to the mixing vanes and the flow housing is well-captured by the simulation.

CASL-U-2013-0324-000-b

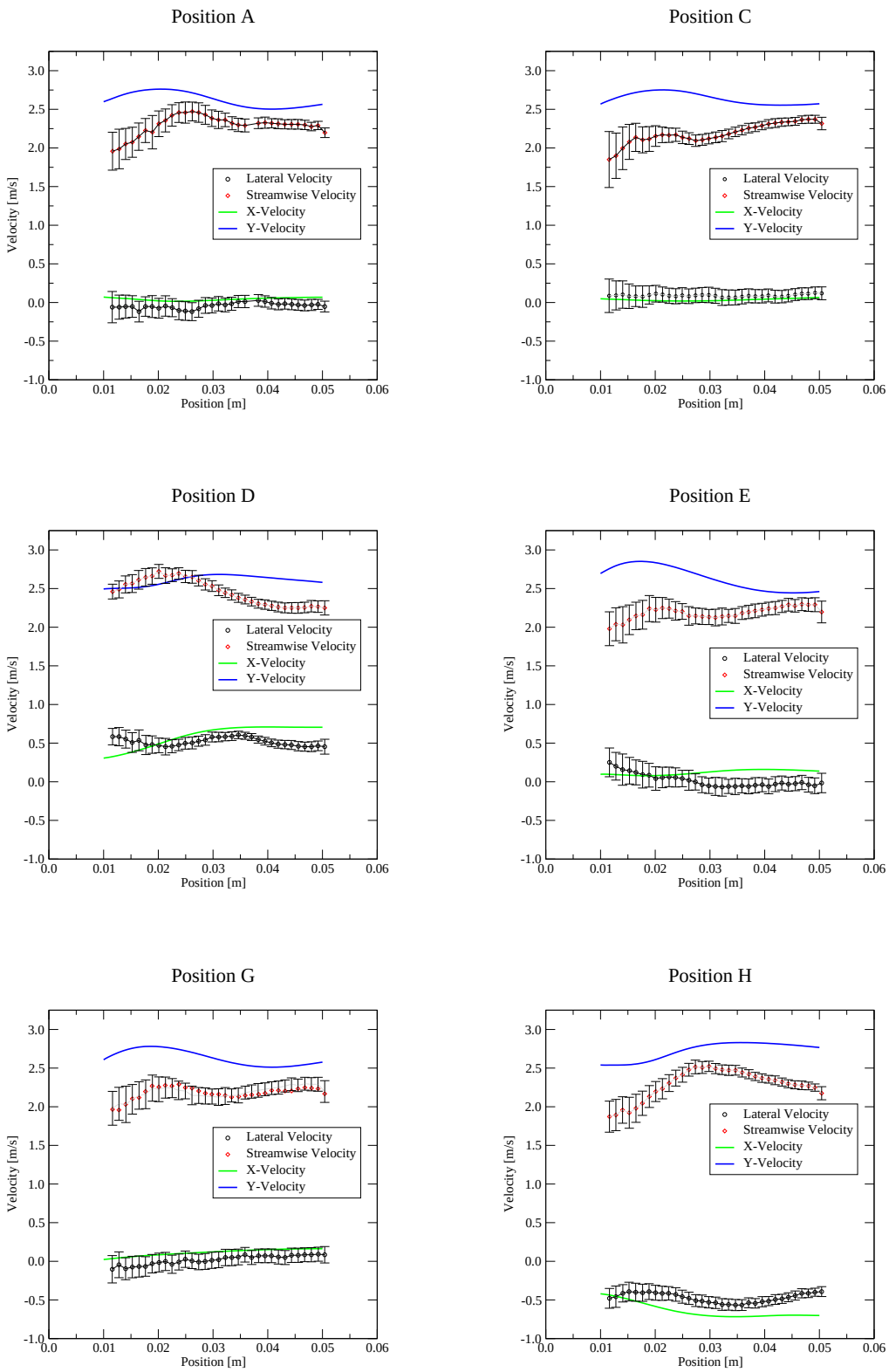

Figure 4.13: Mean axial and lateral velocity profiles at positions A, C, D, E, G and H for the 14M mesh.

4.2.4 Control Files

The control file for the 5×5 GTRF LES calculations is shown in Figure 4.2.4. The control file may be found in the `3D/5x5_gtrf` directory.

4.2.5 Mesh Files

The mesh files for this problem are extremely large, and are not provided.

CASL-U-2013-0324-000-b

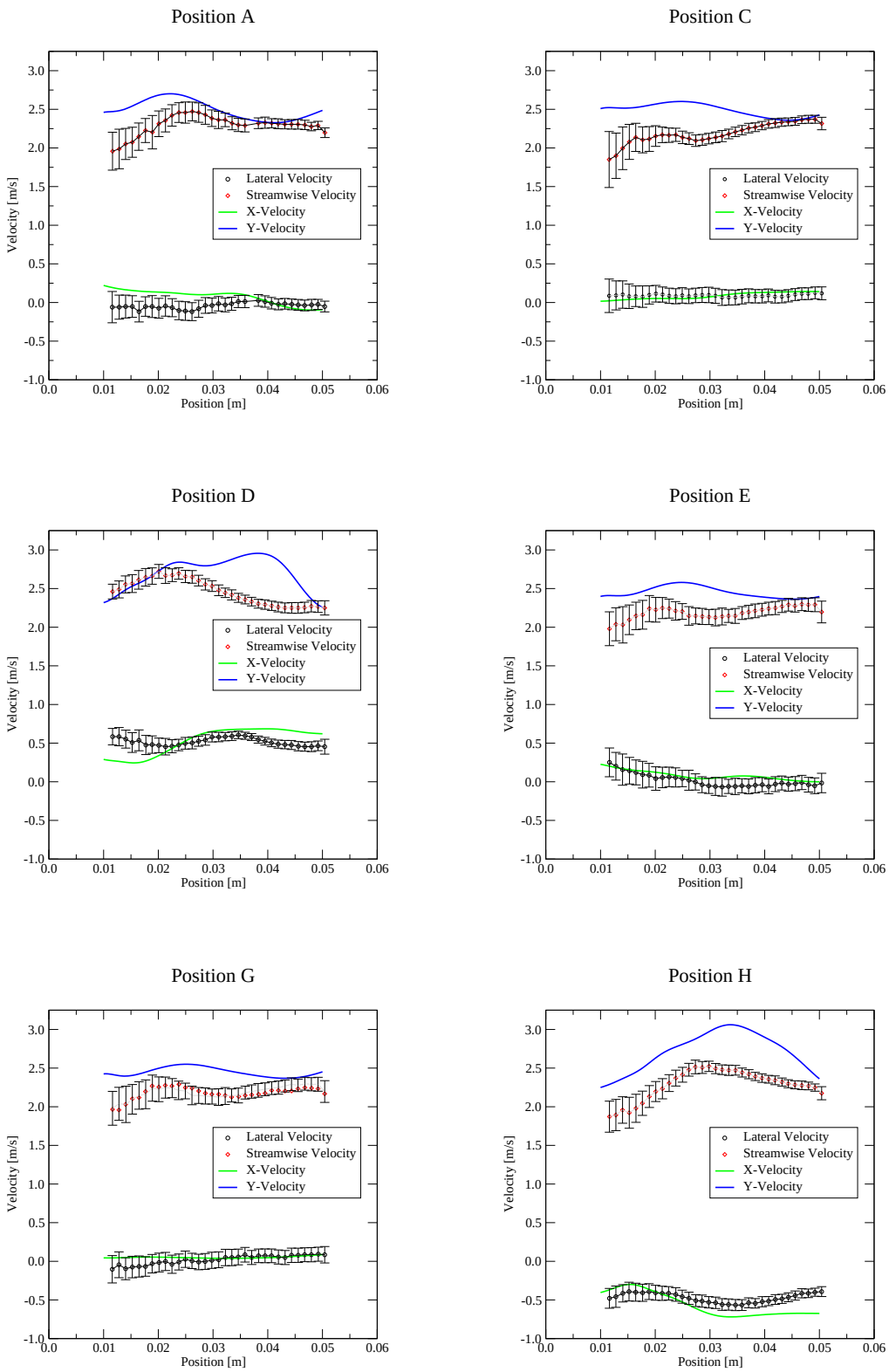

Figure 4.14: Mean axial and lateral velocity profiles at positions A, C, D, E, G and H for the 96M mesh.

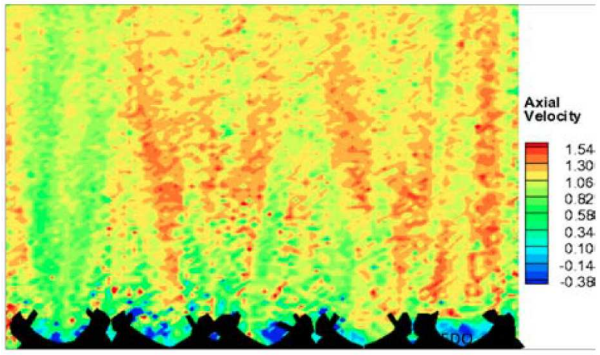

(a) Experimental Axial Velocity

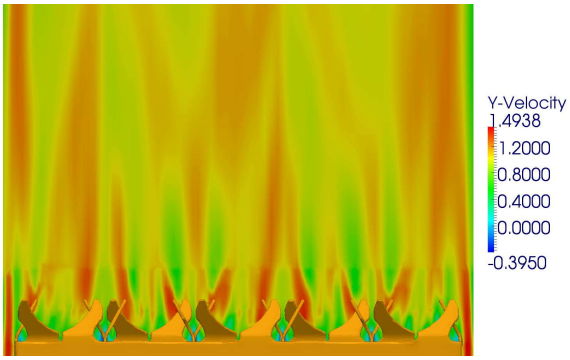

(b) Hydra-TH Y-Velocity

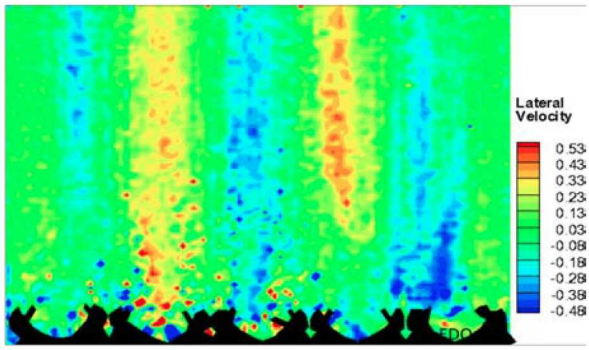

(c) Experimental Lateral Velocity

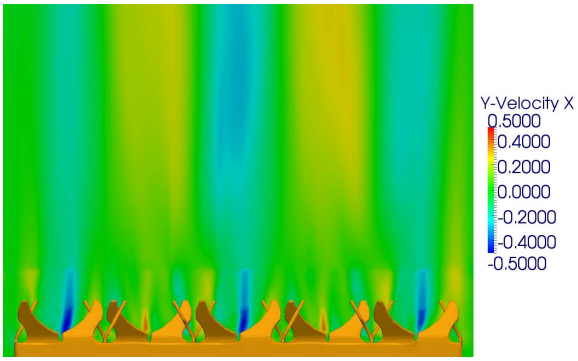

(d) Hydra-TH X-Velocity

Figure 4.15: Experimental and computed axial (y-direction) time-averaged velocities on plane 5. Velocity magnitude has been scaled relative to the 2.48 m/s inlet velocity.

CASL-U-2013-0324-000-b

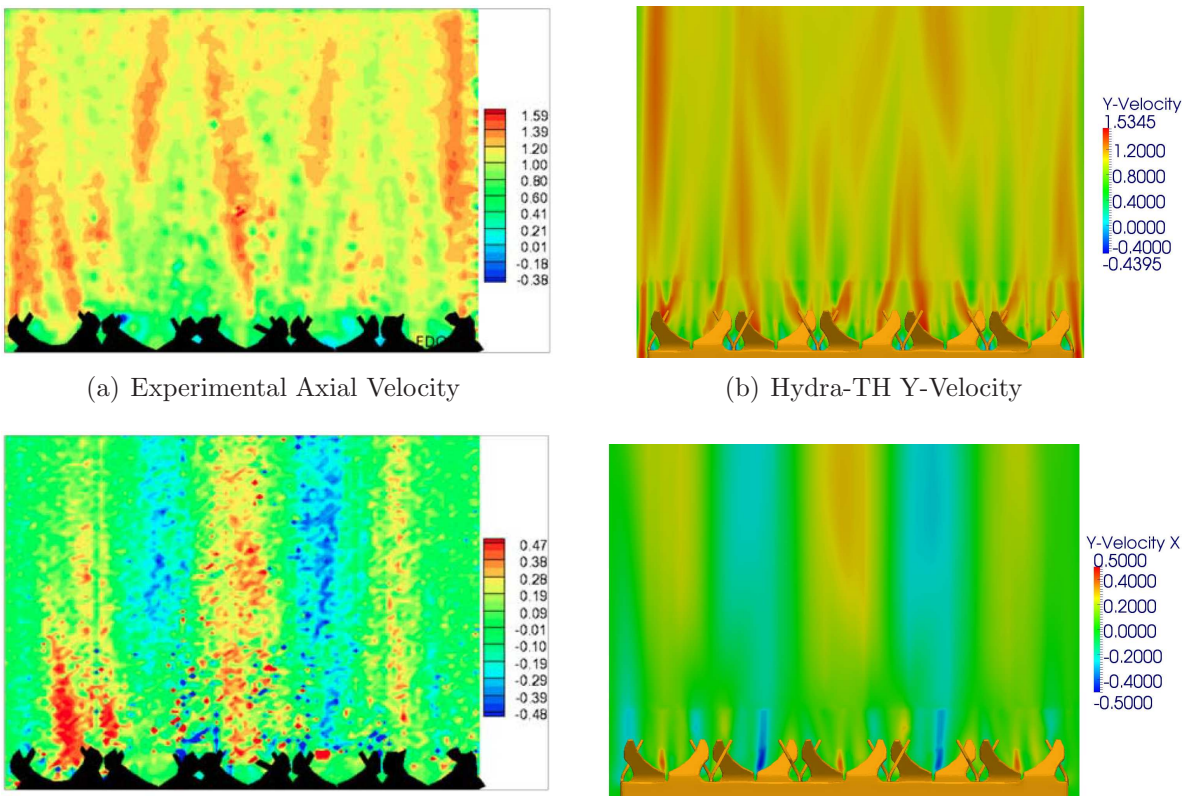

(a) Experimental Axial Velocity

(b) Hydra-TH Y-Velocity

(c) Experimental Lateral Velocity

(d) Hydra-TH X-Velocity

Figure 4.16: Experimental and computed axial (y-direction) time-averaged velocities on plane 7. Velocity magnitude has been scaled relative to the 2.48 m/s inlet velocity.

```
title
GTRF TAMU 5x5 Spider

cc_navierstokes

  nsteps  3500 # 100000
  deltat  0.01
  term    1.0

  time_integration
    type    fixed_cfl
    CFLinit 1.0
    CFLmax  4.0
    dtmax   0.05
    dtscale 1.025
    thetaa  0.5
    thetak  0.5
    thetaf  0.5
  end

  # Output options
  pltype exodusii
  filetype distributed
  plti   250
  ttyi   250
  dump   1500

  # Material model setup &
  # assignment to sets
  material
    id  1
    rho 1000.0
    mu  1.043e-3
  end

  load_balance
    method   rcb
  end

  materialset
    id 10
    material 1
    block 1
    block 2
    block 3
    block 4
  end

  statistics
    starttime   0.2
    endtime     1.0
    plotwinsize 0.05
  end

  plotvar
    elem div
    elem vel
    elem procid
    elem volume
    elem vginv2
    node dist
    node enstrophy
    node pressure
    node vel
    node vorticity
    node helicity

    # wall shear on the
    # rods and spacers
    side 3 wallshear
    side 6 wallshear

    # yplus on the spacer,
    # rods, sides, support
    side 3 yplus
    side 6 yplus
    side 7 yplus
    side 8 yplus
  end

  plotstatvar
    node <velocity>
    node <pressure>
    node <pressure',pressure'>

    elem <velocity>
    elem <vorticity>
    elem <helicity>
    elem tke
    elem reynoldsstress

    side 6 <pressure>
    side 6 <pressure',pressure'>
  end

  # Simple IC's
  initial
    velx 0.0
    vely 2.48
    velz 0.0
    turbnu 5.0e-7
  end

  velocity
    # Inflow
    velx sideset 4 -1 0.0
    vely sideset 4 -1 2.48
    velz sideset 4 -1 0.0

    # Spacer
    velx sideset 3 -1 0.0
    vely sideset 3 -1 0.0
    velz sideset 3 -1 0.0

    # Rods
    velx sideset 6 -1 0.0
    vely sideset 6 -1 0.0
    velz sideset 6 -1 0.0

    # Sides
    velx sideset 7 -1 0.0
    vely sideset 7 -1 0.0
    velz sideset 7 -1 0.0

    # Support
    velx sideset 8 -1 0.0
    vely sideset 8 -1 0.0
    velz sideset 8 -1 0.0
  end

  pressure
    sideset 5 -1 0.0 # Outflow
  end

  ppesolver
    type  AMG
    amgpc HYPRE
    hypre_type BOOMERAMG
    strong_threshold 0.7
    levels 20
    itmax 100
    itchk 1
    coarse_size 1500
    diagnostics off
    convergence off
    eps   1.0e-5
  end

  momentumsolver
    type  ILUFGMRES
    itmax 50
    itchk 2
    restart 25
    diagnostics off
    convergence off
    eps   1.0e-5
  end

end

exit
```

Figure 4.17: Control file for 5 × 5 rod-bundle LES calculations.

CASL-U-2013-0324-000-b

Bibliography

[1] J. Bakosi, M. A. Christon, M. M. Francois, R. B. Lowrie, and R. R. Nourgaliev. GTRF calculations using Hydra-TH. Technical Report LA-UR-12-24526, Los Alamos National Laboratory, September 2012.

[2] M. A. Christon, J. Bakosi, and R. B. Lowrie. Hydra-TH User's Manual, Version: LA-CC-11120. Technical report, November, 2011.

[3] Mark A Christon. Hydra-TH Theory Manual. Technical report, Los Alamos National Laboratories, Los Alamos, New Mexico, LA-UR-11-05387, 2011.

[4] Mark A. Christon. Hydra-TH Theory Manual. Technical Report LA-UR 11-05387, Los Alamos National Laboratory, September 2011.

[5] Mark A. Christon, Jozsef Bakosi, Nathan Barnett, Marianne M. Francois, and Robert B. Lowrie. Initial Assessment of Hydra-TH on Grid-to-Rod Fretting Problems (thm.cfd.p4.01). Technical Report LA-UR-11-07034, Los Alamos National Laboratory, 2011.

[6] M. E. Conner, E. E. Dominguea-Otiveros, and Y. A. Hassan. Hydraulic benchmark data for pwr mixing vane grid. In *The 14th International Topical Meeting on Nuclear Reactor Thermal Hydraulics*, Toronto, Canada, September 2011.

[7] G. de Vahl Davis. Natural convection of air in a square cavity: a bench mark numerical solution. *International Journal for Numerical Methods in Fluids*, 3:249–264, 1983.

[8] G. de Vahl Davis and I. P. Jones. Natural convection in a square cavity: a comparison exercise. *International Journal for Numerical Methods in Fluids*, 3:227–248, 1983.

[9] A. M. Elmahdi, R. Lu, M. E. Conner, Z. Karoutas, and E. Baglietto. Flow induced vibration forces on a fuel rod by les cfd analysis. In *The 14th International Topical Meeting on Nuclear Reactor Thermal Hydraulics (NURETH-14)*, Hilton Toronto Hotel, Toronto, Ontario, Canada, September 2011.

[10] Ercan Erturk and Bahityar Dursun. Numerical solutions of 2-d steady incompressible flow in a driven skewed cavity. *ZAMM - Journal of Applied Mathematics and Mechanics*, 87:377–392, 2007.

[11] U. Ghia, N. Ghia, and C. T. Shin. High-*Re* solutions for incompressible flow using the Navier-Stokes equations and a multigrid method. *Journal of Computational Physics*, 48:387–411, 1983.

[12] R. Y. Lu, Z. Karoutas, M. A. Christon, J. Bakosi, and L. Pritchett-Sheats. Cfd turbulence force calculations and grid-to-rod fretting simulation. Technical Report CASL-I-2012-0165-000, Consortium for Advanced SImulation of Light-Water Reactors (CASL), December, 2012 2012.

[13] Parviz Moin and Krishnan Mahesh. Direct numerical simulation: a tool in turbulence research. *Annual Review of Fluid Mechanics*, 30(1):539–578, 1998.

[14] R. D. Moser, J. Kim, and N. N. Mansour. Direct numerical simulation of turbulent channel flow up to $\mathrm{Re}_\tau = 590$. *Phys. Fluids*, 11(4), 1999.

[15] A. K. Prasad and J.R. Koseff. Reynolds number and end-wall effects on a lid-driven cavity flow. *Phys. Fluids A*, 1(2), 1989.

[16] J. N. Shadid, T. M. Smith, R. P. Pawlowski, E. C. Cyr, P. D. Weber, and D. Z. Turner. Initial drekar LES CFD simulations for grid-torod fretting (gtrf) (thm.cfd.p2.01). Technical report, Sandia National Laboratories, 2011.

[17] J. Yan. personal communication. August 2012.

[18] J. Yan, M. E. Conner, R. A. Brewster, Z. E. Karoutas, E. E. Dominguez-Ontiveros, and Y. A. Hassan. Validation of CFD method in predicting steady and transient flow field generated by PWR mixing vane grid. In *CFD4NRS-4 – The Experimental Validation and Application of CFD and CMFD Codes in Nuclear Reactor Technology, OECD/NEA & International Atomic Energy Agency (IAEA) Workshop*, Daejeon, Korea, September 2012.

Index

Introduction, 1

Navier-Stokes
- 2D problems, 3
  - blasius, 22
  - convection in a square cavity, 16
  - lid-driven skew cavities, 10
  - Poiseuille flow, 3
- 3D problems, 45
  - LES simulation of lid-driven cavity flow, 45
- Benchmark Problems
  - 3×3 GTRF, 59
  - 3×3 rod bundle, 59
  - 5×5 rod bundle, 68
- Thermal-Hydraulic Benchmark Problems, 59